

AD-A102 155

PRINCETON UNIV NJ DEPT OF MECHANICAL AND AEROSPACE --ETC F/6 1/2
TRANSITION AND CONVERSION TRIM-MAPS FOR THE AV-8A VTOL AIRCRAFT--ETC(U)
AUG 80 B HILDRETH

N00014-78-C-0381

UNCLASSIFIED

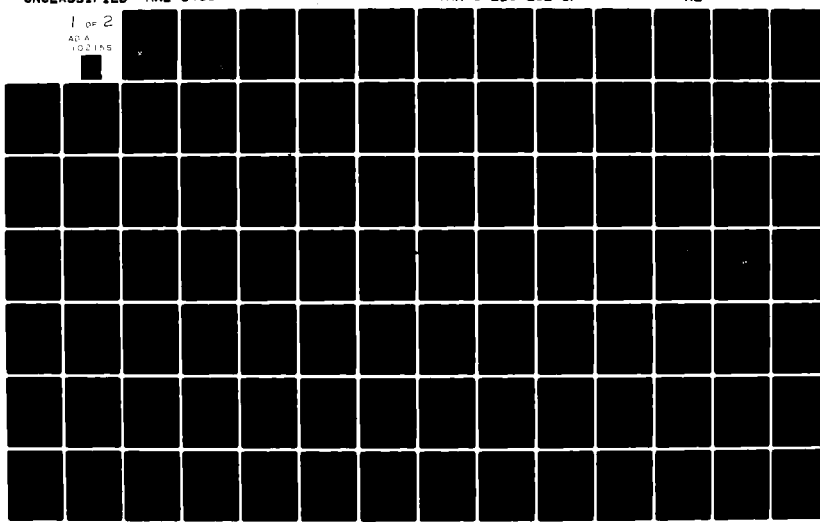
MAE-1466

ONR-CR215-262-1F

NL

1 of 2

ADA A
102155



LEVEL II

1

Princeton University

ADA102155



Department of
Mechanical and
Aerospace Engineering

DTIC FILE COPY

DTIC
SELECTED

JUL 29 1981

D

DISTRIBUTION STATEMENT A
Approved for public release
Distribution Unlimited

817 28102

LEVEL

1

REPORT ONR-CR215-262-1F

TRANSITION AND CONVERSION TRIM-MAPS
FOR THE AV-8A VTOL AIRCRAFT

AUGUST 1980

Prepared for:

NAVAL AIR DEVELOPMENT CENTER
Warminster, PA 18974

Under ONR Contract Number
N00014-78-C-0381

Accession For	
NTIS	GR4&I
DTIC TAB	<input type="checkbox"/>
Unannounced	<input type="checkbox"/>
Justification	
By	
Distribution/	
Availability Codes	
Avail and/or	
Dist	Special
A	

Approved for Public Release
Distribution Unlimited

DTIC
SELECTED
JUL 29 1981
S D

D

Unclassified

SECURITY CLASSIFICATION OF THIS PAGE (When Data Entered)

REPORT DOCUMENTATION PAGE		READ INSTRUCTIONS BEFORE COMPLETING FORM
1. REPORT NUMBER ONR/CR215-262-1F	2. GOVT ACCESSION NO. AD-A102	3. RECIPIENT'S CATALOG NUMBER 155
4. TITLE (and Subtitle) TRANSITION AND CONVERSION TRIM-MAPS FOR THE AV-8A VTOL AIRCRAFT.	5. TYPE OF REPORT & PERIOD COVERED FINAL REPORT.	
7. AUTHOR(s) Bruce Hildreth	6. PERFORMING ORG. REPORT NUMBER MAE Rept. No. 1466	
9. PERFORMING ORGANIZATION NAME AND ADDRESS Department of Mechanical and Aerospace Engineering Princeton University Princeton, N.J. 08544	10. PROGRAM ELEMENT, PROJECT, TASK AREA & WORK UNIT NUMBERS NR-215-262	
11. CONTROLLING OFFICE NAME AND ADDRESS Office of Naval Research 800 North Quincy Street Arlington, VA 22217	12. REPORT DATE AUGUST 1980	
14. MONITORING AGENCY NAME & ADDRESS (if different from Controlling Office) Naval Air Development Center Warminster, PA 18974	13. NUMBER OF PAGES xiii + 131	
16. DISTRIBUTION STATEMENT (of this Report) Distribution Unlimited	15. SECURITY CLASS. (of this report) Unclassified	
	15a. DECLASSIFICATION DOWNGRADING SCHEDULE	
17. DISTRIBUTION STATEMENT (of the abstract entered in Block 20, if different from Report)	14.1.1.1	
18. SUPPLEMENTARY NOTES		
19. KEY WORDS (Continue on reverse side if necessary and identify by block number) Vertical Take-Off and Landing Mathematical Modelling Decelerating Flight Approach and Landing	Jet VTOL Aircraft (Harrier) Transition Conversion Trim	
20. ABSTRACT (Continue on reverse side if necessary and identify by block number) A Mathematical computer model, "HARRIER", of the AV-8A Harrier aircraft has been developed utilizing the concept of quasi-stationary flight in order to determine quasi-equilibrium values of flight variables and controls during accelerating-decelerating flight. Using available aerodynamic data via look-up schemes, "trim-maps" are computed which show the values of the longitudinal flight and control variables as functions of airspeed and thrust angle. These maps have been shown to be useful tools in piecing together transition	14.1.1.1	

profiles, taking in consideration various requirements and constraints.

The final decelerating-descending phase of the present USMC approach profile has been analyzed in detail with the aid of the trim-maps. The technique of flying the transition as suggested by the trim-maps has been found in good agreement with the techniques actually used under the given constraints. This established confidence in both the mathematical model and in the trim-maps as tools for studying alternate transition profiles.

ACKNOWLEDGEMENTS

This report has been prepared by the Department of Mechanical and Aerospace Engineering of Princeton University as MAE Report No. 1466. The principal author of the report is Mr. Bruce Hildreth. Mr. Theodor A. Dukes, Principal Investigator, and Mr. Gerard J. Born made invaluable contributions. Mr. Dukes' ideas determined the course of the work, and both he and Mr. Born were involved in almost every detail of the research. Mr. Born's experience and contributions in the programming effort were especially significant.

The research leading to this report has been supported by the Office of Naval Research under ONR Contract No. N00014-78-C-0381 as part of the NAVTOLAND program. The Technical Representative was Mr. Charles Abrams of the Naval Air Development Center; his and Mr. Alfred Piranian's suggestions contributed significantly to shaping this project.

ABSTRACT

A mathematical computer model, "HARRIER", of the AV-8A Harrier aircraft has been developed utilizing the concept of quasi-stationary flight in order to determine quasi-equilibrium values of flight variables and controls during accelerating-decelerating flight. Using available aerodynamic data via look-up schemes, "trim-maps" are computed which show the values of the longitudinal flight and control variables as functions of airspeed and thrust angle. These maps have been shown to be useful tools in piecing together transition profiles, taking in consideration various requirements and constraints.

The final decelerating-descending phase of the present USMC approach profile has been analyzed in detail with the aid of the trim-maps. The technique of flying the transition as suggested by the trim-maps has been found in good agreement with the techniques actually used under the given constraints. This established confidence in both the mathematical model and in the trim-maps as tools for studying alternate transition profiles.

TABLE OF CONTENTS

	Page
ACKNOWLEDGEMENTS	i
ABSTRACT	ii
LIST OF FIGURES	iv
LIST OF TABLES	vii
NOMENCLATURE	viii
CHAPTER I - INTRODUCTION	1
Background	3
Description of the AV-8A Harrier	4
CHAPTER II - AV-8A HARRIER MODEL DEVELOPMENT	6
Quasi-Equilibrium Flight Model	6
Creation of the Trim-Map	8
Aerodynamics	10
Wing-body Aerodynamics	12
Effect of the Stabilizer	14
Inlet Effects Due to Ram Drag	15
Speedbrake Effects	16
Reaction Control System	16
Engine Model	17
CHAPTER III - RESULTS AND DISCUSSION	19
Interpretation of the Trim-Maps	20
Creating a Flight Profile	20
Control Moment Available	22
Speedbrake Effects	23
Thrust Effects	23
Minimum Fuel Consumption	24
Sample Transition Profile	25
CONCLUSIONS	30
REFERENCES	32
TABLES	34
FIGURES	35
APPENDIX A. EQUATIONS OF MOTION	115
APPENDIX B. METHOD OF SOLUTION	126

LIST OF FIGURES

Figures

1. Two sets of Control Positions Resulting in the Same Trimmed Flight Condition.
2. AV-8A Harrier; Forces and Moments Acting on the Aircraft.
3. AV-8A C_L _{wing-body} Without Wing/Jet Interaction.
- 4-6. AV-8A C_L _{wing-body} With and Without Wing/Jet Interaction for Various θ_j . $V_j/V_\infty = 5.4; 8.0; 11.9$.
7. AV-8A C_D _{wing-body} Without Wing/Jet Interaction for All θ_j , $V_j/V_\infty = 0.0$.
- 8-10. AV-8A C_D _{wing-body} With and Without Wing/Jet Interaction for Various θ_j . $V_j/V_\infty = 5.4; 8.0; 11.9$.
11. AV-8A C_m _{wing-body} Without Wing/Jet Interaction for All θ_j , $V_j/V_\infty = 0.0$.
- 12-14. AV-8A C_m _{wing-body} With and Without Wing/Jet Interaction for All θ_j , $V_j/V_\infty = 5.4; 8.0; 11.9$.
- 15-20. AV-8A C_L _{wing-body} With Wing/Jet Interaction. $\alpha = -4^\circ; 0^\circ; 4^\circ; 8^\circ; 12^\circ; 16^\circ$.
- 21-26. AV-8A C_D _{wing-body} With Wing/Jet Interaction, $\alpha = -4^\circ; 0^\circ; 4^\circ; 8^\circ; 12^\circ; 16^\circ$.
- 27-32. AV-8A C_m _{wing-body} With Wing/Jet Interaction, $\alpha = -4^\circ; 0^\circ; 4^\circ; 8^\circ; 12^\circ; 16^\circ$.

33. AV-8A Non-dimensionalized Lift Loss as a Function of θ_j and V_j/V_∞ .

34. $C_{L_{\text{wing-body}}}$ Flaps Up, Without Wing/Jet Interaction.

35. $C_{D_{\text{wing-body}}}$ Flaps Up, Without Wing/Jet Interaction.

36. $C_{m_{\text{wing-body}}}$ Flaps Up, Without Wing/Jet Interaction.

37. $C_{L_{\delta H}}$ With Wing/Jet Interaction for Various θ_j , All Angles of Attack (No Reaction Control Thrusters).

38-42. $C_{m_{\delta H}}$ With Wing/Jet Interaction (No Reaction Control Thrusters),
 $\theta_j = 30^\circ; 45^\circ; 60^\circ; 75^\circ; 90^\circ$.

43. Comparison of $C_{L_{\delta H}}$ Data.

44. Comparison of $C_{m_{\delta H}}$ Data.

45. Ram Drag at Various Mach Numbers.

46. Modelling $\Delta C_{m_{\text{inlet}}}$ Due to Ram Drag.

47-48. Change in Lift Coefficient Due to Ram Drag ($\Delta C_{L_{\text{inlet}}}$) for Various V_∞ , RPM = 94.4%; 105.8%.

49. Change in Lift Coefficient Due to Speedbrake Deflection ($\Delta C_{L_{\text{speedbrake}}}$) for $\delta_{\text{speedbrake}} = 30^\circ$.

50. Change in Drag Coefficient Due to Speedbrake Deflection ($\Delta C_{D_{\text{speedbrake}}}$) for $\delta_{\text{speedbrake}} = 30^\circ$.

51. Change in Pitching Moment Coefficient Due to Speedbrake Deflection ($\Delta C_{m_{\text{speedbrake}}}$) for $\delta_{\text{speedbrake}} = 30^\circ$.

52. Reaction Control System Duct Pressure Ratio as a Function of Engine RPM.

53. Functional Block Diagram of the AV-8A Reaction Control System and Engine.

54. Reaction Control System Duct Pressure Ratio as a Function of Total RCS Nozzle Area Opening.

55. RCS Nozzle Opening as a Function of Stabilizer Position.

56. Forward and Aft RCS Thrust Ratios as Functions of Their Respective Nozzle Openings.

57. RCS Effectiveness as a Function of Freestream Velocity.

58. Gross Thrust as a Function of Engine RPM.

59. Main Nozzle Thrust Distribution as a Function of Engine RPM.

60. Gross Thrust Increase Due to Freestream Velocity.

61. Pitching Moment per Degree of Stabilizer Deflection.

62. Maximum Nose Down RCS Control Pitching Moment.

63. Variation of Pitching Moment with Gross Thrust at $\theta_j = 90^\circ$.

64. Shipboard Approach Profile as Used by the United States Marine Corps.

65-71. Trimmmaps of α , δ_H , T/W, L/W, D/W, θ , V_j/V_∞ ; with $\delta_F = 50^\circ$, $\dot{u}_{V_c} = 0.1$ g, $\gamma_c = 0.1$ rad.

72-78. Trimmmaps of α , δ_H , T/W, L/W, D/W, θ , V_j/V_∞ ; with $\delta_F = 50^\circ$, $\dot{u}_{V_c} = 0.0$ g, $\gamma_c = 0.0$ rad.

79-85. Trimmmaps of α , δ_H , T/W, L/W, D/W, θ , V_j/V_∞ ; with $\delta_F = 50^\circ$, $\dot{u}_{V_c} = 0.0$ g, $\gamma_c = -0.1$ rad.

86-92. Trimmmaps of α , δ_H , T/W, L/W, D/W, θ , V_j/V_∞ ; with $\delta_F = 50^\circ$, $\dot{u}_{V_c} = -0.1$ g, $\gamma_c = 0.0$ rad.

93-99. Trimmmaps of α , δ_H , T/W, L/W, D/W, θ , V_j/V_∞ ; with $\delta_F = 50^\circ$, $\dot{u}_{V_c} = -0.1$ g, $\gamma_c = -0.1$ rad.

100-106. Trimmmaps of α , δ_H , T/W, L/W, D/W, θ , V_j/V_∞ ; with $\delta_F = 50^\circ$, $\dot{u}_{V_c} = -0.2$ g, $\gamma_c = -0.1$ rad.

LIST OF TABLES

	<u>Page</u>
1. Thrust/Weight Ratios and Time Limitations of the Pegasus 11 Engine	34
2. Summary of Trim-map Flight Conditions	34

NOMENCLATURE

b	wing span	ft
c	aerodynamic sideforce, body axis	lb
\bar{c}	mean aerodynamic chord (MAC)	8.43 ft
C_D	drag coefficient	
c_g	aircraft center of gravity	
C_L	lift coefficient	
C_λ	roll moment coefficient	
C_m	pitch moment coefficient	
C_n	yaw moment coefficient	
C_y	sideforce coefficient	
D	aerodynamic drag	lb
D/W	drag/weight ratio	
F_{x_B}	aerodynamic force along the x body axis	lb
F_{y_B}	aerodynamic force along the y body axis	lb
F_{z_B}	aerodynamic force along the z body axis	lb
g	acceleration due to local gravity force	32.17 ft/sec ²
g_{x_B}	acceleration due to gravity force along the x body axis	g
g_{y_B}	acceleration due to gravity force along the y body axis	g
g_{z_B}	acceleration due to gravity force along the z body axis	g

h	height above sea level (altitude)	ft
I_{yy}	moment of inertia about y axis	slug \cdot ft 2
L	aerodynamic lift	lb
L_a	aerodynamic roll moment	ft \cdot lb
L_e	roll moment due to engine and RCS	ft \cdot lb
L/W	aerodynamic lift/weight ratio	
M	total pitch moment (+ nose up)	ft \cdot lb
M_a	aerodynamic pitch moment	ft \cdot lb
MAC	mean aerodynamic cord (\bar{c})	8.43 ft
M_e	pitch moment due to engine and RCS	ft \cdot lb
M_N	Mach number	
N_a	aerodynamic yaw moment	ft \cdot lb
N_e	yaw moment due to engine and RCS	ft \cdot lb
N_F	engine fan speed	%
NM	nautical mile (6080 ft)	
p	roll rate, body axis	rad/sec
\dot{p}	roll acceleration, body axis	rad/sec 2
q	pitch rate, body axis	rad/sec
\dot{q}	pitch acceleration, body axis	rad/sec 2
\bar{q}	freestream dynamic pressure	lb/ft 2
r	yaw rate, body axis	rad/sec
\dot{r}	yaw acceleration, body axis	rad/sec 2
RCS	reaction control system	
S	wing area	201.1 ft 2

S_j	main nozzle area	13.0 ft^2
T	gross thrust	1b
T_{j_A}	thrust from aft main nozzles	1b
T_{j_F}	thrust from forward main nozzles	1b
T_{x_B}	total engine and RCS forces along the x body axis	1b
T_{y_B}	total engine and RCS forces along the y body axis	1b
T_{z_B}	total engine and RCS forces along the z body axis	1b
T/W	gross thrust/weight ratio	
T_{ϕ_p}	port RCS roll thrust; + RWD	1b
T_{ϕ_s}	starboard RCS roll thrust; + LWD	1b
T_{θ_A}	aft RCS pitch thrust	1b
T_{θ_F}	forward RCS pitch thrust	1b
T_{ψ}	yaw RCS thrust	1b
u	x body axis velocity	ft/sec
\dot{u}	x body axis acceleration	g
\dot{v}_c	acceleration commanded parallel to the x flight path axis	g
v	y body axis velocity	ft/sec
\dot{v}	y body axis acceleration	g
\dot{v}_c	acceleration commanded parallel to the y flight path axis	g

v_j / V_∞	main nozzle jet exhaust velocity/ freestream velocity ratio	
v_{w_x}	ambient wind velocity in the local inertial x axis	ft/sec
v_{w_y}	ambient wind velocity in the local inertial y axis	ft/sec
v_{w_z}	ambient wind velocity in the local inertial z axis	ft/sec
V_∞	freestream velocity	ft/sec
w	z body axis velocity	ft/sec
\dot{w}	z body axis acceleration	g
W	aircraft gross weight	lb
\dot{w}_{v_c}	acceleration commanded parallel to the z flight path axis (perpendicular to the flight path)	g
\dot{x}_I	x component of A/C velocity in the local inertial x axis	ft/sec
x_{j_A}	distance along the x_B axis from the cg to the aft main nozzles; (+ noz- zles aft of cg)	ft
x_{j_F}	distance along the x_B axis from the cg to the forward main nozzles; (+ nozzles forward of cg)	ft
x_ϕ	distance along the y_B axis from the cg to the roll RCS nozzles	ft
$x_{\phi\theta}$	distance along the x_B axis from the cg to the roll RCS nozzles; (+ noz- zles forward of cg)	ft

x_{θ_A}	distance along the x_B axis from the cg to the aft pitch RCS nozzles; (+ nozzles aft of cg)	ft
x_{θ_F}	distance along the x_B axis from the cg to the forward pitch RCS nozzles; (+ nozzles forward of cg)	ft
x_{ψ}	distance along the x_B axis from the cg to the yaw RCS nozzles; (+ nozzle aft of cg)	ft
x_{mr}	distance along the x_B axis from the moment reference center to the cg; (+ moment reference center forward of cg)	ft
Y	aerodynamic force along the y axis, wind axis system	lb
\dot{y}_I	y component of A/C velocity w.r.t. the local inertial axis system	ft/sec
\dot{z}_I	z component of A/C velocity w.r.t. the local inertial axis system	ft/sec
α	fuselage angle of attack	radians
β	fuselage angle of sideslip	radians
γ	longitudinal flight path angle	radians
δ_F	flap position	radians
δ_H	stabilizer position (horizontal tail)	degrees
δ_{SB}	speedbrake position	30 degrees
θ	aircraft pitch attitude	radians

θ_j	nozzle deflection angle	radians
	$\theta_j = 0$ nozzles aligned with x_B axis	
ξ	flight path azimuth angle; clockwise from north	radians
ρ	local atmospheric density	0.002377 ₃ slugs/ft ³
ϕ	aircraft roll attitude	radians
ψ	aircraft heading	radians

Subscripts

(.)_I local inertial axis system; x axis north
flat, non-rotating earth

(.)_B aircraft body fixed axis system; centered at the aircraft cg
positive x forward
positive y out right wing

(.)_w wind axis system; centered at the aircraft cg
positive x aligned with the freestream and opposite in direction
positive z lies in the plane of symmetry and is positive
down

(.)_v velocity axis system; centered at the aircraft cg
positive x forward aligned with the flight path
positive y orthogonal to the x axis and horizontal to the right

CHAPTER I
INTRODUCTION

Over the past decade Vertical/Short Takeoff and Landing (V/STOL) aircraft have been of increasing interest to the aerospace community. One of the most critical phases of V/STOL flight is the transition from wing borne to jet borne flight. The stability of a V/STOL aircraft normally changes significantly in transition and becomes unstable at hover. This creates a high pilot workload and therefore a potentially dangerous situation. Therefore, investigating transition techniques and flight paths is of great importance when studying V/STOL aircraft.

The purpose of this report is to develop and demonstrate a mathematical method for studying the transition performance and control of highly non-linear V/STOL aircraft. Although the sample aircraft chosen is the AV-8A Harrier, the analysis used is valid for any V/STOL aircraft. The purpose of this work is to demonstrate the usefulness of the method to the analysis of the Harrier and to provide some general guidelines on Harrier transition techniques.

The method is based on a non-linear longitudinal force and moment balance model of the Harrier aircraft in transition flight. The concept of a force balance model is extended to include the inertial forces produced by constant acceleration along a prescribed flight path. This model represents "snapshots" of the force and moment balance while accelerating along the flight path. The concept of "trim" is expanded to mean the combination of controls, at a given flight condition (altitude, weight, c.g. position and velocity), which is needed to establish force and moment balance including the inertial components due to acceleration. If it is desired to examine a trim point where no flight path acceleration is taking place then "trim" assumes its conventional meaning of an aircraft in steady unaccelerated flight. This model is used to create a "trim-map" of the variables of interest in the transition speed range. With such

"trim-maps" the performance and control limitations of the aircraft may be studied in a logical, organized fashion. The trim-maps can be used to identify candidates for the best transition flight path and conversion program, taking into consideration many factors, such as fuel consumption, time duration, pilot workload and visibility, control margins, and engine operating limits.

Mapping the trim points is a convenient way to present the result of the force balance model because in V/STOL aircraft there is generally a redundancy in controls during conversion/transition.

In the Harrier, the pilot has four longitudinal controls available:

1. Longitudinal stick
2. Throttle
3. Flaps
4. Jet deflection angle

Figure 1 illustrates how different combinations of longitudinal stick, (controlling the attitude), jet deflection angle (nozzle position), and throttle position may combine in different ways to create the same flight conditions. With the flaps down, the Harrier can fly straight and level at 220 ft/s at any angle of attack (α) between 15.5° and -5.0° with the nozzle deflection (θ_j) varying from 0° to 80° . Varying the flap setting (δ_f) would further increase the variations in α and θ_j . The goal of this study is to establish the relationships among the longitudinal controls, including control limitations, so that transition flight paths and piloting techniques may be compared as to their relative merits.

First, in the rest of this Chapter, some background and a brief description of the AV-8A Harrier are given. Chapter 2 discusses the development of the mathematical model. Finally, in Chapter 3 the resulting trim-maps are discussed and an example transition flight path is given to illustrate how the trim-maps

are utilized. Henceforth, HARRIER in capital letters refers to the computer program .

Background

In studying the aforementioned problem, much effort was expended in researching methods to theoretically determine V/STOL transition flight paths (References 12 through 15). Although many papers have been written on this general subject, it was found that none of the studies accounted for an airframe that had severe control power limitations and coupling between engine thrust and aerodynamic lift. The fact that the lift force is a function of gross thrust and thrust deflection angle in addition to the angle of attack vastly increases the analytical problem. In addition, when the aircraft has marginal control power within a certain speed range, the problem of finding the best way to transition the aircraft from forward to hovering flight is compounded. This is because the performance and the stability and control characteristics must be considered simultaneously. The path for a minimum power, minimum fuel consumption, or minimum time approach may be (and is for the AV-8A) severely constrained by the longitudinal control power available. Closed form flight path optimization becomes very complicated when the above mentioned problems are included.

Another problem with classical optimization in general is that once the optimal flight path is found, only the pilot technique required to fly this path is studied. It becomes difficult to research the "optimum pilot technique" in any sense in this manner.

The trim-maps derived and discussed in this report incorporate all the significant features of the aircraft. They are equally applicable to general theoretical aircraft or to any particular V/STOL aircraft. The only

drawback of the trim-maps is that they do not directly show how to get from one point to another. In most cases this is relatively straightforward. They do, however, vividly show minimum fuel consumption (thrust) approaches and pilot technique required. Control margins and effectiveness are also indicated.

The interpretation of the calculated trim-maps for the AV-8A is contained in Chapter 3.

Description of the AV-8A Harrier

The AV-8A Harrier is a subsonic, single cockpit, single engine turbofan aircraft with V/STOL capabilities which arise from being able to rotate the thrust vector from 0° (thrust aligned with the x_B axis) to 98.5° by means of four nozzles, two on each side of the aircraft. The two front nozzles exhaust the low pressure bypass air and the two rear nozzles exhaust the hot turbine air. Gross thrust is distributed almost equally between the forward and aft nozzles and the resultant thrust vector acts close to the cg.

The Harrier has a tapered swept wing mounted on top of the fuselage with negative geometric dihedral. Similarly, the horizontal tail too is tapered, swept and has negative geometric dihedral. There is a single ventral fin mounted below the vertical stabilizer at the tail. The aircraft has half-span trailing edge flaps which are normally deflected 50° for takeoff and landing and 0° (flaps up) for cruise. There is also a speedbrake, mounted hinge forward, beneath the tail and just forward of the ventral fin. Maximum speedbrake deflection is 66° . Nominal speedbrake positions are 0° (speedbrake stowed) for cruise and 25° for takeoff and landing configuration (undercarriage down). With the undercarriage down the speedbrake cannot be moved from the 25° position.

The AV-8A is approximately 45 ft long and has a 25-ft wingspan. Empty operating weight is approximately 12000 lbs. Maximum takeoff gross weight is 24600 lbs and design landing weight is 16900 lbs. Maximum vertical takeoff gross weight is 17500 lbs. Maximum gross engine thrust is slightly less than 20000 lbs.

Figure 2 shows a three view drawing of the AV-8A Harrier.

One aircraft configuration was examined in detail in this study;

- a) flaps down 50°
- b) undercarriage down
- c) speedbrake extended 30°

As previously mentioned, actual speedbrake deflection in takeoff and landing is 25°. However, because the wind tunnel data were available only for 30° deflection, the model assumes a 30° speedbrake deflection.

Most of the data used in modelling the AV-8A is contained in five McDonnell Douglas Corporation reports, References 16 through 20. Reference 16 contains the vast majority of the aerodynamic data on the Harrier. Reference 17 contains reaction control system data, while Reference 18 details the jet-induced lift loss effects. The model of the reaction control system described in this report was derived based on Nave's report (Ref. 7.) which contains the description of a simulation of the dynamics of the AV-8A in transition.

CHAPTER II
AV-8A HARRIER MODEL DEVELOPMENT

Quasi-Equilibrium Flight Model

For the purposes of producing a set of trimmaps a quasi-equilibrium flight model is needed. In this study equilibrium flight is defined as steady unaccelerated flight along a straight path (not necessarily level). This means:

u_v , v_v , and w_v are constant

$\dot{u}_v = \dot{v}_v = \dot{w}_v = p = q = r = \dot{p} = \dot{q} = \dot{r} = 0$

Quasi-equilibrium flight is defined similar to equilibrium flight but allows for constant linear accelerations. Having both velocities and accelerations constant in the force and moment balance equations means that only a particular instant of time, or a "snapshot" of an aircraft accelerating along a flight path, is examined. The instant of the snapshot is the time at which the aircraft accelerates through the specified velocity. In the quasi-equilibrium case;

u_v , v_v , w_v , \dot{u}_v , \dot{v}_v , \dot{w}_v are constant

p , q , r , \dot{p} , \dot{q} , \dot{r} are small and assumed zero

These assumptions simplify modelling the aircraft by eliminating time dependence, so only the algebraic equations of force and moment equilibria need be solved.

General equations derived with the assumptions above are presented in Appendix A. Because this study only considers flight in a vertical plane, $\phi = \psi = \xi = \dot{\gamma}_I = 0$;

furthermore the ambient wind is considered to be zero:

$$\beta = v_B = 0$$

Using these assumptions, the seven equations required to model the Harrier in transition are Equations A-3, A-5, A-13, and A-16 from Appendix A.

$$\dot{u}_B = (1/W)(-D\cos\alpha + L\sin\alpha + T\cos\theta_j) - \sin\theta \quad (1)$$

$$\dot{w}_B = (1/W)(-D\sin\alpha - L\cos\alpha - T\sin\theta_j - T_{\theta_A} - T_{\theta_F}) + \cos\theta \quad (2)$$

$$L = (1/2)\rho V_\infty^2 S C_L \quad (3)$$

$$D = (1/2)\rho V_\infty^2 S C_D + D_{\text{ram}} \quad (4)$$

$$\dot{x}_I = u_B \cos\theta + w_B \sin\theta \quad (5)$$

$$\dot{z}_I = -u_B \sin\theta + w_B \cos\theta \quad (6)$$

$$M = ((1/2)\rho V_\infty^2 S C_m + T_{\theta_F} x_{\theta_F} + T_{\theta_A} x_{\theta_A} + (T_{j_F} x_{j_F} + T_{j_A} x_{j_A}) \sin\theta_j + x_{mr} L \cos\alpha + x_{mr} D \sin\alpha) / I_{yy} \quad (7)$$

where $M = 0$ in quasi-equilibrium flight

$$\alpha = \theta - \gamma_c \text{ (with no ambient winds)} \quad (8)$$

$$T = (V_j/V_\infty)^2 \bar{q} S_j \quad (9)$$

$$C_L = f(\alpha, \frac{T}{\rho V_\infty^2 S}, \frac{V_j}{V_\infty}, \theta_j, \delta_F, \delta_H) \quad (10)$$

$$C_D = f(\alpha, \frac{T}{\rho V_\infty^2 S}, \frac{V_j}{V_\infty}, \theta_j, \delta_F) \quad (11)$$

$$D_{\text{ram}} = f(V_\infty, T) \quad (12)$$

$$C_m = f(\alpha, \frac{T}{\rho V_\infty^2 S}, \frac{V_j}{V_\infty}, \theta_j, \delta_F, \delta_H) \quad (13)$$

$$T_{\theta_A} = f(T, V_\infty, \delta_H) \quad (14)$$

$$T_{\theta_F} = f(T, V_\infty, \delta_H) \quad (15)$$

$$T_{j_A} = f(T, V_\infty) \quad (16)$$

$$T_{j_F} = f(T, V_\infty) \quad (17)$$

and x_{θ_F} , x_{θ_A} , x_{j_F} , x_{j_A} , x_{mr} are all moment arm lengths and functions of the longitudinal cg position. They are assumed to be constant for each flight profile. S , W , I_{yy} , and \bar{c} are wing area, aircraft gross weight, pitching moment of inertia, and mean aerodynamic chord, respectively; ρ is the atmospheric density and is held constant at its sea level value.

Equations (1) and (2) define the body-axis accelerations of the aircraft. Equations (3) and (4) compute the aerodynamic lift and drag of the aircraft. Equations (5) and (6) comprise the axis transformation from the body-axis system to the local inertial axis system. Finally, Equation (7) is the equation for pitch acceleration. The actual functions C_L , C_D , and C_m are quite complex and shall be discussed later in this chapter.

Creation of the Trim-Maps

Equations (1) through (7), with the relations expressed by Equations (8) through (17), allow for the solution of 7 unknowns. However, a total of 25 unknown parameters and variables appear in the 17 equations after the aircraft physical characteristics (S , \bar{c} , W , I_{yy} , cg , x_{θ_A} , x_{θ_F} , x_{j_A} , x_{j_F} , x_{mr}) are given. These unknowns are:

$$u_B, w_B, \dot{u}_B, \dot{w}_B, L, D, \alpha, \theta, T, T_{\theta_A}, T_{\theta_F}, C_L, C_D, D_{ram}, C_m, T_{j_F}, \\ T_{j_A}, \delta_H, \delta_F, \theta_j, V_\infty, V_j/V_\infty, \gamma, \dot{x}_I, \dot{z}_I$$

Therefore, after the physical characteristics are set, 8 more parameters or variables must be specified or determined.

For each trim-map the flap position, δ_F , the vertical flight path angle, γ_c , and the accelerations of the aircraft in the flight path (velocity) axes, \dot{u}_{v_c} and \dot{w}_{v_c} (the subscript c indicates commanded quantities) are specified

and held constant. Airspeed, V_∞ , and jet nozzle deflection angle, θ_j , are varied to map the speed range where quasi-equilibrium flight may occur at each θ_j . These six variables and parameters are inputs to the HARRIER computations.

The body axis accelerations in Equations (1) and (2) are substituted by flight path axis acceleration inputs via the following axis transformation:

$$\dot{u}_B = \dot{u}_{V_c} \cos\alpha - \dot{w}_{V_c} \sin\alpha \quad (18)$$

(from A-13)

$$\dot{w}_B = \dot{u}_{V_c} \sin\alpha + \dot{w}_{V_c} \cos\alpha \quad (19)$$

This substitution does not affect the number of unknowns.

Two more variables are actually inputs as determined by the following two equations:

$$\dot{x}_I = V_\infty \cos\gamma_c \quad (20)$$

(from A-8)

$$\dot{z}_I = -V_\infty \sin\gamma_c \quad (21)$$

Substituting Equations (18), (19), (20), and (21) into the left sides of Equations (1), (2), (5), and (6) respectively and rearranging Equations (1) through (7), with $\bar{q} = (1/2)\rho V_\infty^2$,

$$0 = (1/W)(-D\cos\alpha + L\sin\alpha - T\cos\theta_j) - \sin\theta_j - (\dot{u}_{V_c}/g)\cos\alpha + (\dot{w}_{V_c}/g)\sin\alpha \quad (22)$$

$$0 = (1/W)(-D\sin\alpha - L\cos\alpha - T\sin\theta_j - T_{\theta_A} - T_{\theta_F}) + \cos\theta_j - (\dot{u}_{V_c}/g)\sin\alpha - (\dot{w}_{V_c}/g)\cos\alpha \quad (23)$$

$$0 = L - \bar{q}SC_L \quad (24)$$

$$0 = D - \bar{q}SC_D - D_{ram} \quad (25)$$

$$0 = -u_B \cos \theta - w_B \sin \theta + V_\infty \frac{\cos \gamma_c}{c} \quad (26)$$

$$0 = u_B \sin \theta - w_B \cos \theta - V_\infty \frac{\sin \gamma_c}{c} \quad (27)$$

$$0 = (\bar{q} \bar{S} \bar{C}_m + T_{\theta_F} x_{\theta_F} + T_{\theta_A} x_{\theta_A} + (T_{j_F} x_{j_F} + T_{j_A} x_{j_A}) \sin \theta_j \\ + x_{mr} L \cos \alpha + x_{mr} D \sin \alpha) / I_{yy} \quad (28)$$

For determining

$$\alpha, C_L, C_D, D_{ram}, C_m, V_j/V_\infty, T_{\theta_A}, T_{\theta_F}, T_{j_F}, \text{ and } T_{j_A}$$

the relationships expressed in Equations (8) through (17) are used, utilizing look-up schemes and interpolation where necessary, making a total of 17 independent relationships available to calculate 17 variables. The quasi-equilibrium "trim" points for each variable of interest can be calculated and plotted as functions of V_∞ and θ_j . These plots, one for each variable ($L/W, D/W, T/W, \theta, \delta_H, u_B, w_B$) are called trim-maps.

Appendix B describes the method used to solve the system of equations.

Aerodynamics

Modelling the aerodynamics of the Harrier aircraft is a complex task because of wing/jet aerodynamic interaction. This interaction is a result of the air flow at the engine inlet and of the jet exhaust from the main nozzles interfering with the freestream air flow at the wing. The interaction varies strongly with the jet velocity ratio, V_j/V_∞ , and θ_j , but only slightly with α . Essentially all aerodynamic coefficients except speed-brake effects are influenced by this interaction. The effects on the lift are the most significant, with increasing V_j/V_∞ and/or θ_j decreasing the lift produced (for constant α). This results in a significant "lift-loss"

occurring in transition from forward flight in the airplane configuration to hover. As would be expected, drag generally decreases as lift decreases because of the reduction in induced drag. As V_j/V_∞ and θ_j increase, C_m changes from negative to positive and C_m becomes neutrally stable or unstable. In the majority of the cases these terms are quite non-linear functions of V_j/V_∞ and θ_j .

The interaction effects must be included when modelling the Harrier. Theoretical models representing these interactions were thoroughly investigated (References 1 through 4, among many) only to find that because of the difficulty and poor results in predicting interaction effects all sources recommend the use of experimental data when available. Therefore, the aerodynamic data for the Harrier which include interaction effects were not modelled analytically.

The basic aerodynamic data are presented in Reference 5 and are in the form of carpet plots. Since the data were so non-linear and functions of three variables it was found impractical to obtain functional relations by means of curve fitting. Therefore, the aerodynamic data and most other functional relationships were inserted into the HARRIER computer program in the form of table look-ups. The table look-up subroutines give the value of a parameter at any point and also its partial derivative with respect to each of the inputs. These partials are needed for the numerical solution. Between data points linear interpolation is used for obtaining the value of the function so that the partial derivatives are piecewise constant functions of the arguments.

The components of C_L , C_D and C_m used to model the Harrier are:

$$C_L = C_{L_{\text{wing-body}}}(\alpha, \theta_j, V_j/V_\infty, \delta_F) + C_{L_{\delta_H}}(V_j/V_\infty, \theta_j) \Delta \delta_H$$

$$+ C_{L_{\text{speedbrake}}}(\alpha, \delta_{SB}) + C_{L_{\text{inlet}}}(\alpha, V_\infty, \text{RPM})$$

$$C_D = C_{D_{\text{wing-body}}}(\alpha, \theta_j, V_j/V_\infty, \delta_F) + C_{D_{\text{speedbrake}}}(\alpha, \delta_{SB})$$

Ram drag is computed separately and is therefore not included in C_D ; $C_{D_{\delta_H}}$ was found insignificant and is therefore neglected.

$$C_m = C_{m_{\text{wing-body}}}(\alpha, \theta_j, V_j/V_\infty, \delta_F) + C_{m_{\delta_H}}(V_j/V_\infty, \alpha, \theta_j) \Delta \delta_H$$

$$+ C_{m_{\text{speedbrake}}}(\alpha, \delta_{SB}) + C_{m_{\text{inlet}}}(\alpha, V_\infty, \text{RPM})$$

where $\Delta \delta_H = \delta_H - 6.0^\circ$

References 5, 6, and 7 contain the data which determine the values of the above coefficients.

Wing-body Aerodynamics

The wing-body contribution to C_L , C_D and C_m with flaps down is presented in Reference 5 in the form of carpet plots showing C_L as a function of α , and C_D and C_m as functions of C_L , for various V_j/V_∞ and θ_j . These data were taken from wind tunnel tests of a powered model and, therefore, wing/jet interaction effects are included. Engine thrust and moment are not included in these data because the airflow source simulating the engine was supported separately from the rest of the model. For insertion into the HARRIER computer program, C_D and C_m were transformed to be functions of α instead of C_L . Figures 3 through 14 display these data.

In Reference 5 no data are given for θ_j equal to zero (airplane configuration) at any V_j/V_∞ other than zero (unpowered model). Therefore,

nothing is known about the wing/jet interaction effects for $\theta_j = 0$. To investigate this case, the carpet plots of $C_{L_{\text{wing-body}}}$, $C_{D_{\text{wing-body}}}$ and $C_{m_{\text{wing-body}}}$ were replotted as functions of θ_j for a constant α and various V_j/V_∞ . Figures 15 through 32 show these plots.

From these plots it can be seen that for constant V_j/V_∞ and regardless of angle of attack $C_{L_{\text{wing-body}}}$ and $C_{D_{\text{wing-body}}}$ approach their respective values for $V_j/V_\infty = 0$ as θ_j goes to zero. This indicates that for $C_{L_{\text{wing-body}}}$ and $C_{D_{\text{wing-body}}}$ there are negligible wing/jet interactions at $\theta_j = 0$, regardless of V_j/V_∞ .

While $C_{L_{\text{wing-body}}}$ and $C_{D_{\text{wing-body}}}$ vary almost linearly with θ_j , $C_{m_{\text{wing-body}}}$ is a non-linear function of θ_j . It is therefore more difficult to extrapolate $C_{m_{\text{wing-body}}}$ to $\theta_j = 0$. However, $C_{L_{\text{wing-body}}}$ and $C_{D_{\text{wing-body}}}$ clearly show that wing/jet interactions become negligible as θ_j goes to zero so therefore it will be assumed this holds true for $C_{m_{\text{wing-body}}}$ as well.

As a result, for $\theta_j = 0$, it is assumed that there are no wing/jet interaction effects regardless of the value of V_j/V_∞ . Therefore, in Figures 3, 7, and 11 the single curve represents all values of θ_j at $V_j/V_\infty = 0$. In the rest of Figures 3-14 the same curves as on Figures 3, 7, and 11, respectively, represent the values of $C_{L_{\text{wing-body}}}$, $C_{D_{\text{wing-body}}}$, and $C_{m_{\text{wing-body}}}$ for $\theta_j = 0$ for all V_j/V_∞ .

Some discrepancy was found in the data in Reference 5 when the data from the aforementioned carpet plots for C_L were compared to another figure in the same Reference (reproduced here as Figure 33) which shows the lift loss as a function of V_j/V_∞ . This question is discussed at the end of Appendix A.

Effect of the Stabilizer

The movable horizontal stabilizer has considerable effects on moment and lift. Its effect on drag is small and was neglected.

Again, inconsistencies in the data of Reference 5 were noted. Two sets of data presented there do not agree. The aforementioned carpet plots for C_L , C_D , and C_m give values at two positions of the horizontal stabilizer.

Therefore, assuming linearity, $C_{L_{\delta_H}}$ and $C_{m_{\delta_H}}$ can be calculated. Graphs of $C_{L_{\delta_H}}(V_j/V_\infty, \theta_j)$ and $C_{m_{\delta_H}}(a, V_j/V_\infty, \theta_j)$ (Figures 37 to 42) were also presented in the same reference. When the derivatives obtained from the carpet plots were superimposed upon the former data (at 8° angle of attack, Figures 43 and 44), the carpet plot data were found to be discontinuous and inconsistent. The former data (Figures 37 through 42) were used in the HARRIER program.

However, the $C_{L_{\delta_H}}$ and $C_{m_{\delta_H}}$ data given do not include data for $V_j/V_\infty = 0$ or $\theta_j = 0$. Examination of Figure 44 reveals that $C_{m_{\delta_H}}$ is close to linear with both V_j/V_∞ and θ_j , and linear extrapolation to $\theta_j = 0$ shows that $C_{m_{\delta_H}}$ at any V_j/V_∞ converges to approximately the same point (-.0208). Because of these facts, it was decided that linear extrapolation would be used for values of θ_j less than 30° and for values of V_j/V_∞ less than 5.4.

Examination of Figure 37 shows that $C_{L_{\delta_H}}(\theta_j)$ is not far from linear for θ_j between 30° and 60° ; linear extrapolation for values of θ_j less than 30° was used. Although the change in $C_{L_{\delta_H}}$ as a function of V_j/V_∞ seems to be a function of V_j/V_∞ squared, for simplicity linear extrapolation was again used for values of V_j/V_∞ less than 5.4.

The data in Figures 37 through 42 were used for $C_{L_{\delta_H}}$ and $C_{m_{\delta_H}}$ in the HARRIER program.

Inlet Effects Due to Ram Drag

The engine inlets on the Harrier are considerably forward of the cg, so ram drag at the inlet affects not only lift and drag but has a considerable effect on pitching moment. Ram drag as a function of engine RPM and Mach number was taken from Reference 7 and is presented in Figure 45.

The change in pitching moment coefficient due to ram drag was computed in Reference 5. Referring to Figure 46,

$$C_{m_{\text{inlet}}} = \frac{D_{\text{ram}}}{qS\bar{c}} \left[\underbrace{(10.41 \sin(\alpha - 7.5^\circ) + 8.10 \sin(7.5^\circ + 1.5^\circ))}_{\text{inlet face}} + \underbrace{8.10 \sin(7.5^\circ + 1.5^\circ)}_{\text{internal}} \right]$$

The first term inside the brackets represents turning the flow from freestream to the inlet face. The second term represents turning the flow inside the inlet (a moment arm, in feet, times the sine of the angle the flow was turned).

The change in lift coefficient due to ram drag at the inlet can be computed in a similar manner,

$$C_{L_{\text{inlet}}} = D_{\text{ram}} \frac{\sin(\alpha + 1.5^\circ)}{\bar{q}S} = \frac{L_{\text{inlet}}}{\bar{q}S}$$

where 1.5° is the additional angle, past the fuselage reference line, by which the airflow is turned to the engine face. The above equation was inserted into the HARRIER program in the form of Figures 47 and 48. A cross check between the data in References 5 and 7 confirmed the inlet effect data.

Speedbrake Effects

As given by Reference 5, the speedbrake effects are functions of α only. The data given are for a speedbrake deflection of 30° and all analyses were done with the speedbrake simulated in that position. Actual speedbrake position with undercarriage down is fixed at 25° .

Figures 49 through 51 present $C_{L_{\text{speedbrake}}}$, $C_{D_{\text{speedbrake}}}$ and $C_{m_{\text{speedbrake}}}$.

Reaction Control System (RCS)

Bleed air from the high pressure stage of the compressor of the Pegasus 11 engine is ducted to the nose, tail and wingtips of the Harrier to provide moments about all three axes at low speeds. The bleed air control is phased in during main nozzle deflection. For $\theta_j \geq 20^\circ$ full RCS moments are available. For $\theta_j = 10^\circ$, 50% of maximum moment is available. The RCS is not operational at $\theta_j = 0^\circ$.

The moment available about any axis (under standard day, sea level conditions) is primarily a function of engine speed (RPM), control surface position, and total demand on the RCS. The maximum amount of pitching moment produced by the pitch control thrusters is reduced when roll and/or yaw RCS thrust is also being used. Pitch reaction control is controlled by the longitudinal stick, roll is controlled by the lateral stick, and yaw is controlled by the rudder pedals. Although roll and yaw reaction controls are not used in this study, they could be added to the model.

Pitch control comes from fore and aft thrusters, exhausting downward, providing nose-up and nose-down moments, respectively. Figure 53 is a functional block diagram showing how the reaction control system was modelled.

Duct pressure ratios (DPR 1 and DPR 2) are computed as functions of engine RPM and of total reaction control system nozzle area (TRCSA) and are shown in Figures 52 and 54. Forward and aft RCS nozzle areas (FRCSP and ARCSP) are functions of the stabilizer position (Figure 55). The percentage of thrust from each nozzle (FRCST and ARCST) is then a function of nozzle area (FRCSA and ARCSA, Figure 56) times the duct pressure ratios. This percentage is then multiplied by the maximum thrust available if the nozzle were full open (FRCSMT and ARCSMT) to get actual thrust at the nozzle. This thrust is further multiplied by a reaction control effectiveness (DLRCV, Fig. 57) which is a function of velocity. The RCS effectiveness models the freestream effects on the nozzle exhaust. The freestream tends to change the effective angle of the nozzle exhaust; the faster the aircraft is traveling the less effective are the reaction controls. Figure 57 shows RCS effectiveness (DLRCV) as a function of V_∞ .

Engine Model

The Rolls Royce Pegasus 11 turbofan engine is modelled as a function of static gross thrust versus revolutions per minute (RPM). The engine has six distinct thrust ratings. These thrust ratings arise from temporarily allowing jet pipe and turbine over-temperatures, overspeeding of the engine, and injecting water into the engine to cool the combustion chamber and turbine. At each increased thrust rating there is a maximum operating time allowed. After this allowance is expended the engine must be run for five minutes at or below the maximum continuous rating before again exceeding it. Each engine also has a specified engine life and an engine life counter which keeps track of time and temperature when operating above 630°C jet pipe temperature. Under standard day conditions this is equal to about 92% RPM or a T/W of 1.01

(at 14000 lbs). Therefore, thrust above 14000 lbs. must be avoided whenever possible in order to save engine life. Figure 58 shows gross thrust versus RPM and the six thrust ratings. Table 1 shows the equivalent T/W ratios for a 14000 lb. aircraft.

Gross thrust increases as a function of freestream velocity due to the higher pressures at the compressor face. This gross thrust increase (Figure 60) is added to the aforementioned thrust vs. RPM curve. Knowing the thrust required to trim the aircraft, the RPM can then be found. Given RPM, Figure 59 shows the thrust distribution between the forward and aft main nozzles and so the pitching moment as a function of thrust is easily obtained.

All data are for a standard 50°F day at sea level. The effects of temperature, humidity, and altitude were neglected. The effect of bleeding RCS air on the gross thrust was also neglected.

CHAPTER III

RESULTS AND DISCUSSION

First in this chapter the interpretation of trim-maps is discussed in general. This is followed by a discussion of those transition constraints which are most significant for the AV-8A Harrier. General conclusions concerning significant characteristics of the AV-8A transition are then presented. Following, there is an example using the trim-maps to study the transition profile presently recommended for use during shipboard landings. The chapter is followed by a summary of the most significant conclusions.

Since landing transitions with the Harrier are more difficult than takeoff transitions, only the former are discussed in this report. However, trim-maps for a climbing, accelerating transition are also presented.

Trim-maps of the Harrier in transition are shown in Figures 65 through 106*; these were calculated for a freestream velocity range of 250 ft/sec to 0 ft/sec. The configuration studied was 14000 lbs gross weight and 7.8% mac cg. Flaps ($\delta_F = 50^\circ$) and undercarriage were down and speedbrake was out at 30° (normal speedbrake deflection on approach is actually 25°). The HARRIER also can handle flaps-up flight with the undercarriage up and the speedbrake still extended, with any weight and cg position. Table 2 summarizes the flight conditions mapped and shows where the results may be found.

* The trim-map formats were developed by T. A. Dukes, G. J. Born and T. O. Williams under NASA Grant No. NGR-31-001-277.

Interpretation of the Trim-Maps

Each set of trim-maps shows families of curves of α (ALFA), δ_H (DH), T/W(THRUST), L/W, D/W, θ_f (THETA F) and V_j/V_o as functions of V_∞ and θ_j for a given flight path angle and acceleration along the flight path.

Each plotted point represents the "trim" value of the variable at the given θ_j and V_∞ . On the trim-maps a 0 indicates $\theta_j = 0$; a "1" indicates 10 degrees; a "2" 20 degrees of θ_j , and so on. An* indicates $\theta_j = 100^\circ$.

For coincident points there is an A plotted when two points coincide; a B represents three coinciding points, etc. The data points of all the variables are truncated whenever α exceeds 20° or T/W exceeds 1.5.

Creating a Flight Profile

It must be emphasized that all the data points are for quasi-steady equilibrium (trimmed) flight and the dynamics involved in moving from one trim point to another are not considered here. However, it shall be seen that, in general, moving from one trim point to another is a very straightforward process. The transition profile is defined as all the parameters and variables which represent the flight path, aircraft configuration, and flight condition at which the aircraft is flying.

Creating a transition profile means piecing together the trim flight conditions as defined in the trim-maps in order to create a desired flight path and to indicate a pilot technique. A profile may be created by defining the flight path to be taken and then choosing the pilot technique required to fly that path or by defining the method of flying and working backward to determine the resultant flight path.

The desired profile is constrained by many factors, some of which

are shown directly on the trim-maps. For example, for the Harrier the stabilizer position (δ_H) is critical because there is only marginal nose-down pitching moment available. On the δ_H trim-maps (Figures 66, 73, 80, 87, 94, and 101) it can be seen that the stabilizer limit of +11.25 degrees is exceeded for several speeds and nozzle positions. This means that there is insufficient nose-down trim moment available at these flight conditions, not even considering the need for a control margin. Similarly, angle of attack (α) and thrust (T) limits are also constraints on the transition profile. Obviously the maximum gross thrust available is a limiting factor and the maximum angle of attack should be kept below buffet (16-18°). Thrust impact on engine life and fuel consumption are also considerations. Fuel consumption depends on gross thrust, which in turn depends on the deceleration profile to hover (Reference 8). Therefore, accurate flight path control is not only important for safety reasons but is also important for fuel considerations. Pilot visibility makes it desirable that the aircraft maintain a relatively low pitch attitude so that the pilot has a good view over the nose.

In a landing transition, deceleration and descent trim-maps are generally of the greatest interest. It should be noted that a deceleration of 0.1 g with the flight path angle (γ) equal to zero results in essentially the same trim-maps as zero deceleration and $\gamma = -0.1$ radian because the component of weight along the flight path in a descent of $\gamma = -0.1$ rad is equal to 0.1 times the aircraft weight. This equivalence is demonstrated by Figures 79 through 85 and Figures 86 through 92 which show the trim-maps for $\gamma = -0.1$ rad, $\dot{u}_v = 0.0$ and $\gamma = 0.0$, $\dot{u}_v = -0.1g$ respectively. Therefore, for small angles the sum of the flight path angle in radians and the

acceleration in g's is an important characteristic of the trim-maps. For example, a set of $\gamma = -0.1$ rad., $\dot{u}_v = -0.2$ g trim-maps is nearly identical to the $\gamma = -0.2$ rad., $\dot{u}_v = -0.1$ g (sum = -0.3) trim-maps, therefore only one of the two sets needs to be computed.

Control Moment Available

The critical speeds in the transition of the AV-8A Harrier are between approximately 225 ft/sec and 125 ft/sec because of the marginal nose-down control moment available in this range. At the higher speeds the control moment is provided mostly by the aerodynamic force acting on the horizontal tail. At low speeds the pitching moment is produced by the reaction control system which loses effectiveness at higher speeds (Figure 57) because the freestream deflects the RCS exhaust and changes the effective exhaust angle. In the 225 to 125 ft/sec speed range the aerodynamic pitching moment due to stabilizer deflection is decreasing while the RCS pitching moment is not yet strong enough to make up for the loss. Figures 61 and 62 demonstrate this problem. At 250 ft/sec the stabilizer produces almost 2400 ft-lb per degree of δ_H deflection. With the trailing edge full down (11.25°) this results in a pitch-down moment of almost 12600 ft-lb. This decreases to less than 4725 ft-lb at 150 ft/sec, a loss of about 7875 ft-lb of aerodynamic pitching moment. Figure 62 shows that the pitching moment available from the reaction control system increases from about 1700 ft-lb at 250 ft/sec to 4400 ft-lb at 150 ft/sec, an increase of 2700 ft-lb. Therefore, slowing down from 250 to 150 ft/sec, there is a net loss of over 5000 ft-lb in the available pitching moment.

Two critical parameters affecting the required trim moment in this speed range are the speedbrake deflection and the effects of thrust.

Speedbrake Effects

Without the speedbrake extended the aircraft exhibits an undesirable oscillatory roll mode at slow speeds. The speedbrake is extended on approach not for its drag but because it alters the airflow around the ventral fin (Reference 9).

As mentioned before, the limited nose-down pitching moment available is a quite stringent constraint on how the transition may be flown with the AV-8A. A speedbrake deflection of 25° (the data used in this report was for 30° deflection) causes an unfavorable nose-up aerodynamic pitching moment equivalent to about 3° stabilizer deflection at $\alpha = 4^\circ$ and 1° stabilizer deflection at $\alpha = 8^\circ$ (Figure 51). With the speedbrake fully extended (66°) the ΔC_m due to speedbrake is nose down approximately -0.02 , (Reference 5, flaps & U/C up, $\theta_j = 0$) and equivalent to about one degree stabilizer deflection. Therefore it would be desirable to use full speedbrake deflection during transition if it could be established that this would stabilize the oscillatory roll as well as the 25° deflection. As the aircraft was decelerated to below the critical speed range the speedbrake would then be retracted back to 25° to keep it from hitting the ground at touchdown.

Thrust Effects

The pitching moment varies significantly as a function of the main nozzle thrust, T . At low thrust the bypass airflow (fan exhaust) produces more thrust than the turbine exhaust. Since the fan exhaust flows out the front nozzles and the turbine exhaust out the aft nozzles, a significant nose up moment is created. Figure 59 shows that the ratio of fan/turbine thrust decreases as the total thrust (or RPM) increases, and as a result

the nose-up moment changes to a nose-down moment. The variation of the pitching moment with thrust is shown in Figure 63. Because of the marginal nose-down moment available it would be advantageous to run the engine at a high thrust to get the benefit of the nose-down moment due to thrust. Running the engine at higher RPM also increases the thrust of the RCS, enabling the aft pitch thruster to produce more nose-down moment than at low thrust settings.

While running the engine at higher thrust levels improves the control problem it conflicts with one objective of landing; that is, to descend and decelerate using as little fuel as possible. Using thrust greater than about 92% also decreases engine life. This should be avoided in landing transitions as much as possible in order to conserve engine life for take-off and combat. Nevertheless, a trade-off between fuel economy and an improved control margin is possible.

Minimum Fuel Consumption

The thrust trim-maps indicate implicitly the trim points for minimum fuel consumption flight. They are simply the θ_j at each airspeed requiring the least thrust. The minimum thrust points in the trim-maps (Figs. 67, 74, 81, 88, 95, 102) are determined by the $\alpha = 20^\circ$ truncation. Allowing for an α margin to stall, a much lower value of α must be cross-plotted on the thrust curves. As an example, in Figure 95 the $\alpha = 12^\circ$ values for various θ_j are indicated by X-es; in the decelerating-descending flight of that Figure, the X-es denote the truncation points of the thrust curves for $\alpha = 12^\circ$. A minimum thrust program with this α constraint amounts to flying at this angle of attack essentially throughout the transition. In

order to establish the control deflections needed for such a transition, X -es corresponding to $\alpha = 12^\circ$ are also shown in the δ_H curves in Figure 94. The minimum thrust point at $\theta_j = 80^\circ$ clearly would not leave an adequate control margin. This graph indicates that below about 175 ft/sec the minimum thrust policy should be abandoned in favor of an improved control margin. This illustrates how the trim-maps can be used in constructing transitions, combining requirements and constraints.

Sample Transition Profile

In this section the trim-maps are used to study a particular transition. In this case the flight program is known and the trim-maps will be used to illustrate how the aircraft is flown and the pilot technique involved.

The sample transition profile is the one presently being adopted for use by the United States Marine Corps for shipboard operations. This profile is shown in Figure 64. Beginning at 12 nautical miles (nm) the aircraft is at 1200 ft, 340 ft/sec, flaps and undercarriage down, and nozzles aft. The aircraft is then slowed to approximately 290 ft/sec and the nozzles rotated to 20° by the time it is 8 nm from the ship. Then from 8 to 4 nm the pilot flies a constant-speed descent to about 450 ft altitude and levels out. At 4 nm and 270 ft/sec the pilot puts the nozzles down to 40° and further decelerates to about 240 ft/sec by the time he is 1 nm from the ship (still at 450 ft). At this point the final descent is begun. The nozzles are lowered to 81° and the pilot simultaneously decelerates and descends to a hover above the ship.

The final mile of the transition is by far the most challenging so it will be traced on the trim-maps.

At 1 nm:

$$V_{\infty} = 240 \text{ ft/sec}$$

$$\theta_j = 40^\circ$$

$$h = 450 \text{ ft}$$

On Figures 72 through 79 point "a" represents the aircraft flight conditions for straight and level, unaccelerated, flight at 240 ft/sec and $\theta_j = 40^\circ$. From these trim-maps it can be seen that

at point a, $V_{\infty} = 240 \text{ ft/sec}$, $\dot{u}_v = 0.0 \text{ g}$, $\gamma = 0.0 \text{ rad}$, $\theta_j = 40^\circ$:

$$\alpha = 9^\circ; \delta_H = 3^\circ; \theta = 9^\circ;$$

$$T/W = 0.48; L/W = 0.65; D/W = 0.205; V_j/V_{\infty} = 0.28$$

The angle of attack found on the trim-map agrees closely with the actual approach angle of attack in that the Marine Corps pilots attempt to keep α constant at 8° .

At this point the nozzles are rotated down to 80 degrees and the pilot begins a decelerating descent. If the pilot held the angle of attack constant while he rotated the nozzles the aircraft would begin to decelerate at 6.4 ft/sec^2 (0.2 g) and descend at $\gamma = -5.7^\circ$ (-0.1 rad) (as shown by point b in figures 100 through 106). Summarizing these trim-maps:

at point b, $V_\infty = 240$ ft/sec, $\dot{u}_v = -0.2g$, $\gamma = -0.1$ rad, $\theta_j = 80^\circ$

$\alpha = 9^\circ$, $\delta_H = 4.75^\circ$

$T/W = 0.47$, $L/W = 0.55$, $D/W = 0.195$

The trim-maps verify that this is a good place to rotate the nozzles from 40° to 80° because α and thrust remain essentially unchanged. Therefore, besides rotating the nozzles, the pilot only needs to move the stick forward enough to move the elevator 1.75° to change from one quasi-equilibrium trim point to another.

Examining further Figures 100 through 106 it can be seen that maintaining the -0.2 g deceleration and -0.1 rad flight path angle requires increasing α and δ_H , and at 160 ft/sec α would be 16° and δ_H would be 10.75° , both dangerously high. Angle of attack would be approaching stall and δ_H would be approaching the forward stick stop (11.25°). Examining the trim-maps for unaccelerated straight and level flight (Figures 72 through 78) and for decelerating descent at $\dot{u}_v = -0.1$ g, $\gamma = -0.1$ rad (Figures 93 - 99), it can be seen that the flatter the flight path and the less the deceleration, the less the stabilizer required. This is caused mainly by the fact that the trim condition for lower deceleration requires more thrust (see Figs. 95 and 102), which decreases the nose up moment due to thrust.

As a result, assuming the maximum α allowed to be about 12.5° , the $\dot{u}_v = -0.2$ g, $\gamma = -0.1$ rad flight may only be maintained until 200 ft/sec is reached (point c) and the deceleration/descent must then be decreased.

Referring to Figures 100 - 106:

$$\text{at point c, } V_{\infty} = 200 \text{ ft/sec, } \dot{u}_V = -0.2 \text{ g, } \gamma = -0.1 \text{ rad, } \theta_j = 80^\circ$$
$$\alpha = 12.5^\circ; \delta_H = 6.25^\circ; \theta = 7^\circ$$
$$T/W = 0.55; L/W = 0.46; V_j/V_{\infty} = 0.37; D/W = 0.175$$

To fly from the conditions at point b to point c the pilot would simply continue to move the stick slowly forward to 6.25° stabilizer angle, allowing the angle of attack to increase to 12.5° . During this time thrust must be increased by a small amount (0.08 T/W).

At this point the angle of attack must either be held constant or be reduced. This means the nozzle deflection must either be increased or the deceleration/descent reduced. Since the Marine Corps pilots do not move the nozzles past 82° (hover stop) it is therefore evident that the deceleration/descent angle is reduced. In addition, the pilots are constantly trying to keep the angle of attack near 8° and as hover is approached they decrease the deceleration while flattening the flight path.

This means the pilot is trying to fly smoothly between the $\alpha = 8^\circ$ trim points on the $\dot{u}_V = -0.1 \text{ g, } \gamma = -0.1 \text{ rad}$ trim-maps (Figures 93-99) and the $\dot{u}_V = 0.0 \text{ g and } \gamma = 0.0 \text{ rad}$ trim-maps (Figures 72-78). From 200 ft/sec to 100 ft/sec, the pilot should take special care to keep the angle of attack at 8° or above in order that the pitch-up due to the speedbrake (Figure 51) is avoided. This speed range can be traced on the trim-maps in the following way. Comparing Figures 93 and 72, note that points d and e represent the $\theta_j = 80^\circ, \alpha = 8^\circ$ trim points on the α trim-maps for $\dot{u}_V = -0.1 \text{ g, } \gamma = -0.1 \text{ rad, and for } \dot{u}_V = 0.0 \text{ g, } \gamma = 0.0 \text{ rad, respectively.}$ Point d shows trimmed decelerating, descending flight at 185 ft/sec at an

angle of attack of 8° . As the deceleration and descent angle are decreased, the airspeed for trimmed flight at $\alpha = 8^\circ$ with the same θ_j is decreased to 50 ft/sec when steady level flight is reached (point e). The airspeed for trimmed flight at 8° for $u_v = 0.05$ g, $\gamma = -0.05$ rad can be estimated to be about 118 ft/sec $[(185 + 50)/2]$.

Using this information, the pilot technique and flight conditions for flying this path can be deduced. From the conditions given at point c, the stick will have to be moved to almost full forward at about 200 ft/sec as the amount of deceleration is decreased to -0.1 g (point d, Fig. 94). As the deceleration and flight path angle are further decreased, the stick will be very slowly moved aft until about 150 ft/sec is reached when it should be moved more rapidly aft in the 150 ft/sec to 75 ft/sec speed range. In the 75 ft/sec to 50 ft/sec speed range, the stick would continue to be moved slightly aft to about $\delta_H = 3.25^\circ$. During this time, thrust would be initially rapidly increased to about $T/W = 0.8$ and then more slowly increased reaching $T/W \approx 1$ at about 100 ft/sec.

After level unaccelerated flight is reached at 50 ft/sec (point e) simply raising the angle of attack to 10° will slowly bring the aircraft to hover (point f on Figures 72-78).

This example illustrates how the trim-maps can be used for a detailed analysis of a prescribed transition. In the AV-8A the control power limitation and the simplest possible piloting technique are overriding factors. In future VTOL aircraft with no severe control limitation and with various degrees of automatic flight control, the trim-maps can be used to explore less constrained and potentially more efficient transition profiles.

CONCLUSIONS

A mathematical computer model, "HARRIER", of the AV-8A Harrier aircraft has been developed utilizing the concept of quasi-stationary flight in order to determine quasi-equilibrium values of flight variables and controls during accelerating-decelerating flights. Using available aerodynamic data via look-up schemes, "trim-maps" are computed which show the values of the longitudinal flight and control variables as functions of air-speed and thrust angle. These maps have been shown to be useful tools in piecing together transition profiles, taking into consideration various requirements and constraints.

The AV-8A is most difficult to control longitudinally in the speed range of approximately 225 to 125 ft/sec. Decelerating through this critical speed range the aerodynamic pitching moment from the stabilizer is decreasing as a function of dynamic pressure and the reaction control system has not yet become effective enough to make up for the loss. Considering that the transition is constrained by the available nose-down control moment, the moments caused by the speedbrake and the thrust become significant. Therefore, the transition should be flown with two major constraints in this speed range. First the angle of attack should be kept at or above 8° so that the nose-up pitching moment due to the speedbrake is not excessive. Second, deceleration through the critical speed range should be performed gradually to keep thrust up near the thrust required for level flight and therefore minimizing the nose up pitching moment due to thrust. This second constraint should be tempered, especially at higher landing weights, with the consideration of engine life.

Extending the speedbrake to the full-out position on approach would be beneficial in that it would change the pitch-up effect of the speedbrake to pitch-down, thereby alleviating the problem of marginal nose down moment available. After decelerating below 100 ft/sec the speedbrake should then be retracted to 25° to avoid hitting the ground at touchdown.

The final decelerating-descending phase of the present USMC approach profile has been analyzed in detail with the aid of the trim-maps. The technique of flying the transition as suggested by the trim-maps has been found in good agreement with the techniques actually used under the given constraints. This established confidence in both the mathematical model and in the trim-maps as tools for studying alternate transition profiles which might improve pilot work load and/or fuel efficiency.

REFERENCES

1. Shumpert, P. K., "Model Tests of Jet-Induced Lift Effects on a VTOL A/C in Hover", NASA CR-1297, March 1969.
2. Margason, R. J., "Review of Propulsion-Induced Effects on Aerodynamics of Jet V/STOL Aircraft", NASA TN-D 5617, 1970.
3. Viehweger, Gunter, "Flow Effects with Cross-blown Lifting Jets of V/STOL Aircraft and Their Reactions on the Aerodynamic Forces and Moments of the Airplane", translated from German, NASA TM-75143.
4. Kotansky, D. R., Durando, N. A., Bristow, D. R., and Saunders, P. W., "Multi Jet Induced Forces and Moments on VTOL Aircraft Hovering In and Out of Ground Effect", McDonnell Douglas Corp., Report Number NADC-77-229-30, For the Naval Air Development Center, Warminster, Pa., June 1977.
5. McDonnell Douglas Corporation, "AV-8A Aerodynamic Characteristics", Report MDC A1410 Revision A, St. Louis, Mo., 29 February 1972.
6. McDonnell Douglas Corporation, "AV-8A Basic Aerodynamic Data", Report MDC A1400 Revision B, St. Louis, Mo., 20 Dec. 1972.
7. Nave, Ronald L., "A Computerized VSTOL/Small Platform Landing Dynamics Investigation Model", Naval Air Development Center Report, NADC-77024-30, Warminster, Pa., 30 Sept. 1977.
8. E. Huntley, "Optimal Paths for Minimizing Landing Transition Distance for a Jet-Lift VTOL Aircraft", The Aeronautical Journal of the Royal Aeronautical Society, May 1972.
9. "The Hawker Siddeley Harrier", Hawker Siddeley Aviation Limited, Kingston upon Thames, U.K., Dec. 1969, Page 81.
10. Marinucci, Claudio, "A Nonlinear Force Balance Model for a Tilt-Rotor Airplane in Transition", MAE Report No. 1101-T, Princeton University May 1973.
11. Bellman, R. E. and Kalaba, R. E., editors. Quasilinearization and Nonlinear Boundary - Value Problems, The RAND Corporation, American Elsevier Publishing Company, Inc., New York, 1965, pp 7-12 and 21,22.

12. Templin, R. J., "A Momentum Rule for Optimum Aircraft Performance in the V/STOL Transition Regime", National Aeronautical Establishment, Ottawa, Canada, January 1967.
13. Huntley, E., "Optimal Paths for Minimizing Landing Transition Distance for Jet-Lift VTOL Aircraft", RAE-TR-70134, Royal Aircraft Establishment, Farnborough, United Kingdom, July 1970.
14. Schmidt, G., Weimann, A., "Fuel-Optimal Landings of Jet-Supported VTOL Aircraft", Dornier AG, Friedrichshafen, West Germany
15. Huntley, E., "Landing Transition Paths Which Optimize Fuel, Time or Distance For Jet-Lift VTOL Transport Aircraft In Steep Approaches", Sheffield University, United Kingdom.
16. McDonnell Douglas Corporation Report A1410, "AV-8A Aerodynamic Characteristics", 31 January 1972.
17. McDonnell Douglas Corporation Report A1411-B, "AV-8A Estimated Flying Qualities", 31 January 1972.
18. McDonnell Douglas Corporation Report A1400, "AV-8A Basic Aerodynamic Data", 6 December 1971.
19. McDonnell Douglas Corporation Report A3880, "AV-8A Aircraft Performance", 15 February 1976.
20. McDonnell Douglas Corporation Report A3828, "Analysis of Primary and Auxiliary Flight Control Systems for the AV-8A", 20 January 1976.

TABLE 1
Thrust to Weight Ratios and Time Limitations of
The Installed Pegasus 11 Engine*

THRUST RATING	% N_F	TIME LIMITATION	GROSS THRUST -165-	T/W @ 14000 lbs
Max. continuous	90	unlimited	12900	0.92
Maximum thrust	94.4	15 min.	15500	1.10
Normal lift, dry	100.0	2.5 min.	17700	1.26
Short lift, dry	102.7	15 sec.	18650	1.33
Normal lift, wet	104.1	1.5 min.	19300	1.38
Short lift, wet	105.8	15 sec.	19600	1.40

*Static, Sea Level Standard Day

TABLE 2
Summary of Trim-Map Flight Conditions

Figures	γ	\dot{u}_v (g)	\dot{w}_v (g)	v_∞ ft/sec	θ_j (deg)	δ_F (deg)
65-71	0.1	0.1	0	250-0	0-100	50
72-78	0	0	0	250-0	0-100	50
79-85	-0.1	0	0	250-0	0-100	50
86-92	0	-0.1	0	250-0	0-100	50
93-99	-0.1	-0.1	0	250-0	0-100	50
100-106	-0.1	-0.2	0	250-0	0-100	50

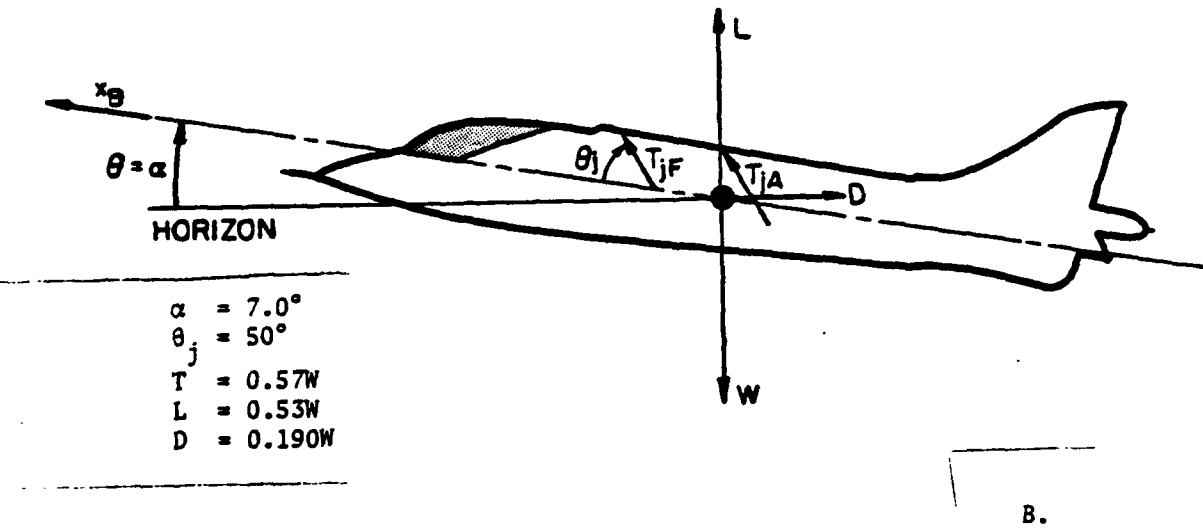
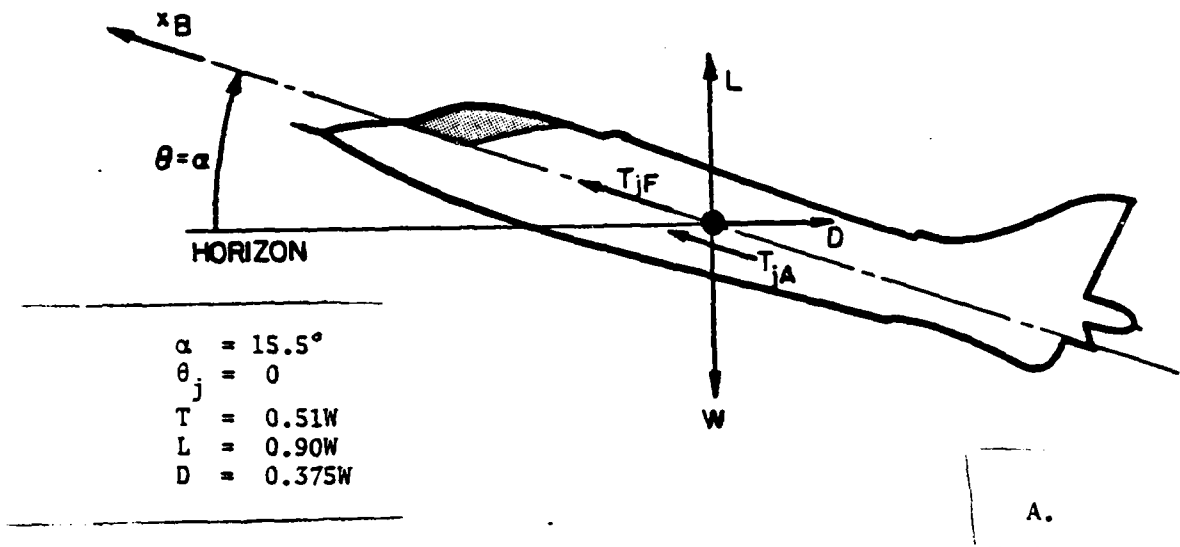


FIGURE 1 - Two Sets of Control Positions Resulting in the Same Trimmed Flight Condition, (Level Unaccelerated Flight $V_\infty = 220$ ft/s).

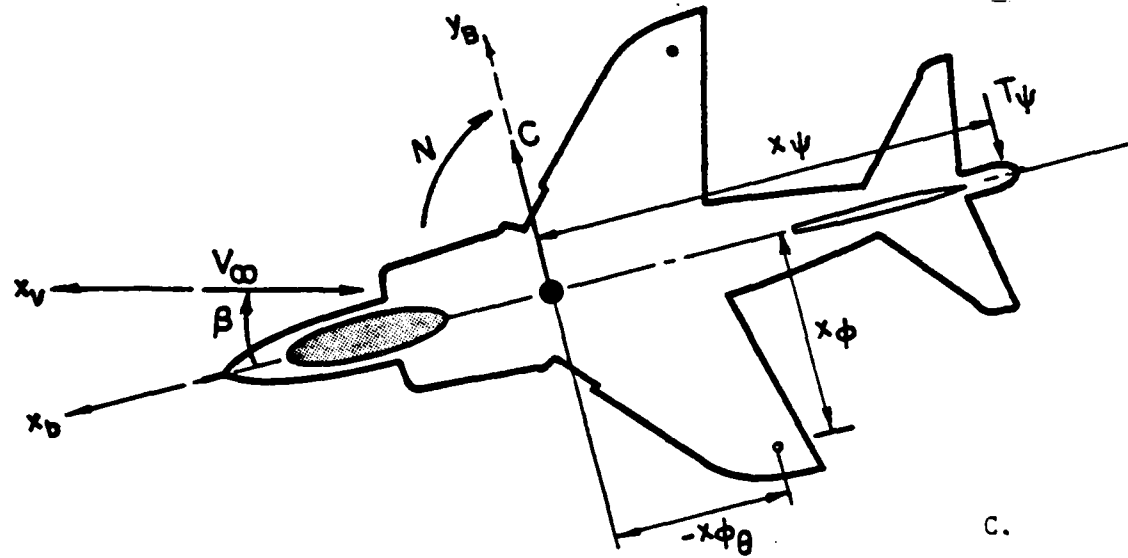
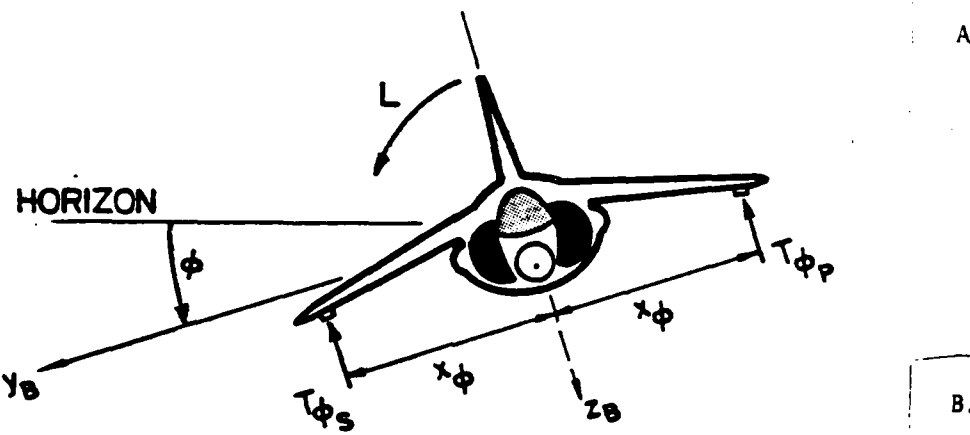
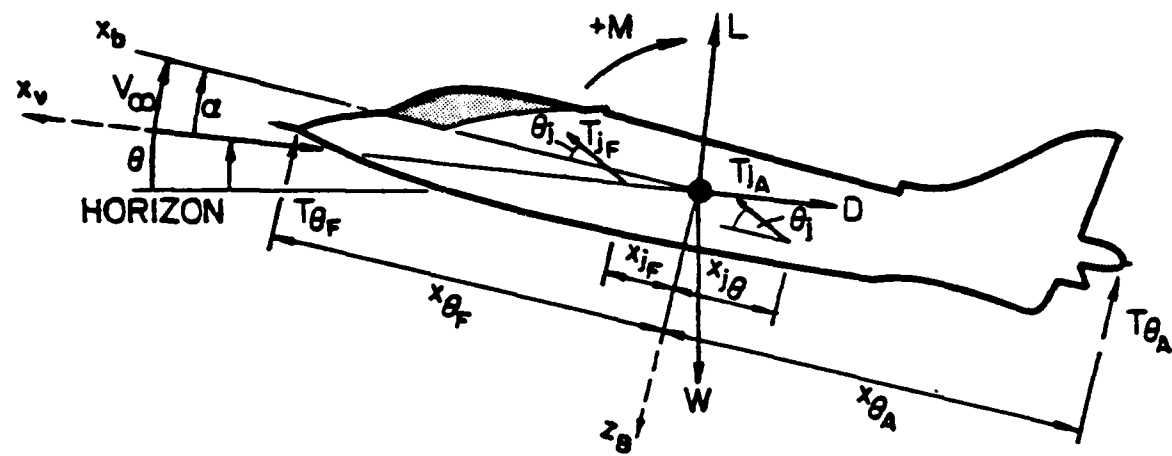


FIGURE 2 - AV-8A Harrier; Forces and Moments Acting on the Aircraft.

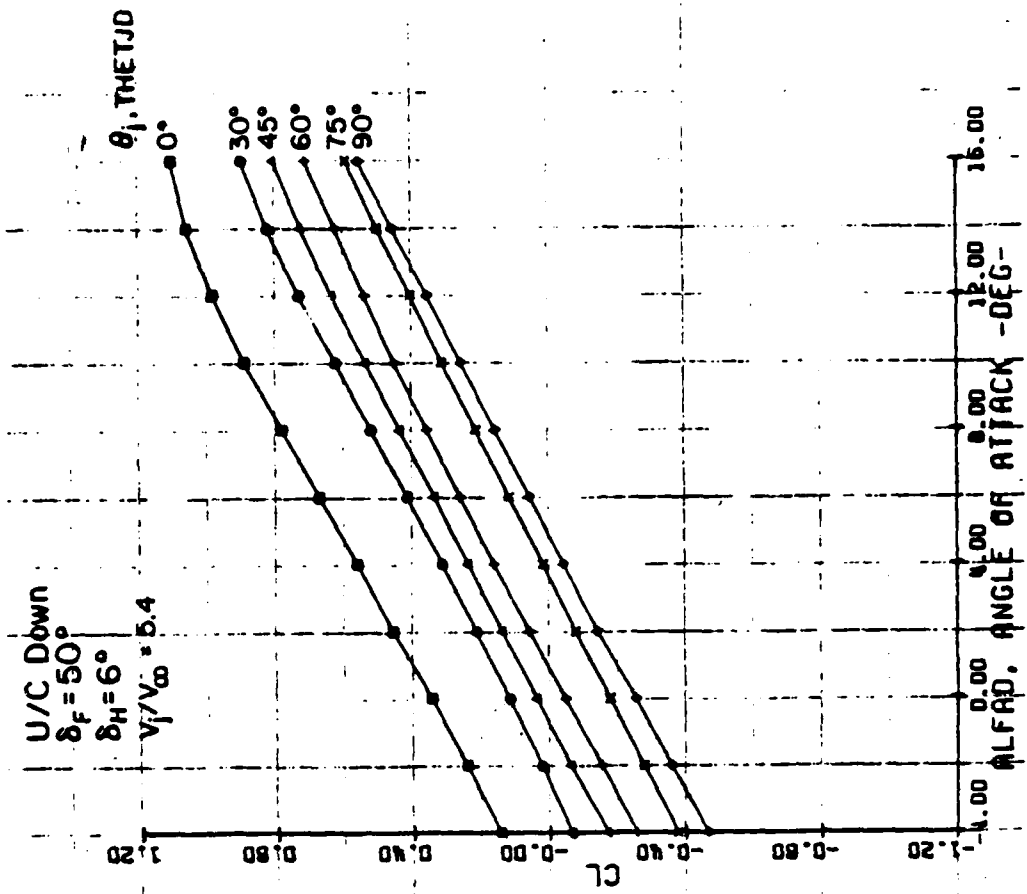
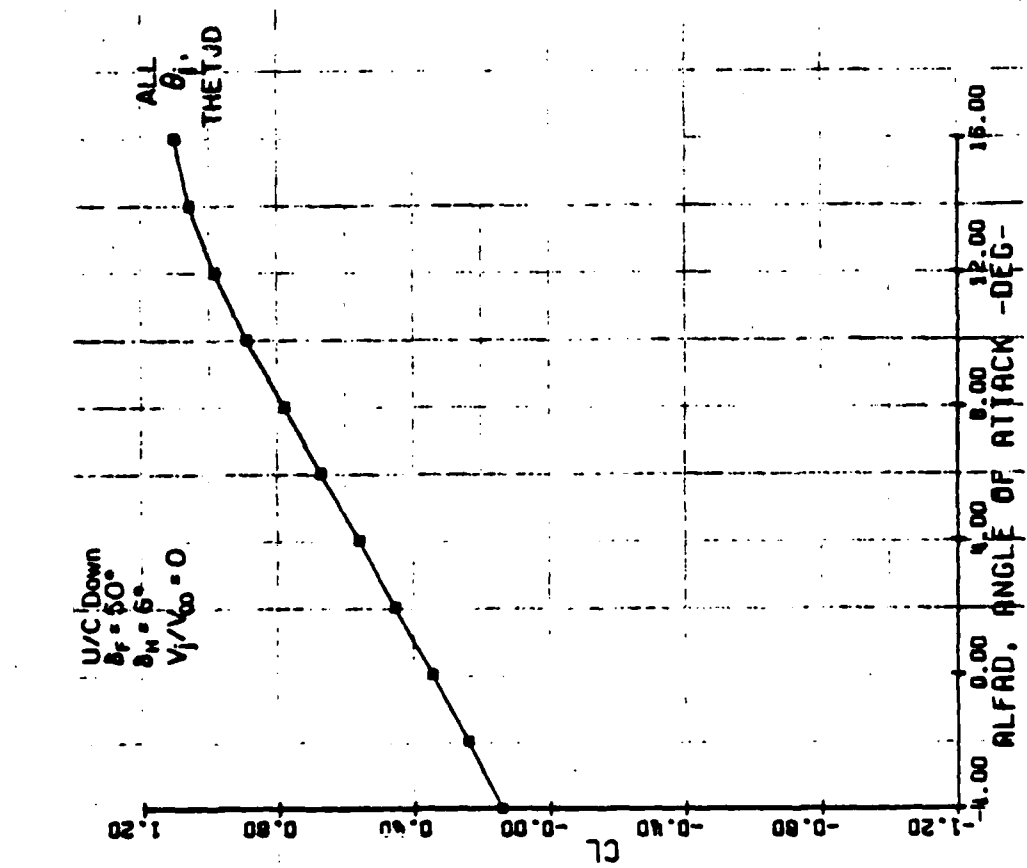


FIGURE 3 - AV-8A C_L _{wing-body} Without Wing/Jet Interaction (Ref. 5, p. 161).

FIGURE 4 - AV-8A C_L _{wing-body} With and Without Wing/Jet Interaction for Various θ_j . - $V_j/V_\infty = 5.4$;
 (Ref. 5, pp. 171-175).

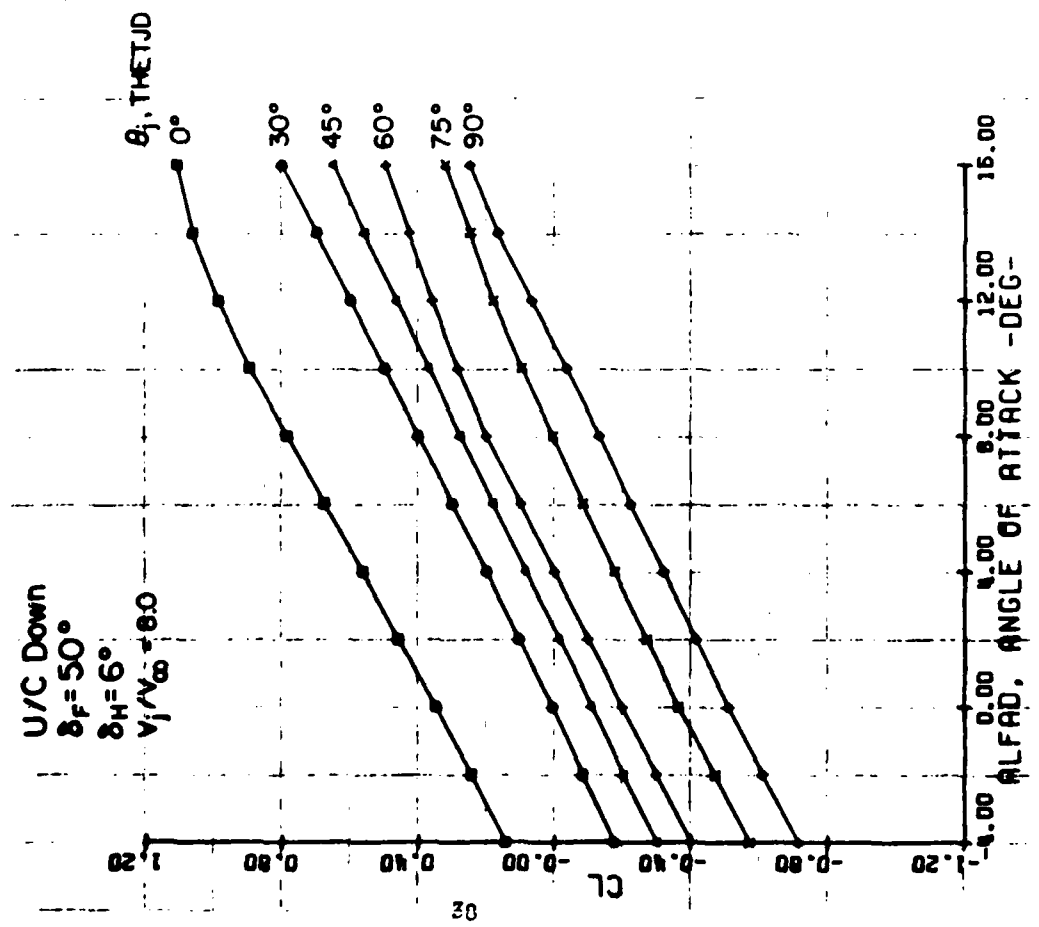
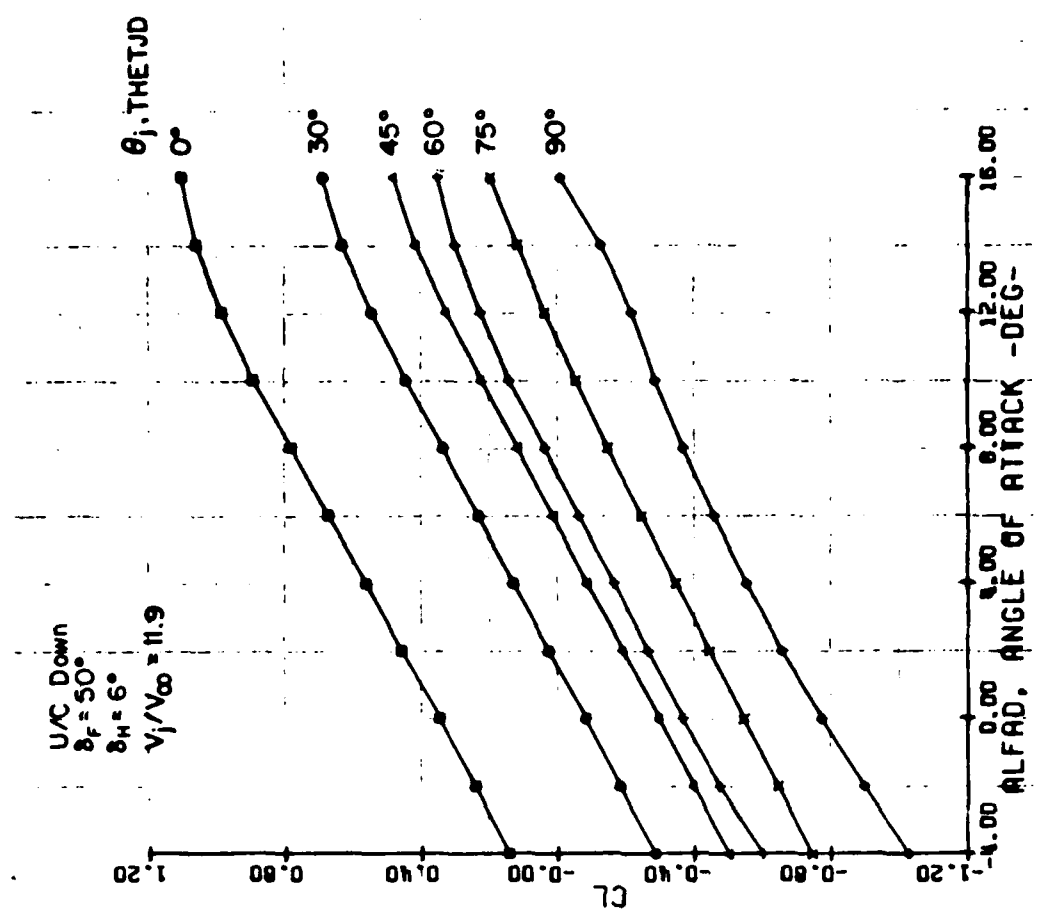


FIGURE 5 - AV-8 C_L _{wing-body} With and Without Wing/Jet Interaction for Various θ_j . $V_j/V_\infty = 8.0$ (Ref. 5, pp. 166-170).

FIGURE 6 - AV-8A C_L _{wing-body} With and Without Wing/Jet Interaction for Various θ_j . $V_j/V_\infty = 11.9$ (Ref. 5, pp. 162-165).

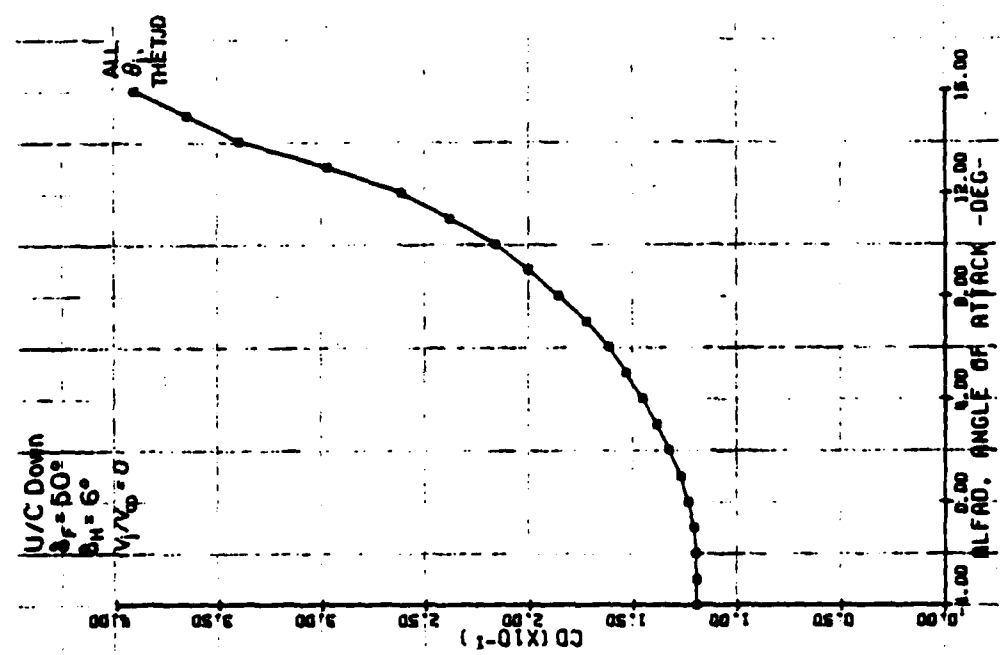


FIGURE 7 - AV-8A C_D wing-body interaction for $\alpha_j = 0.0$ (Ref. 5, p. 161).

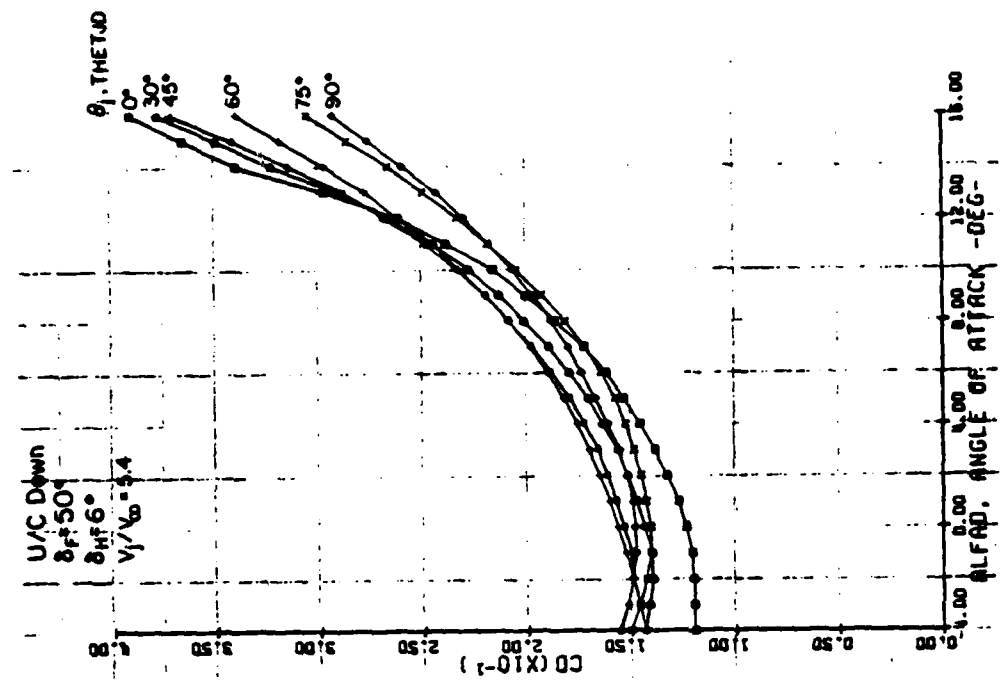


FIGURE 8 - AV-8A C_D wing-body interaction for various θ_j .
 $V_j/V_\infty = 5.4$ (Ref. 5, pp. 171-175).

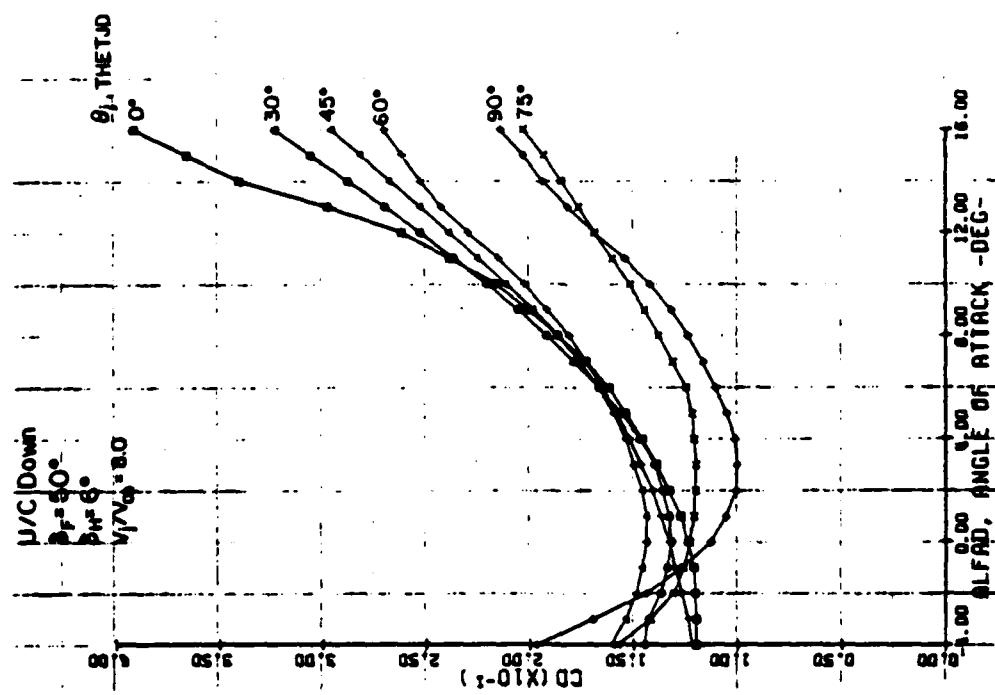


FIGURE 9 - AV-8A C_D _{wing-body} With and Without Wing/Jet Interaction for Various θ_j .
 $V_j/V_\infty = 8.0$ (Ref. 5, pp. 166-170).

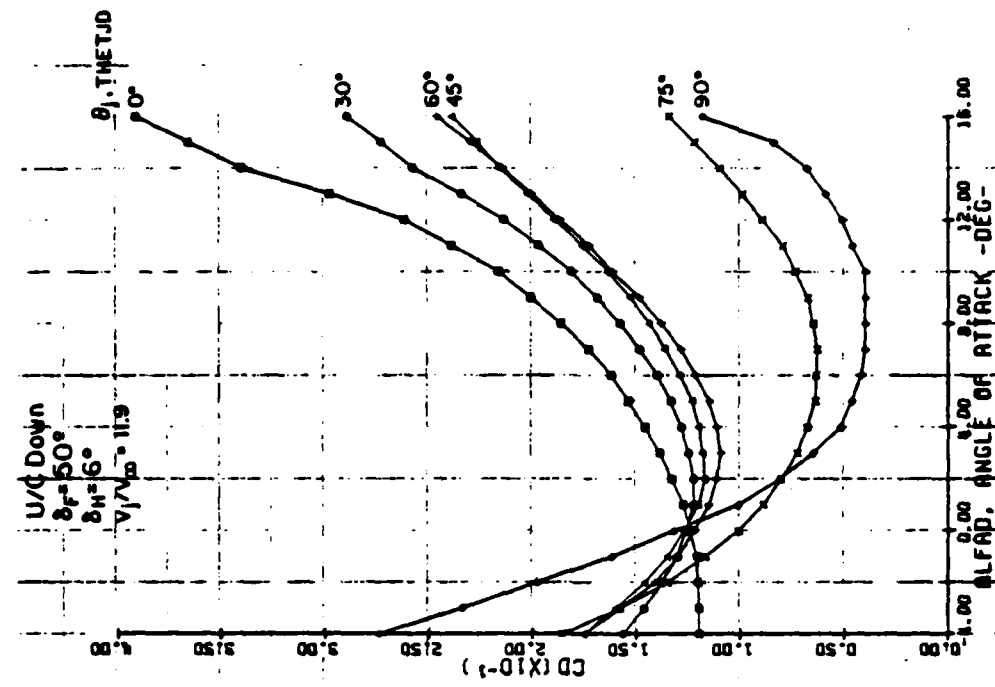


FIGURE 10 - AV-8A C_D _{wing-body} With and Without Wing/Jet Interaction for Various θ_j .
 $V_j/V_\infty = 11.9$ (Ref. 5, pp. 166-170).

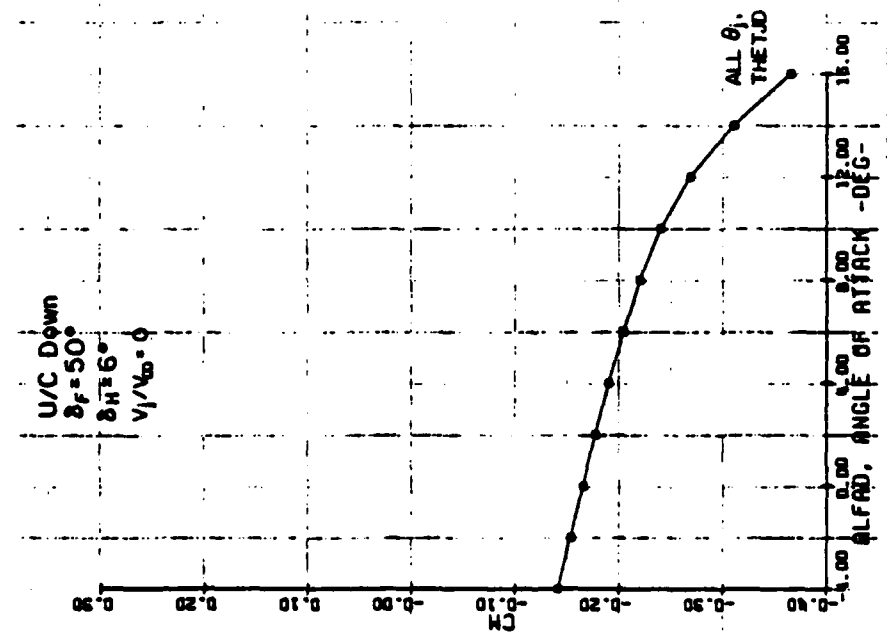


FIGURE 11 - AV-8A C_m _{wing-body} Without Wing/Jet
Interaction for All θ_j , $V_j/V_\infty = 0.0$
(Ref. 5, p. 161).

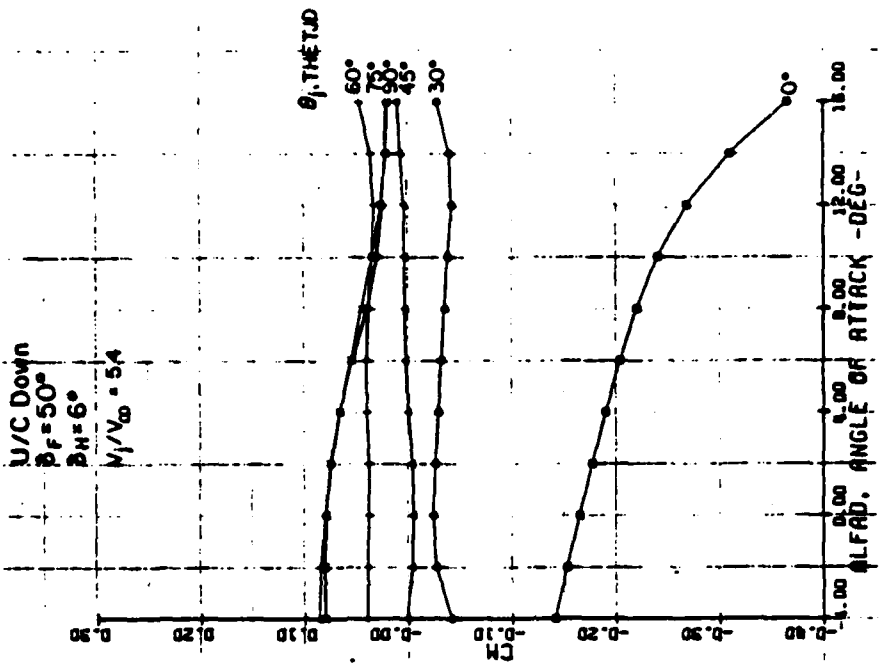


FIGURE 12 - AV-8A C_m _{wing-body} With and Without Wing/Jet
Interaction for All θ_j , $V_j/V_\infty = 5.4$
(Ref. 5, pp. 171-175).

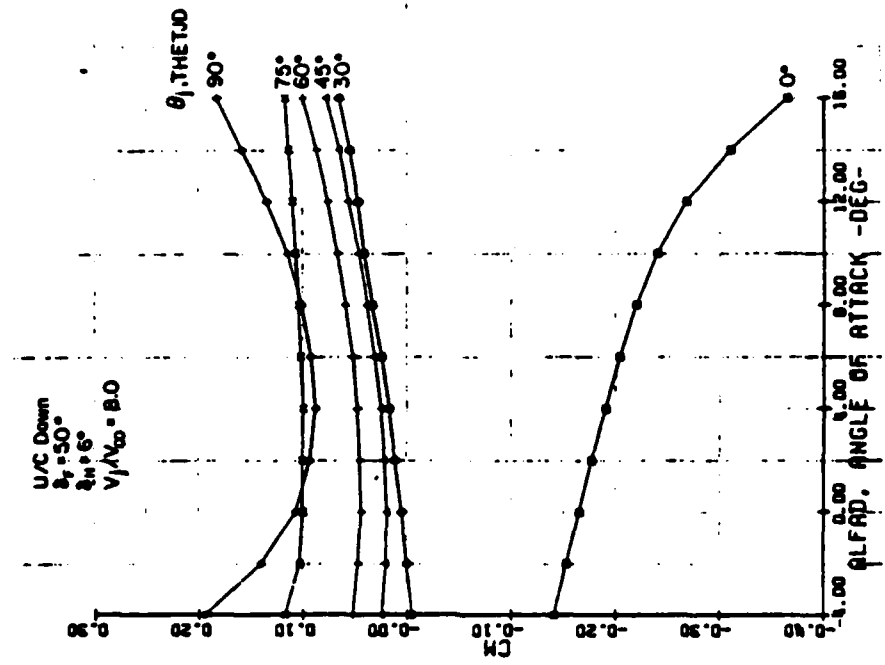


FIGURE 13 - AV-8A C_m wing-body With and Without Wing/Jet
Interaction for All θ_j , $V_j/V_\infty = 8.0$
(Ref. 5, pp. 166-170).

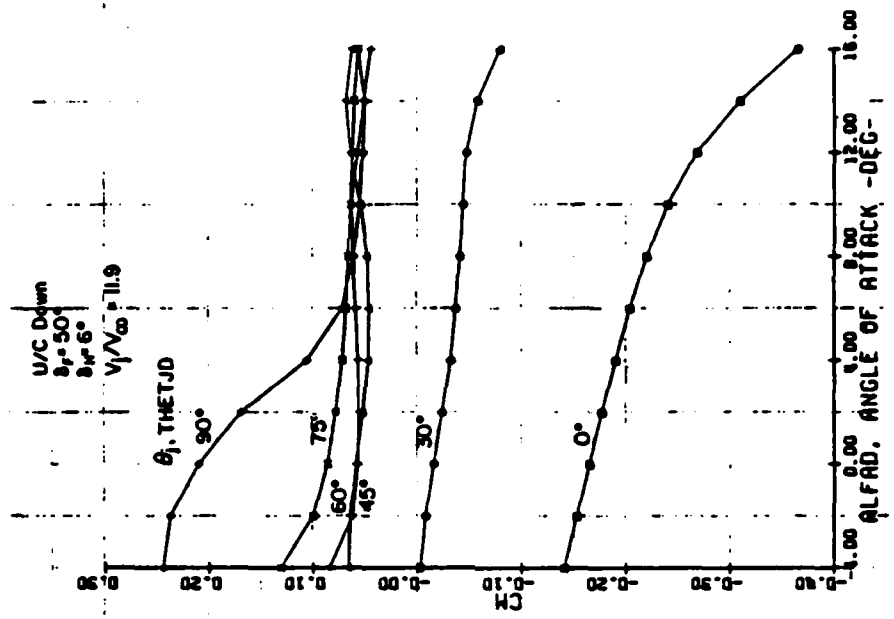


FIGURE 14 - AV-8A C_m wing-body With and Without Wing/Jet
Interaction for All θ_j , $V_j/V_\infty = 11.9$
Ref. 5, pp. 162-165).

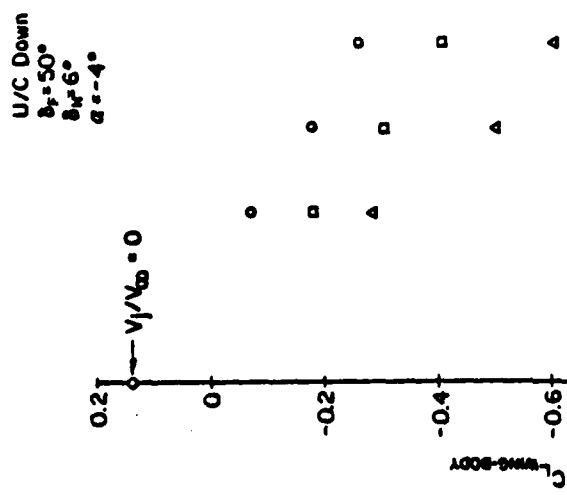


FIGURE 15 - AV-8A C_L With Wing/Jet Interaction.
 $\alpha = -4^\circ$.

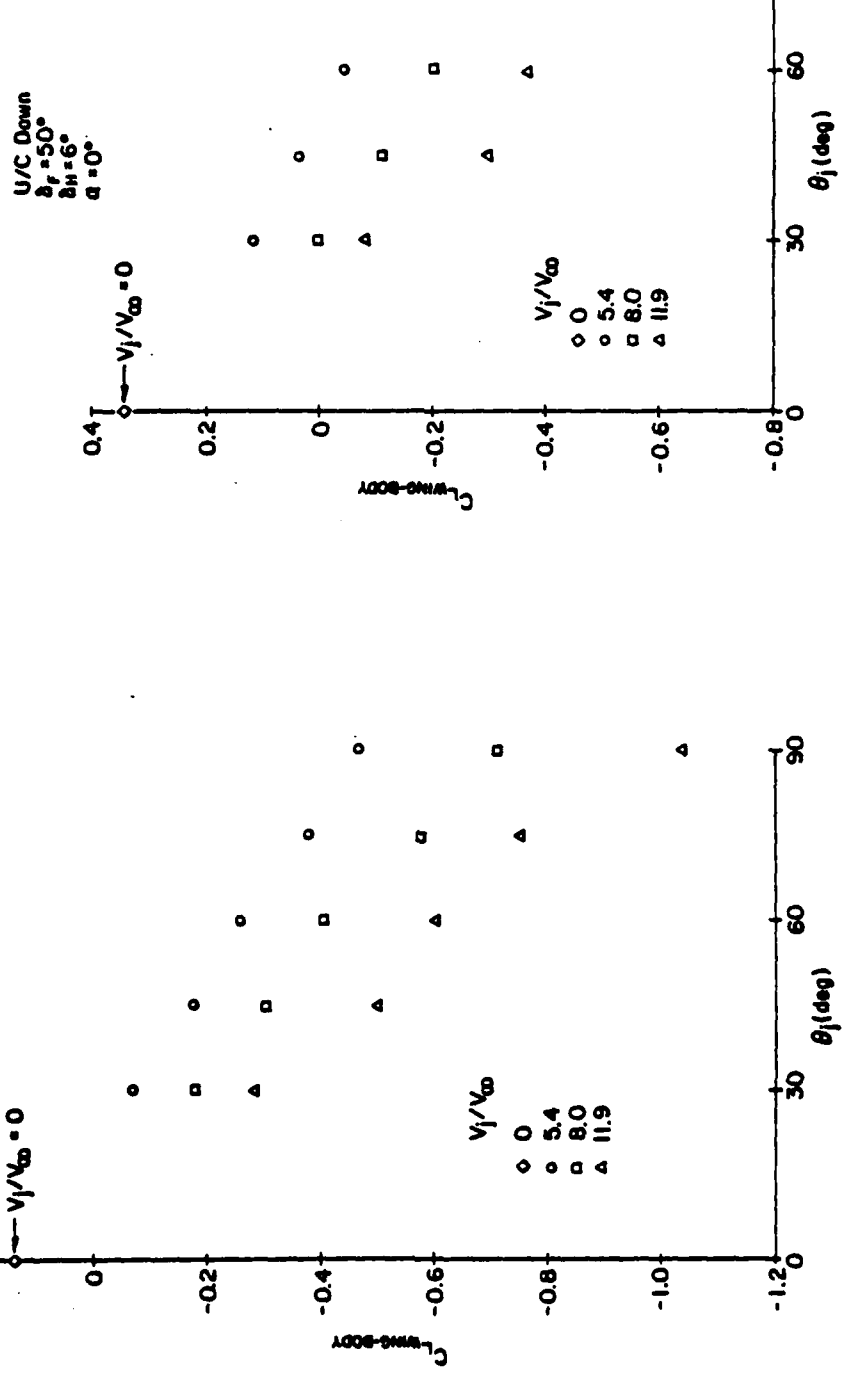


FIGURE 16 - AV-8A C_L With Wing/Jet Interaction.
 $\alpha = 0^\circ$.

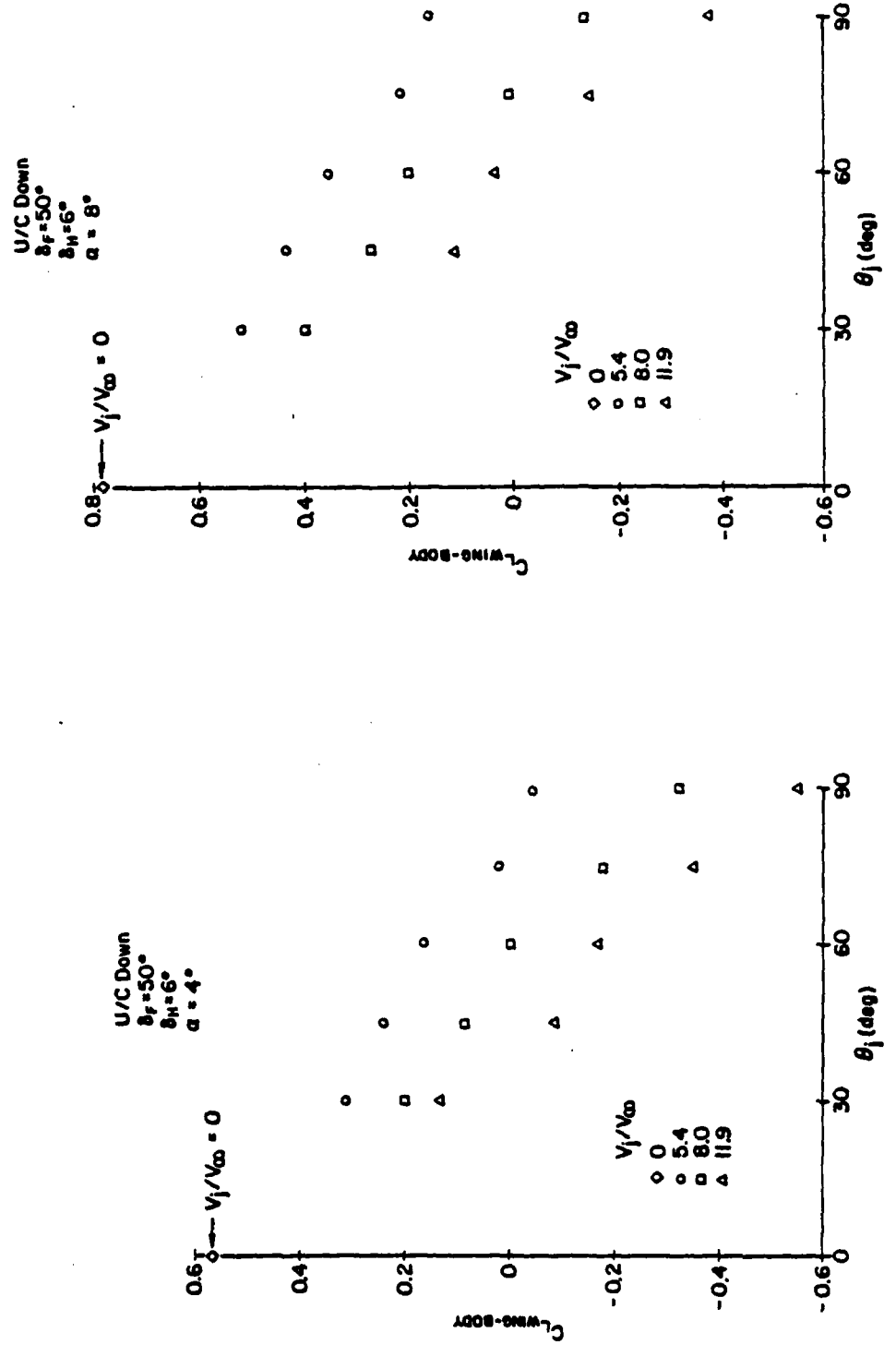


FIGURE 17 - AV-8A $C_{L_{\text{WING-BODY}}}$ With Wing/Jet Interaction.
 $\alpha = 4^\circ$.

FIGURE 18 - AV-8A $C_{L_{\text{WING-BODY}}}$ With Wing/Jet Interaction.
 $\alpha = 8^\circ$.

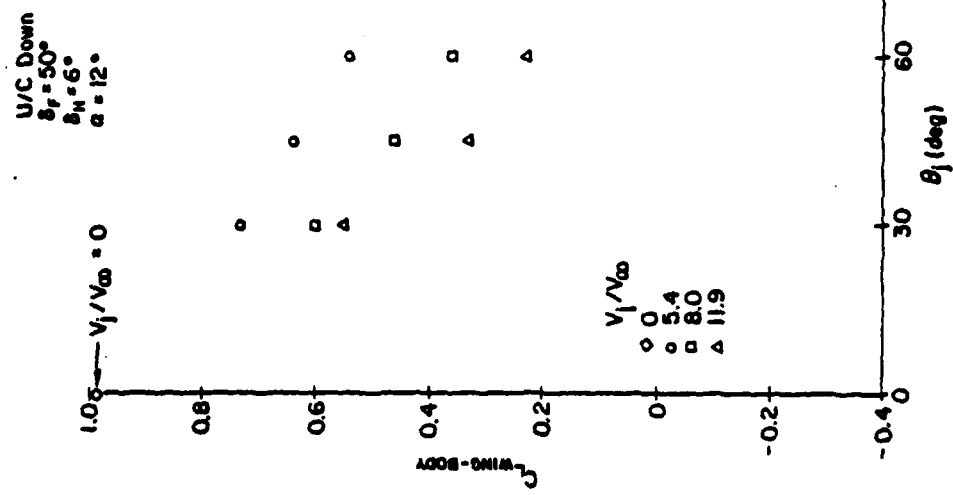


FIGURE 19 - AV-8A $C_{L_{\text{wing-body}}}$ With Wing/Jet Interaction.
 $\alpha = 12^\circ$.

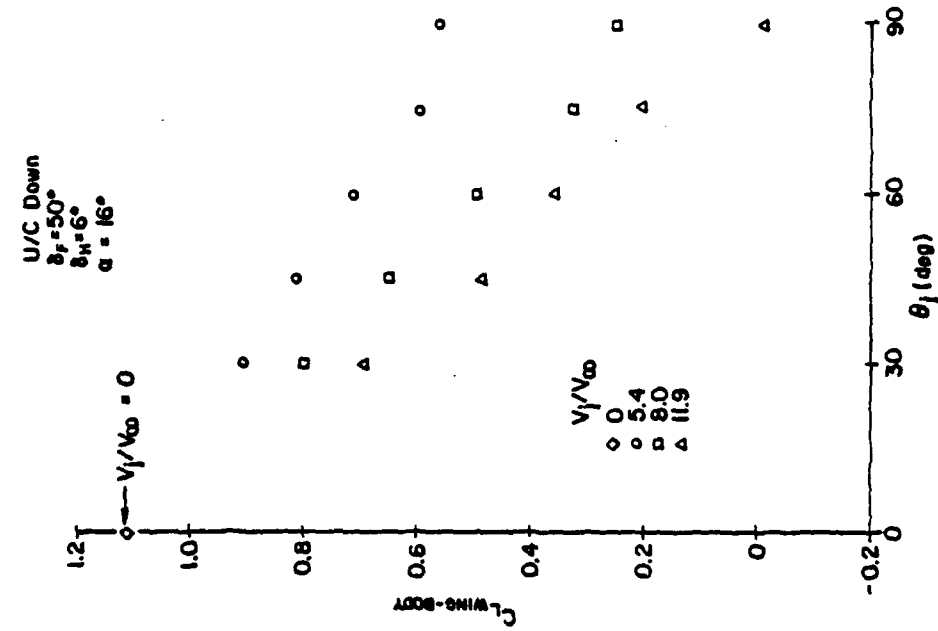


FIGURE 20 - AV-8A $C_{L_{\text{wing-body}}}$ With Wing/Jet Interaction.
 $\alpha = 16^\circ$.

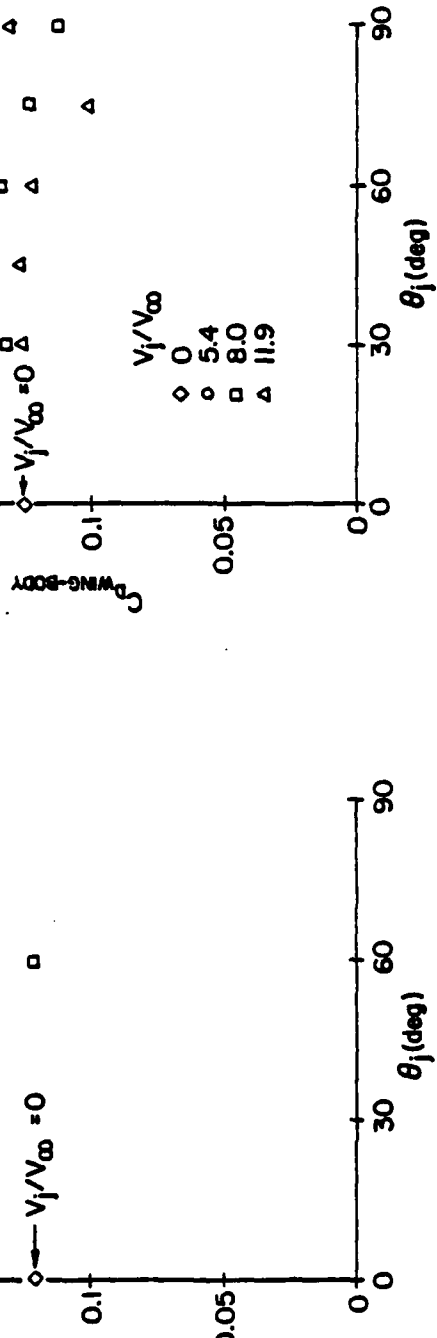
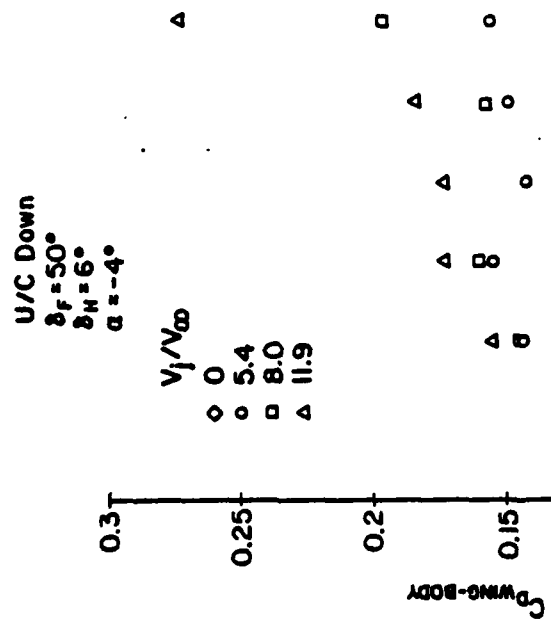


FIGURE 21 - AV-8A C_D _{wing-body} With Wing/Jet Interaction, $\alpha = -4^\circ$.

FIGURE 22 - AV-8A C_D _{wing-body} With Wing/Jet Interaction, $\alpha = 0^\circ$.

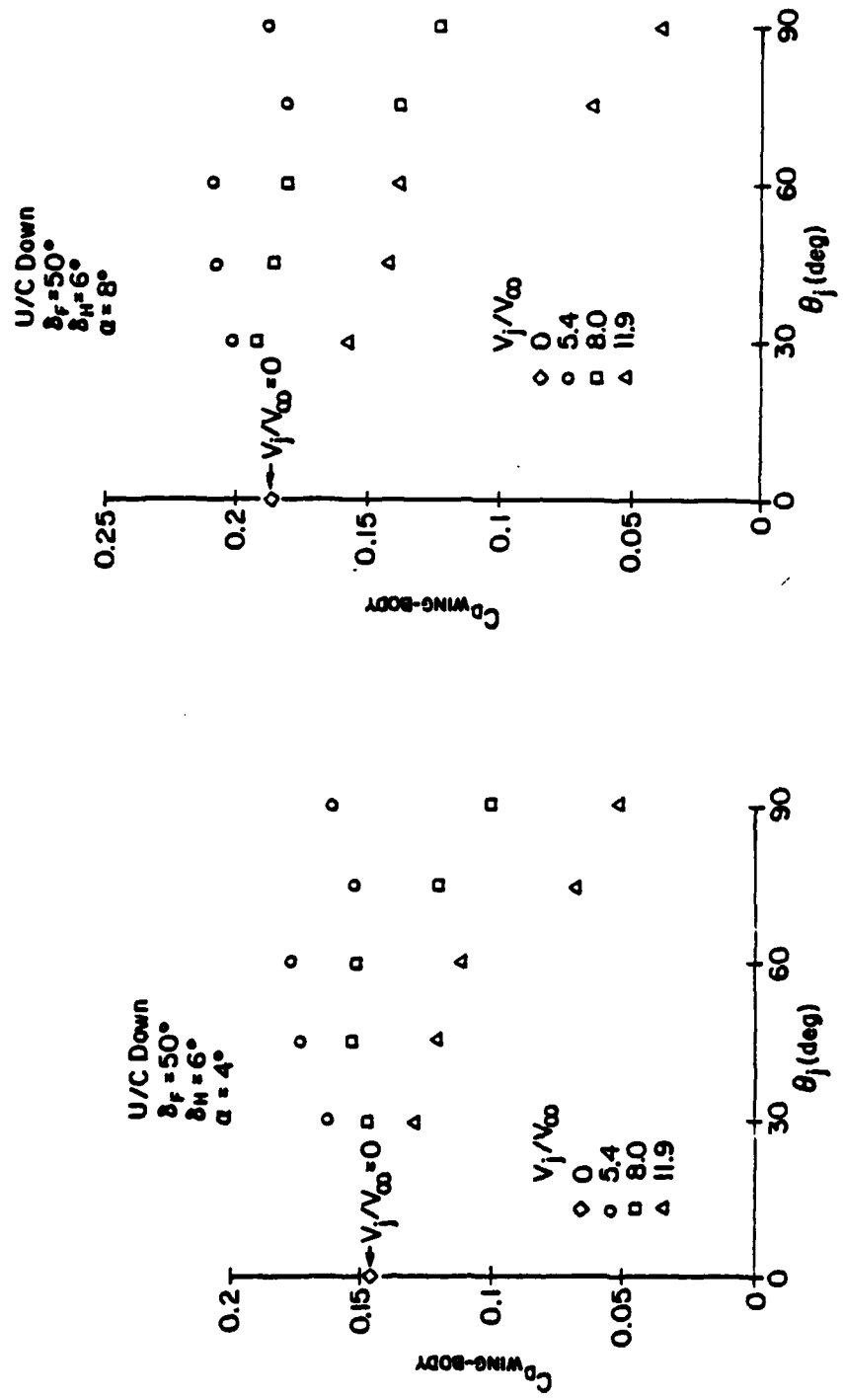


FIGURE 23 - AV-8A C_D wing-body With Wing/Jet Interaction, FIGURE 24 - AV-8A C_D wing-body With Wing/Jet Interaction, $\alpha = 8^\circ$. $\alpha = 4^\circ$.

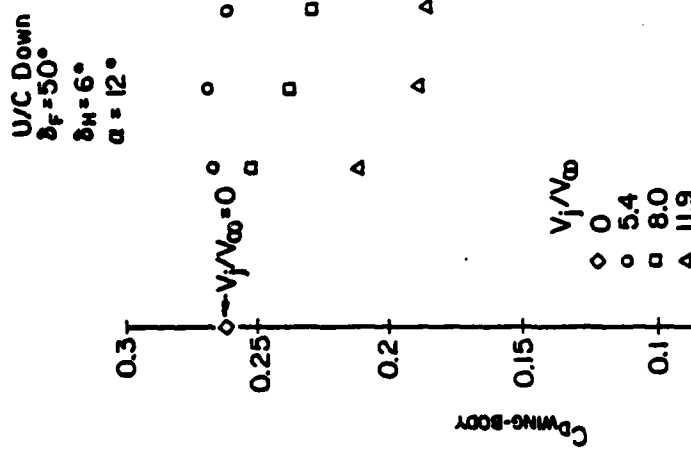


FIGURE 25 - AV-8A $C_D^{\text{WING-BODY}}$ With Wing/Jet Interaction,
 $\alpha = 12^\circ$.

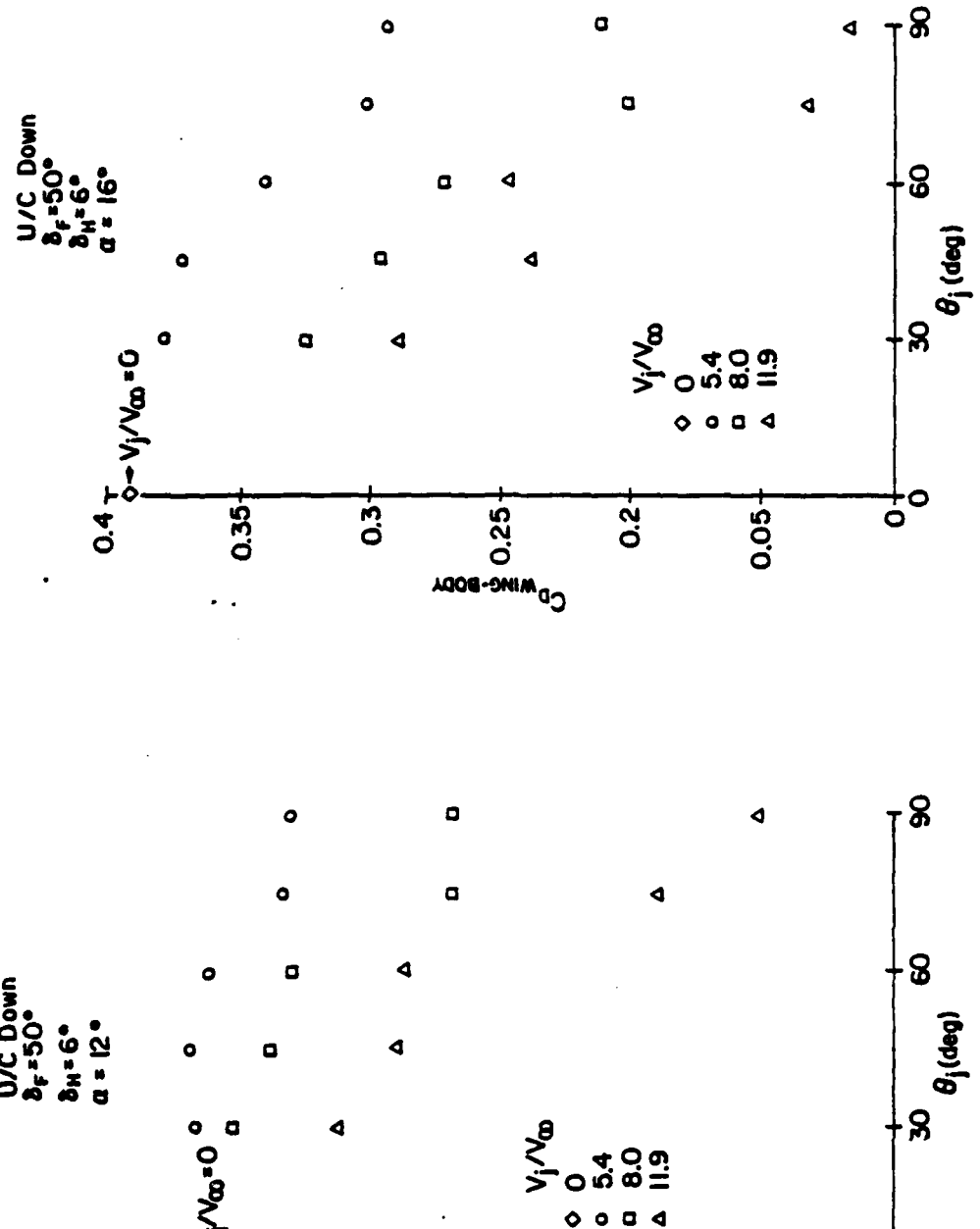


FIGURE 26 - AV-8A $C_D^{\text{WING-BODY}}$ With Wing/Jet Interaction,
 $\alpha = 16^\circ$.

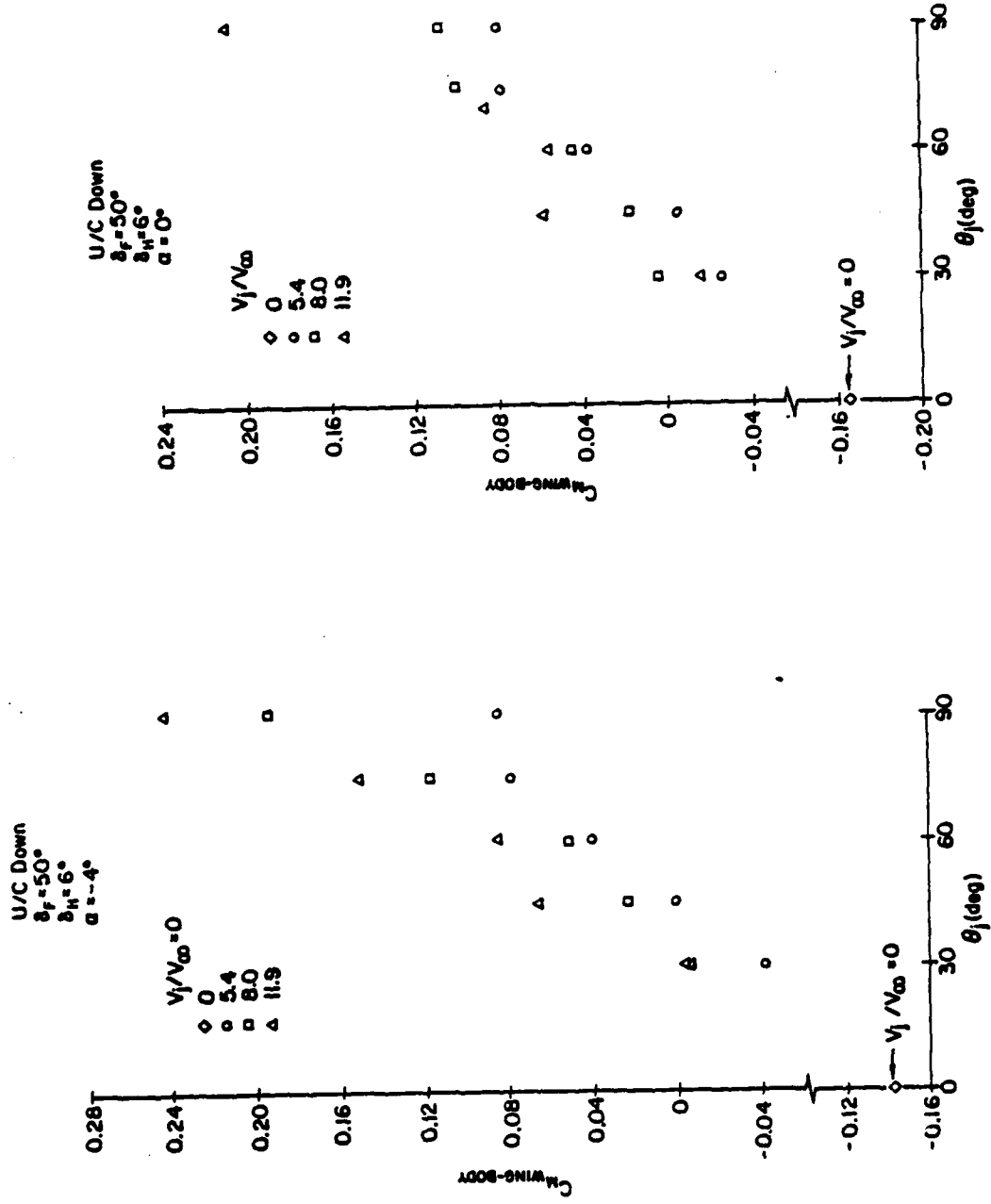
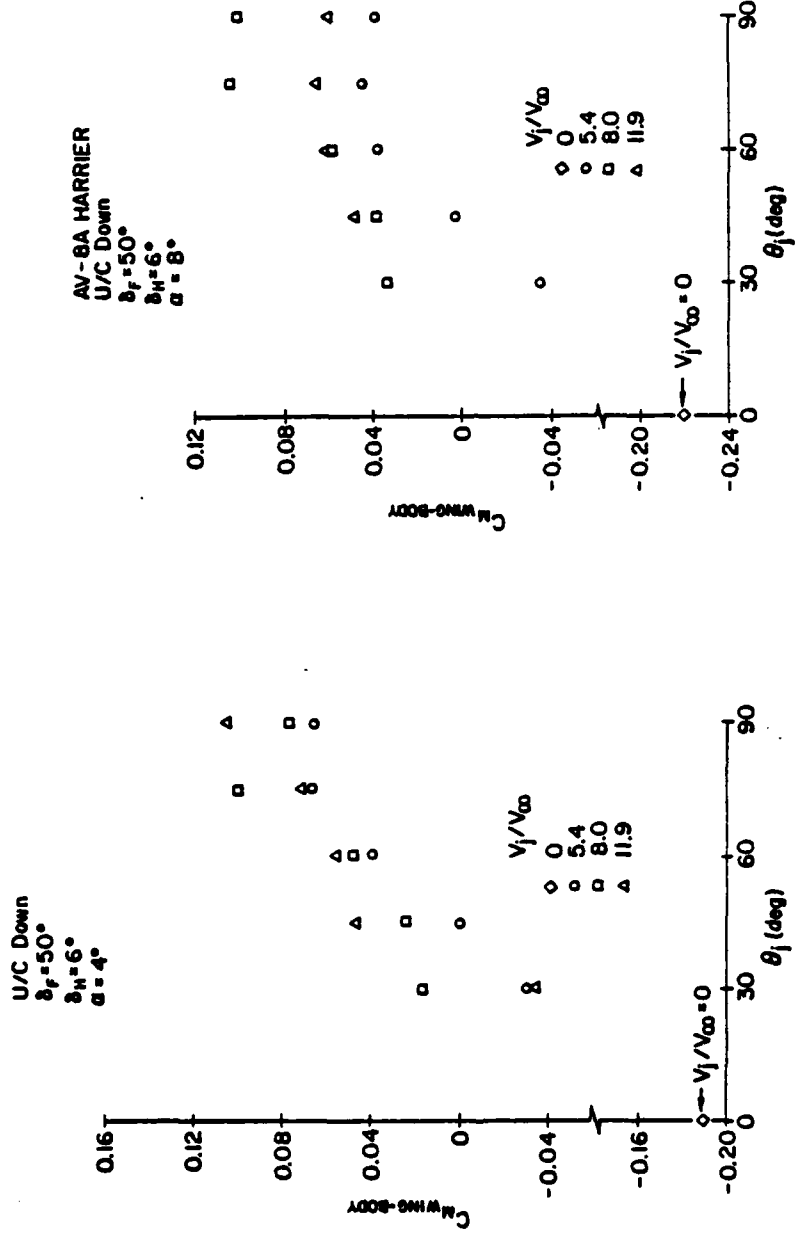


FIGURE 27 - AV-8A C_m wing-body With Wing/Jet Interaction, $\alpha = -4^\circ$.

FIGURE 28 - AV-8A C_m wing-body With Wing/Jet Interaction, $\alpha = 0^\circ$.



50

FIGURE 29 - AV-8A C_m wing-body With Wing/Jet Interaction,
 $\alpha = 4^\circ$.

FIGURE 30 - AV-8A C_m wing-body With Wing/Jet Interaction,
 $\alpha = 8^\circ$.

FIGURE 30 - AV-8A C_m wing-body With Wing/Jet Interaction,
 $\alpha = 8^\circ$.

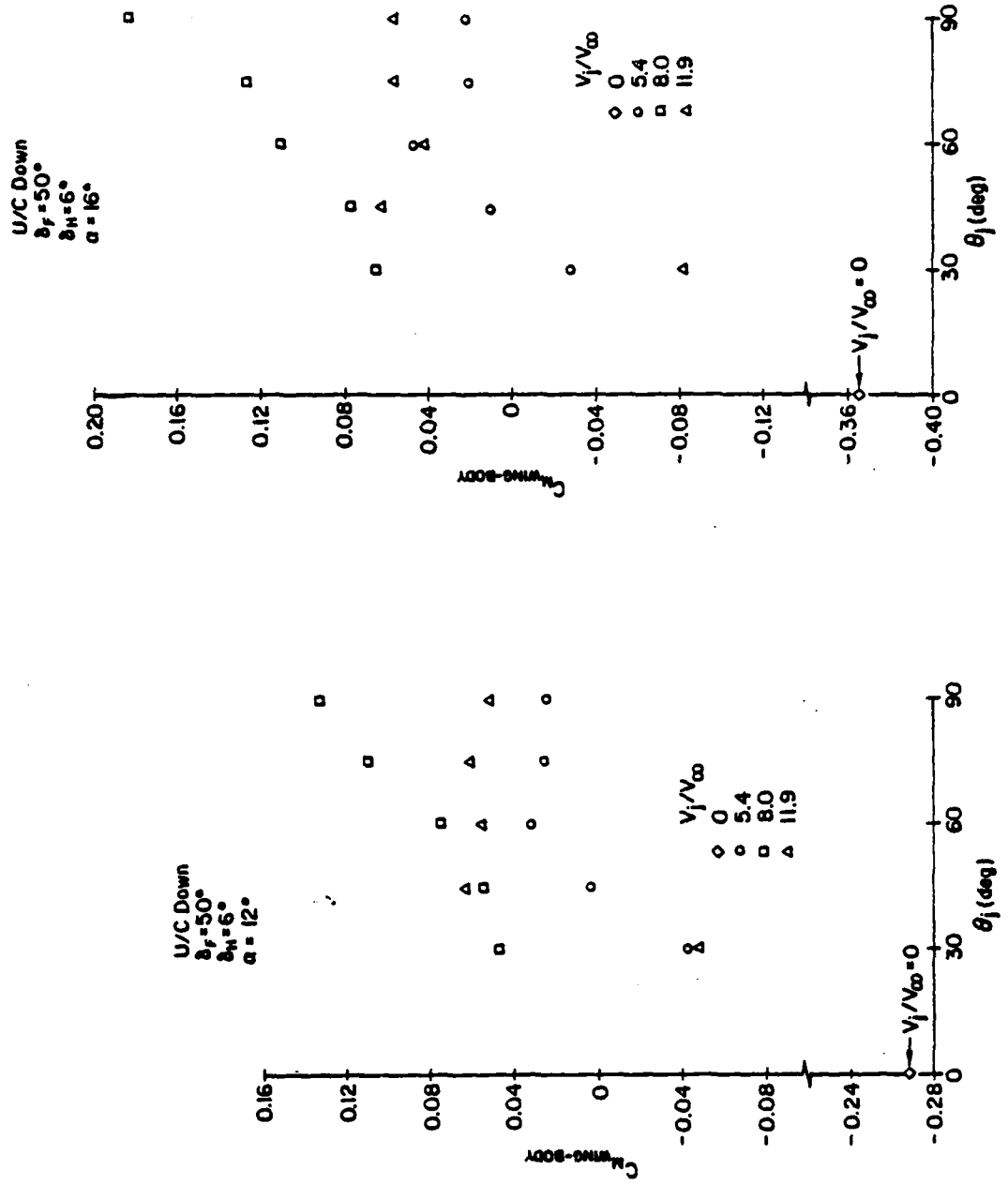


FIGURE 31 - AV-8A $C_m^{\text{wing-body}}$ With Wing/Jet Interaction,
 $\alpha = 12^\circ$.

FIGURE 32 - AV-8A $C_m^{\text{wing-body}}$ With Wing/Jet Interaction,

With Wing/Jet Interaction,
 $\alpha = 16^\circ$.

FIGURE 32 - AV-8A $C_m^{\text{wing-body}}$ With Wing/Jet Interaction,

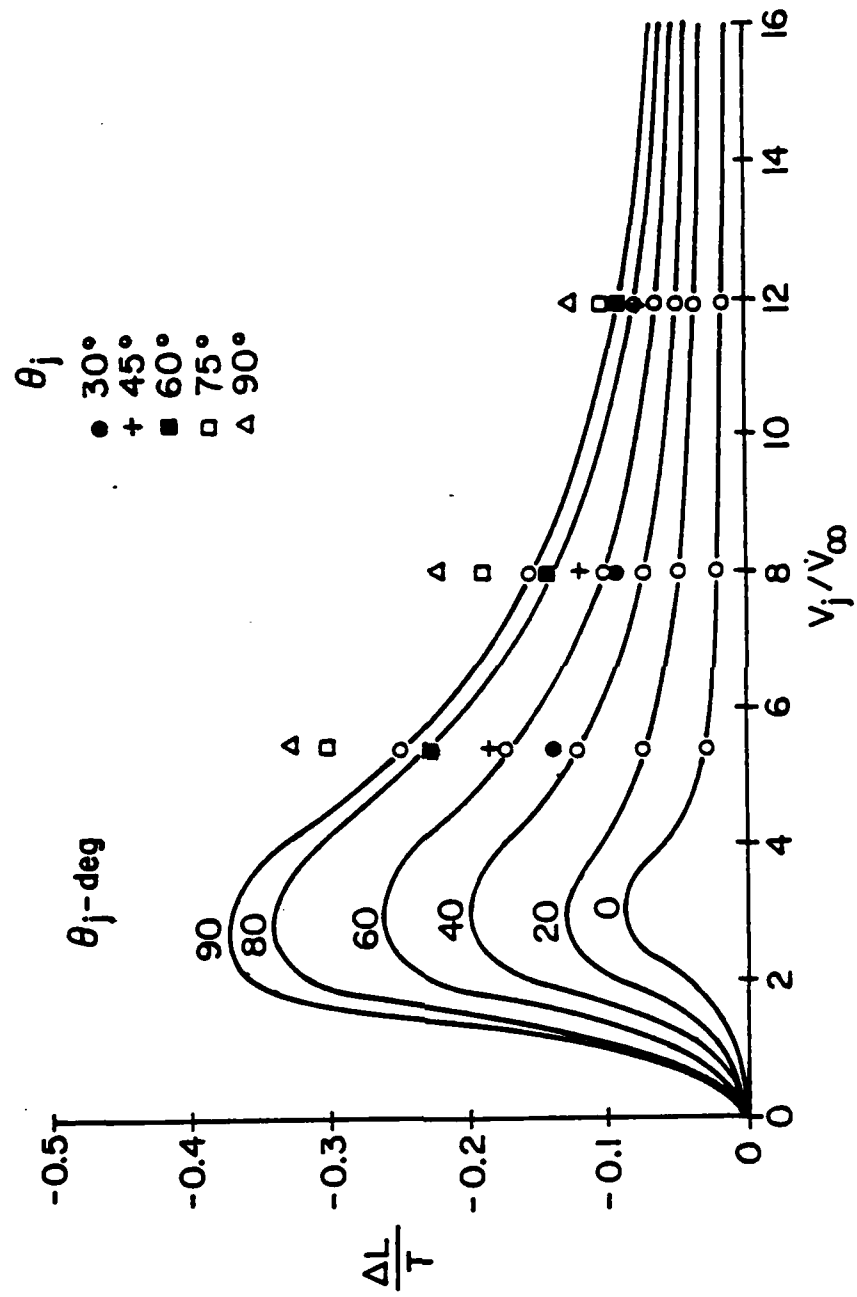


FIGURE 33 - AV-8A Non-dimensionalized lift loss as a function of θ_j and V_j / V_∞
 (Ref. 5, Data from pp. 161-175 and p. 191 compared).

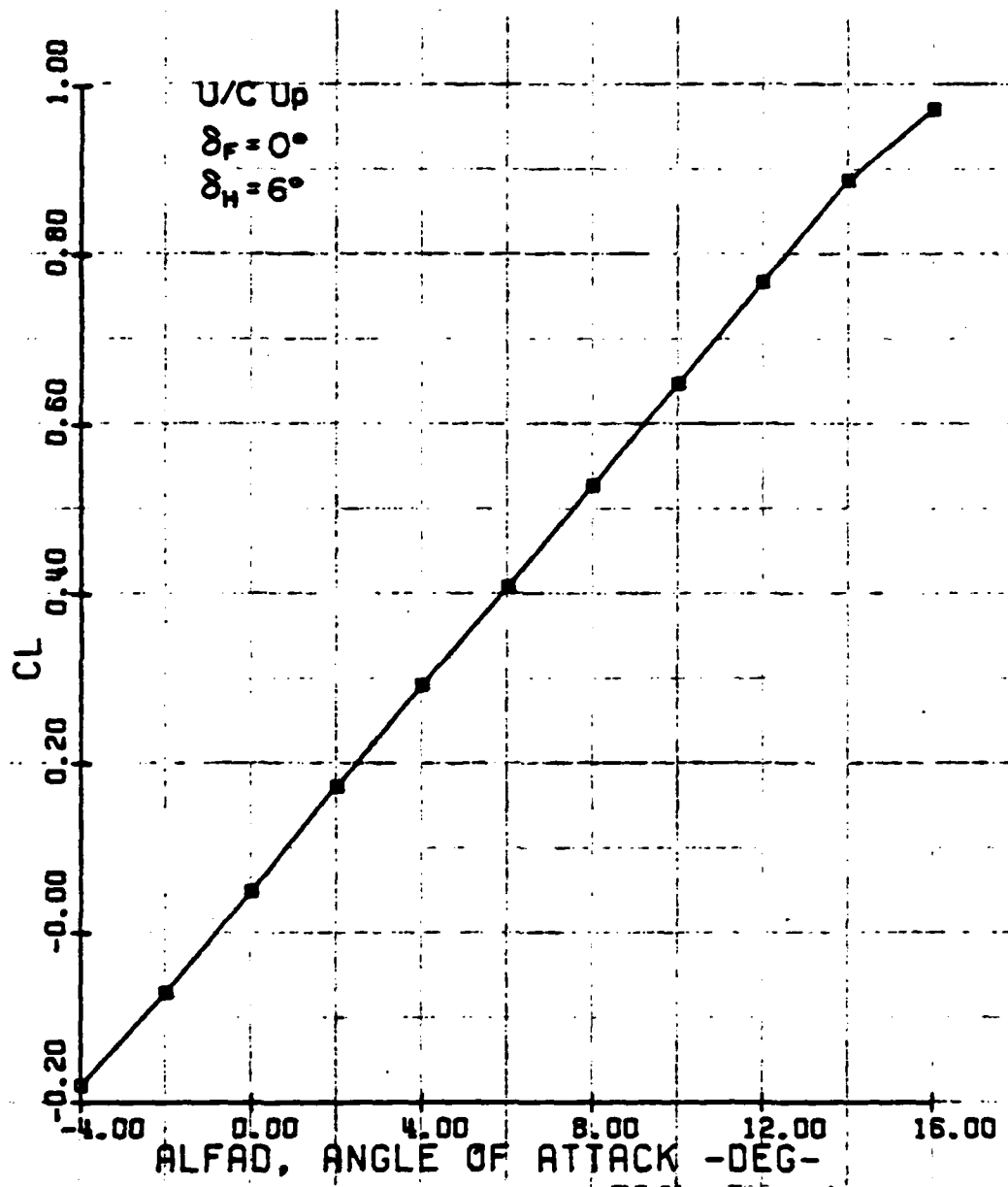


FIGURE 34 - C_L _{wing-body} Flaps Up, Without Wing/Jet Interaction
 (Ref. 5, p. 160).

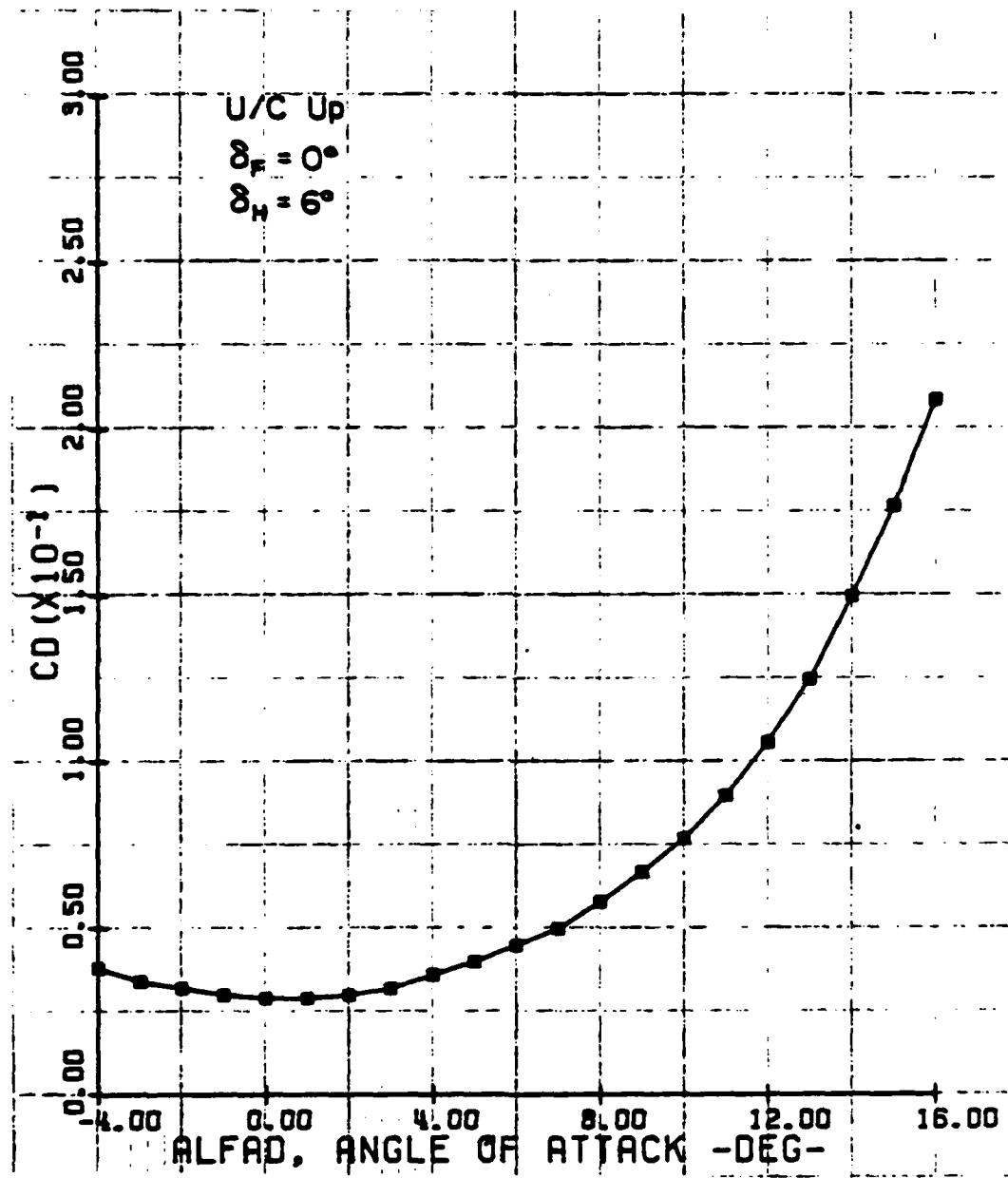


FIGURE 35 - C_D _{wing-body} Flaps Up, Without Wing/Jet Interaction
(Ref. 5, p. 160).

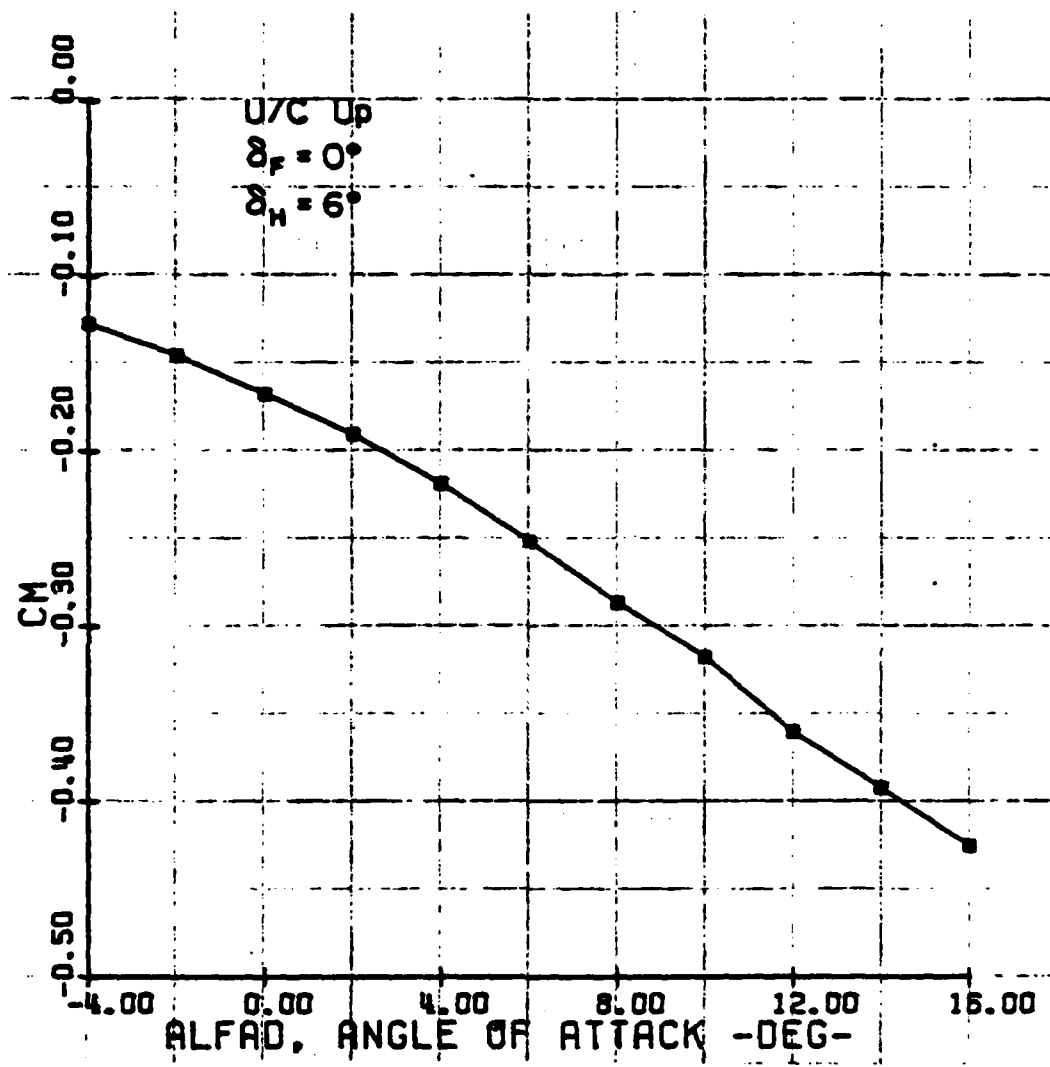


FIGURE 36 - $C_{M,30}$ Flaps Up, Without Wing/Jet Interaction
 (Ref. 5, p. 160).

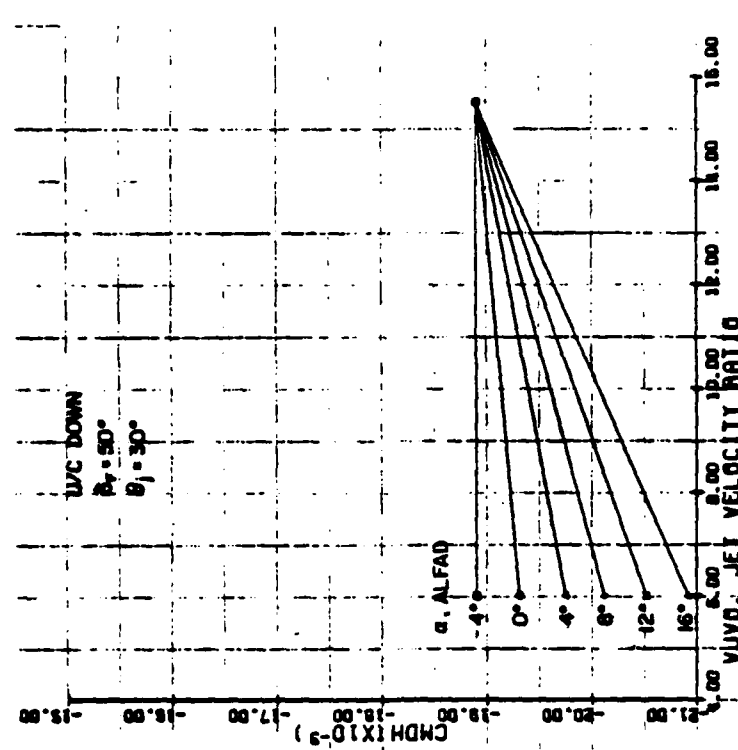
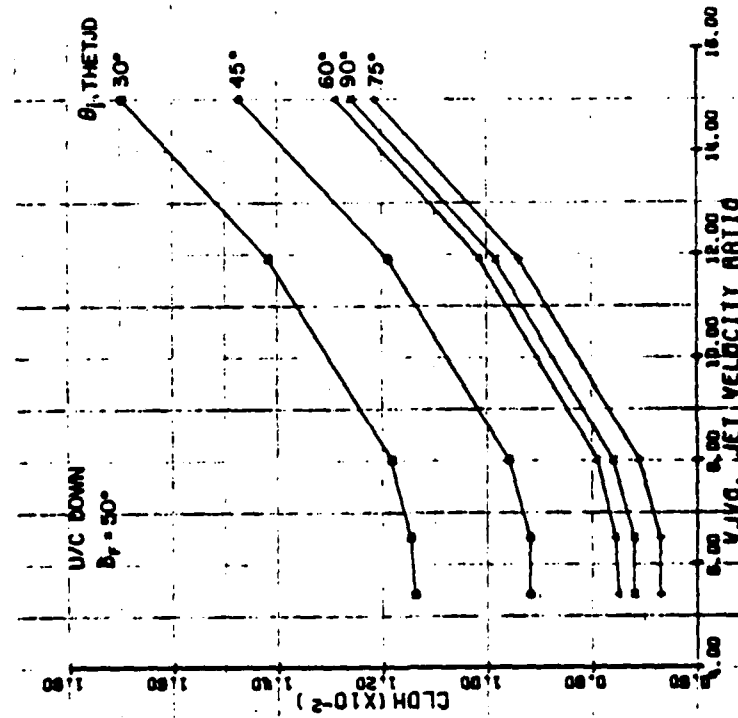


FIGURE 37 - $C_{L_{\delta H}}$ With Wing/Jet Interaction for Various θ_j , FIGURE 38 - $C_{m_{\delta H}}$ With Wing/Jet Interaction (No Reaction All Angles of Attack (No Reaction Control Thrusters), $\theta_j = 30^\circ$.

FIGURE 38 - $C_{m_{\delta H}}$ With Wing/Jet Interaction (No Reaction All Angles of Attack (No Reaction Control Thrusters), $\theta_j = 30^\circ$.

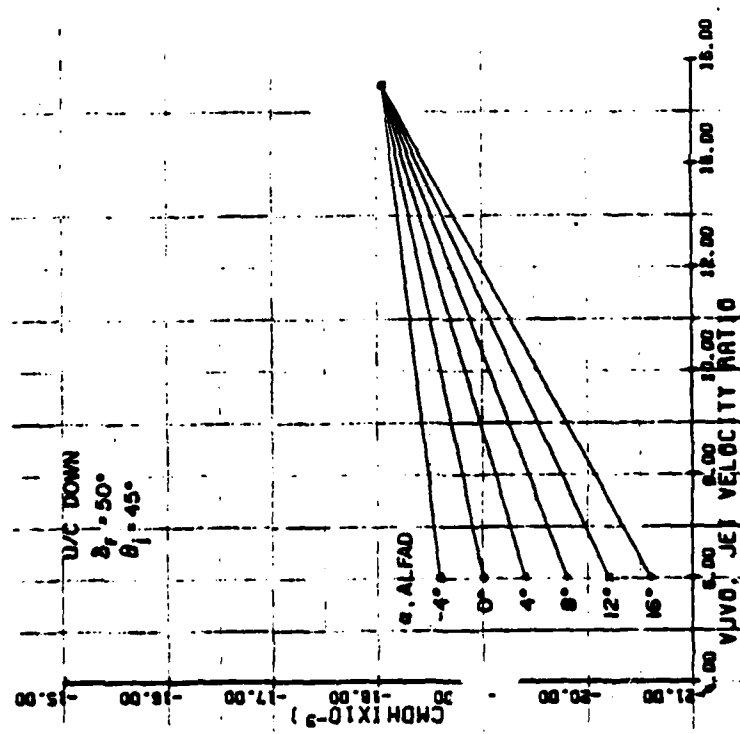


FIGURE 39 - $C_{m\delta H}$ With Wing/Jet Interaction (No Reaction Control Thrusters), $\theta_j = 45^\circ$.

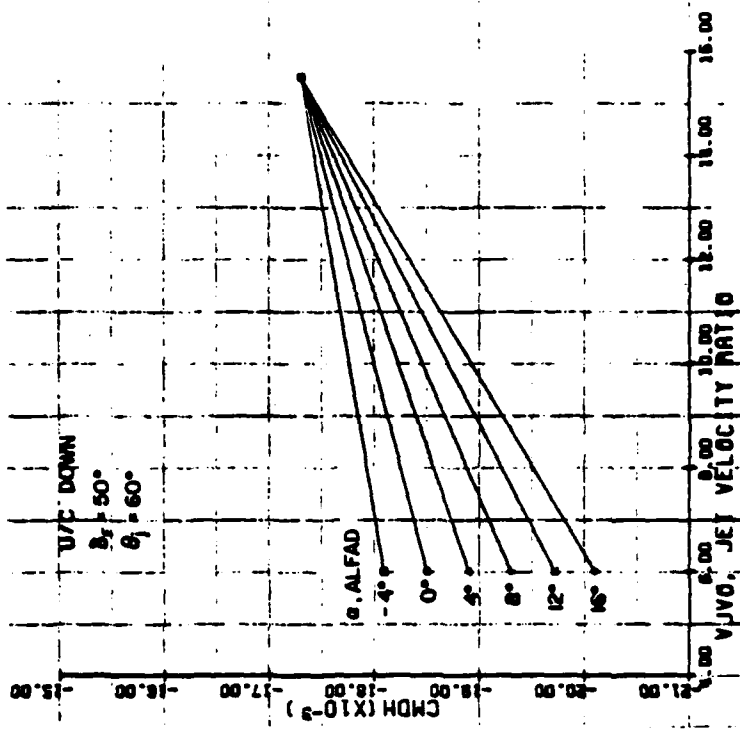


FIGURE 40 - $C_m \delta H$ With Wing/Jet Interaction (No Reaction Control Thrusters), $\theta_j = 60^\circ$

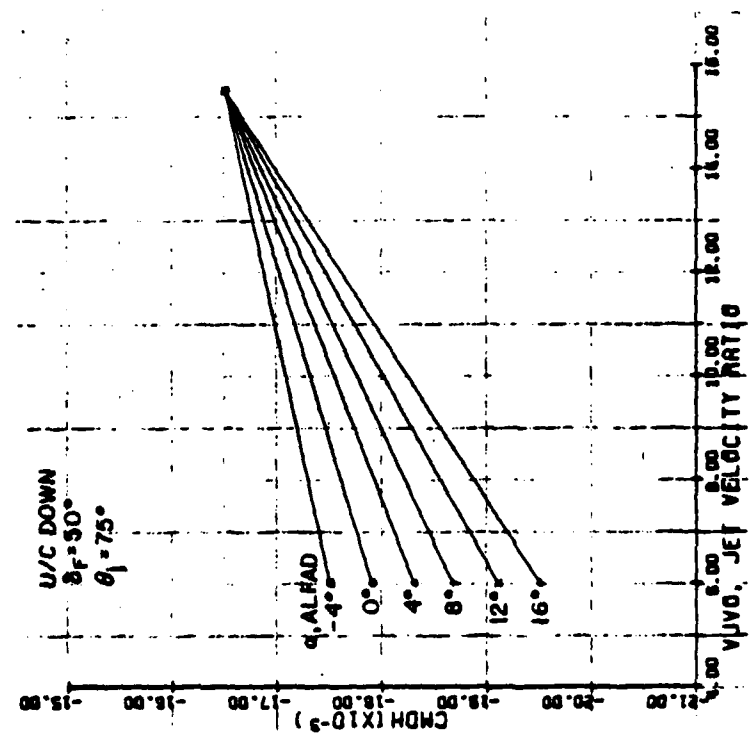


FIGURE 41 - C_m^H With Wing/Jet Interaction (No Reaction
Control Thrusters), $\theta_j = 75^\circ$

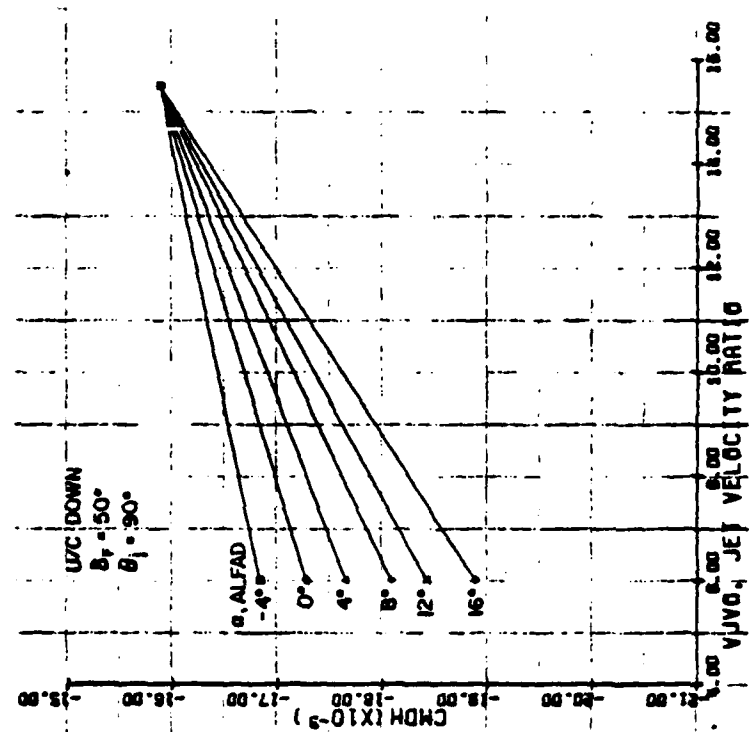


FIGURE 42 - C_m^H With Wing/Jet Interaction (No Reaction
Control Thrusters), $\theta_j = 90^\circ$.

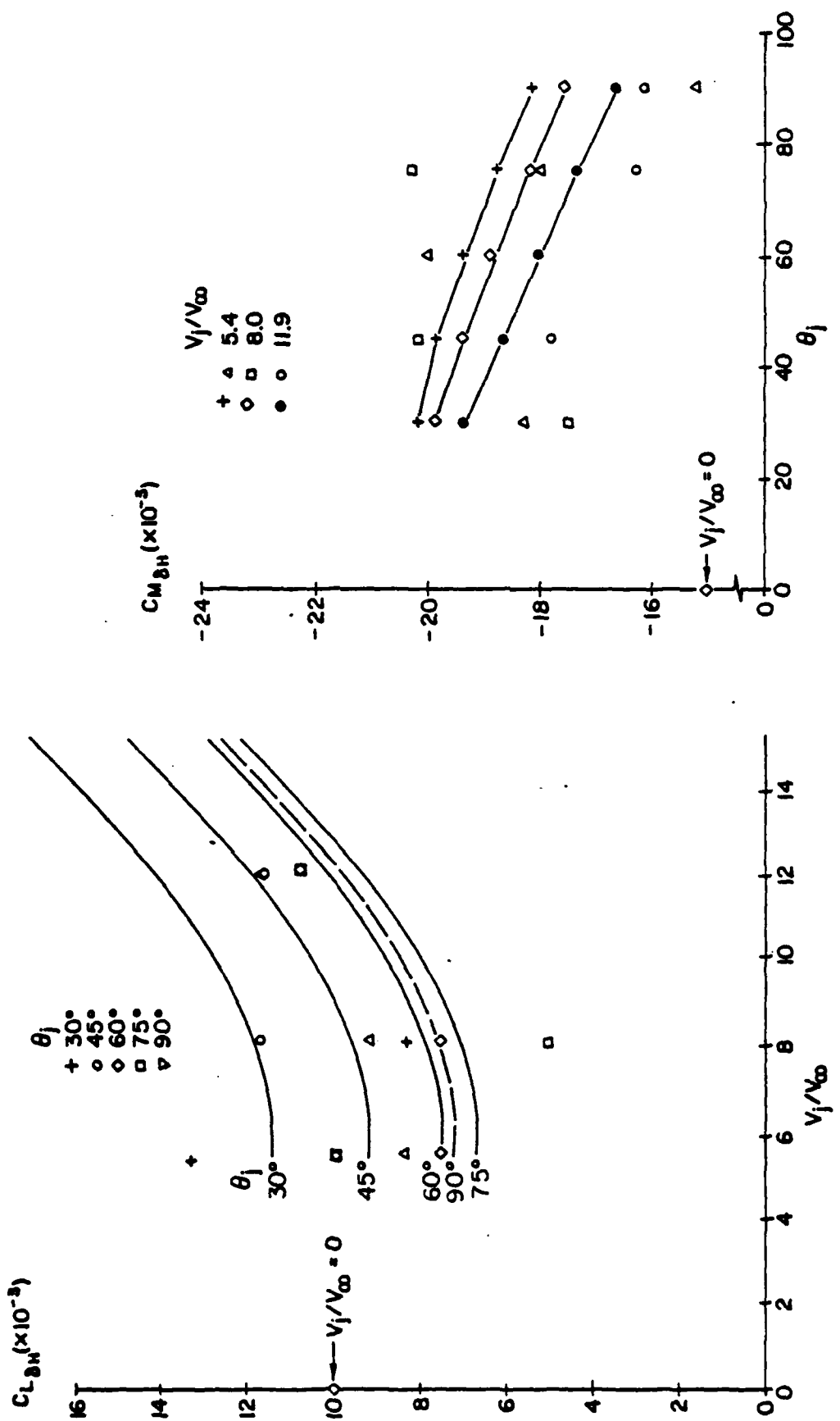


FIGURE 43 - Comparison of $C_{L,\delta H}$ Data.

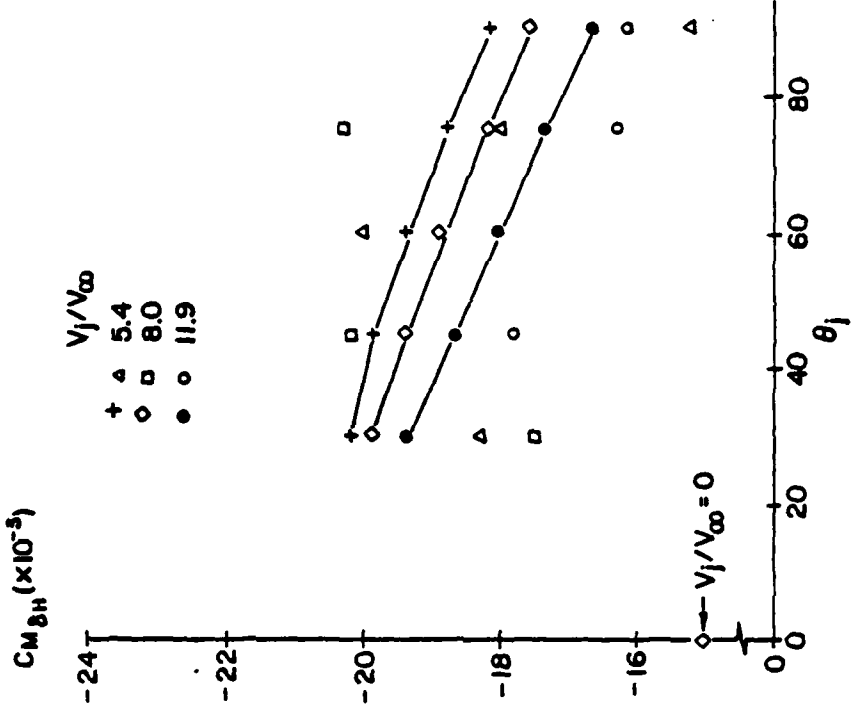


FIGURE 44 - Comparison of $C_{M,\delta H}$ Data.

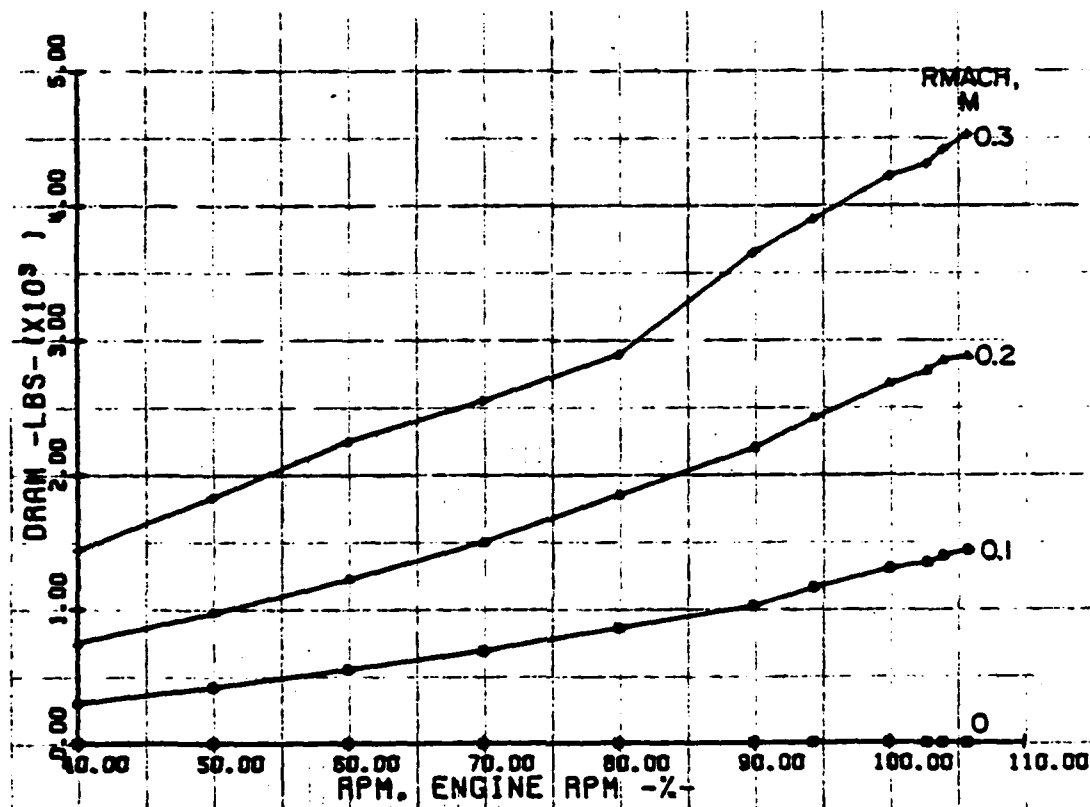
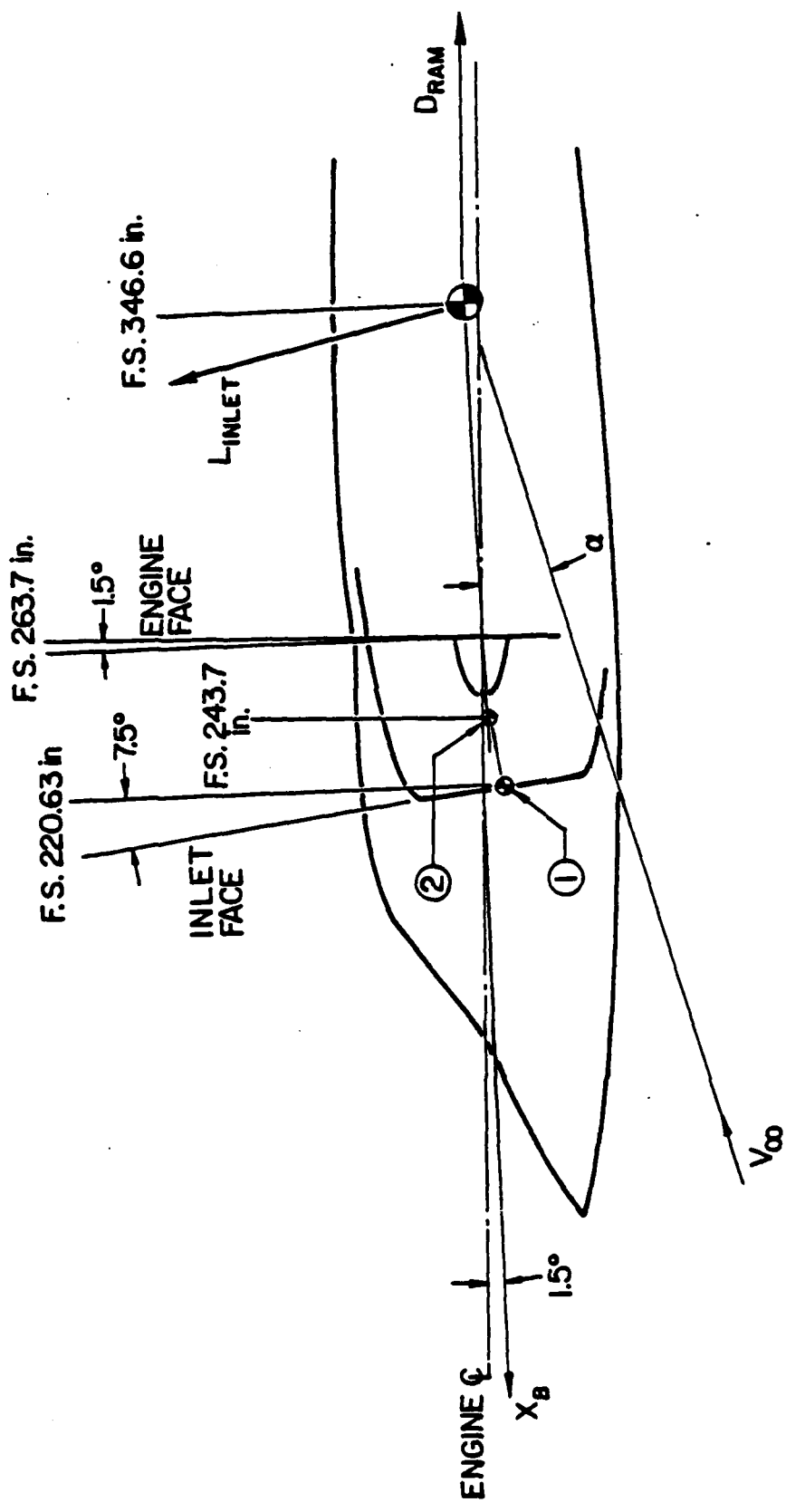


FIGURE 45 - Ram Drag at Various Mach Numbers.



$$\Delta C_{M, \text{INLET}} = f(\Delta m_v \text{ AT THE INLET FACE} + \Delta m_v \text{ INTERNAL})$$

$$\Delta C_{M, \text{INLET}} = (D_{\text{RAM}} / q S \bar{c}) 10.41 (\sin(\alpha - 7.5^\circ)) + 8.10 \sin 9^\circ$$

NOTE: \bar{c} IN FEET

FIGURE 46 - Modelling $\Delta C_{M, \text{INLET}}$ Due to Ram Drag (Ref. 5).

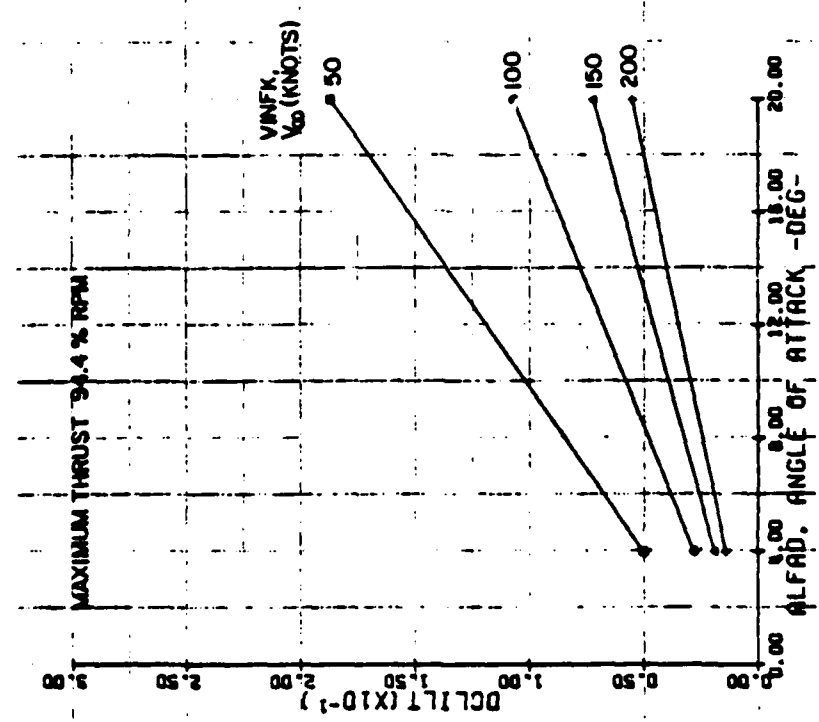


FIGURE 47 - Change in Lift Coefficient Due to Ram Drag ($\Delta C_{L_{inlet}}$) for Various V_{∞} , RPM = 94.4%.

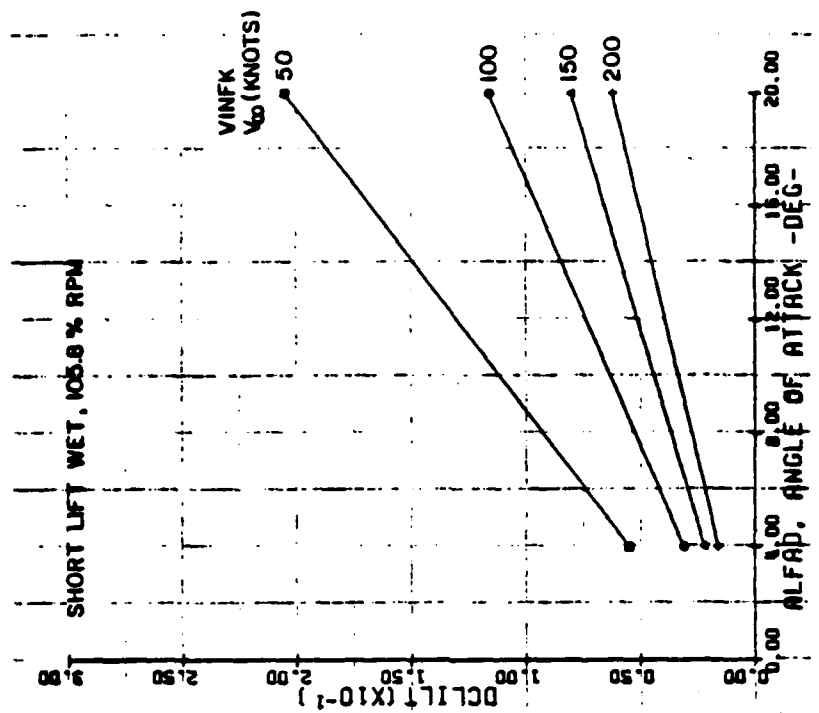


FIGURE 48 - Change in Lift Coefficient Due to Ram Drag ($\Delta C_{L_{inlet}}$) for Various V_{∞} , RPM = 105.8%.

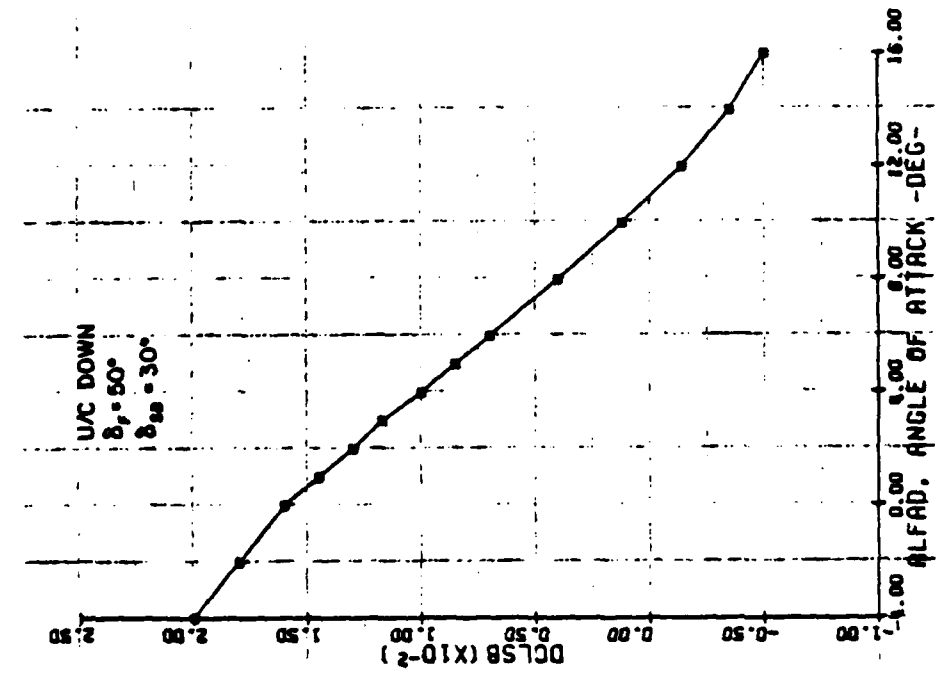


FIGURE 49 - Change in Lift Coefficient Due to Speedbrake Deflection ($\Delta C_{L_{sb}}$) for $\delta_{speedbrake} = 30^\circ$.

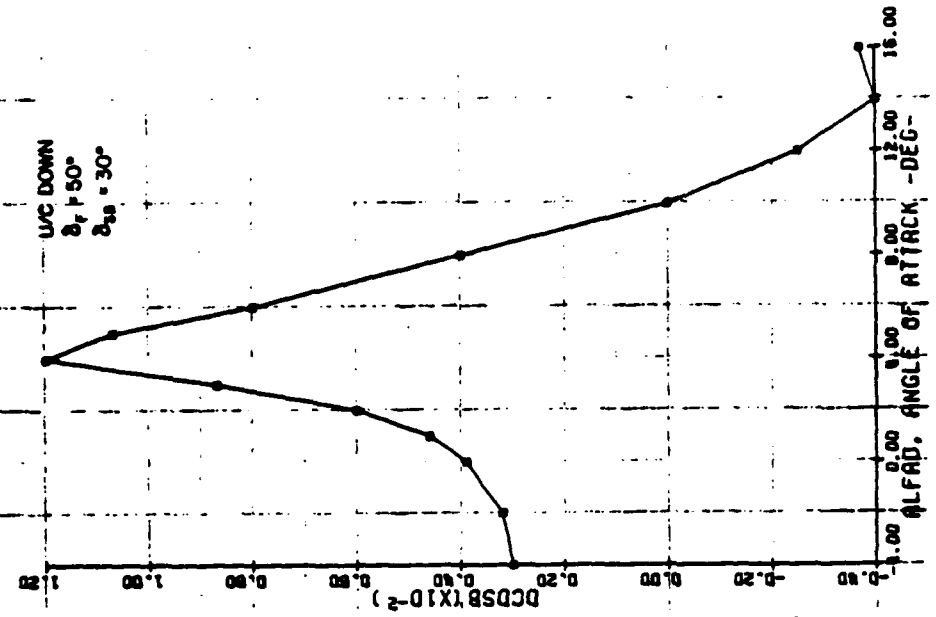


FIGURE 50 - Change in Drag Coefficient Due to Speedbrake Deflection (ΔC_D) for $\delta_{speedbrake} = 30^\circ$.

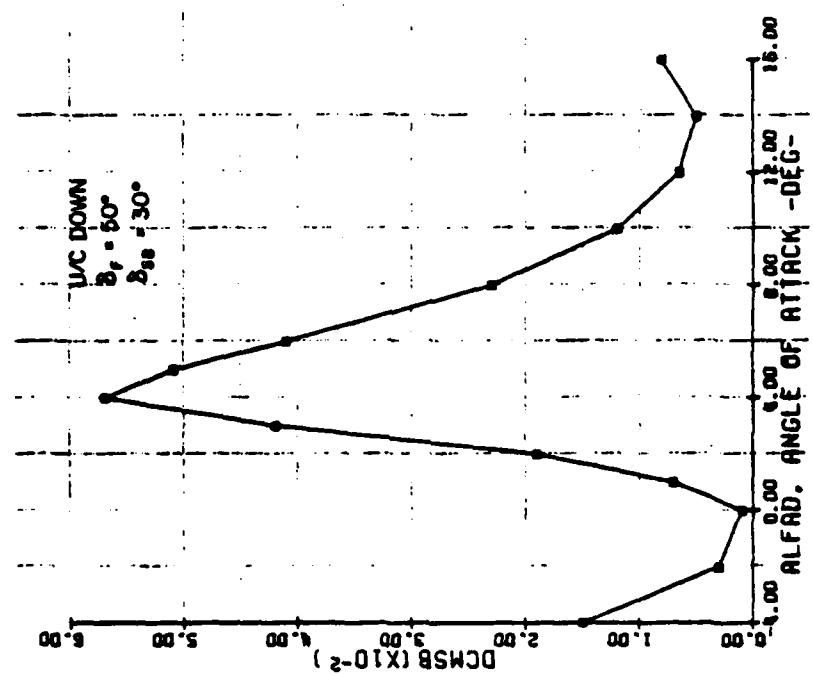
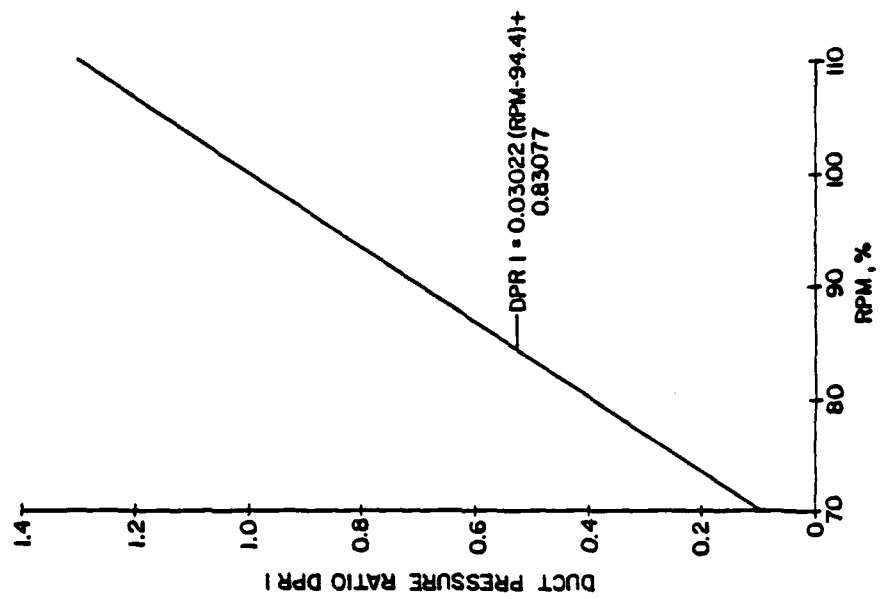


FIGURE 51 - Change in Pitching Moment Coefficient Due to Speedbrake Deflection (ΔC_m)
to Speedbrake Deflection (ΔC_m)
for δ_m speedbrake = 30° .

FIGURE 52 - Reaction Control System Duct Pressure Ratio as a Function of Engine RPM.

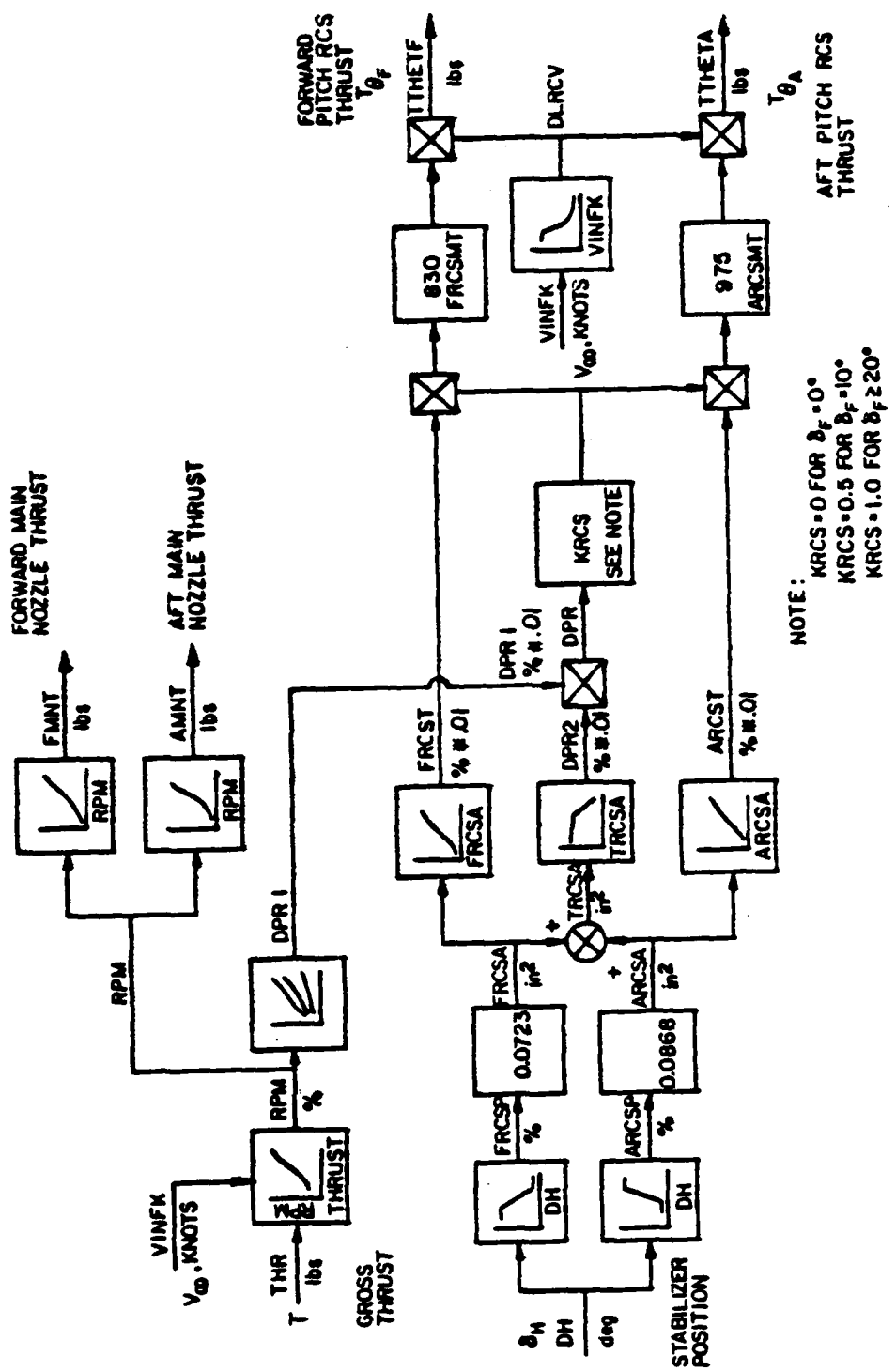


FIGURE 53 - Functional Block Diagram of the AV-8A Reaction Control System and Engine.

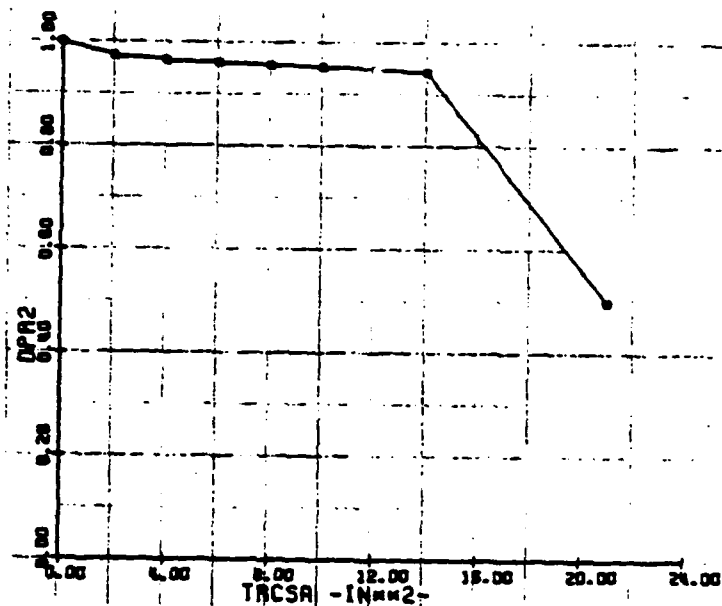


FIGURE 54 - Reaction Control System Duct Pressure Ratio as a Function of Total RCS Nozzle Area Opening.

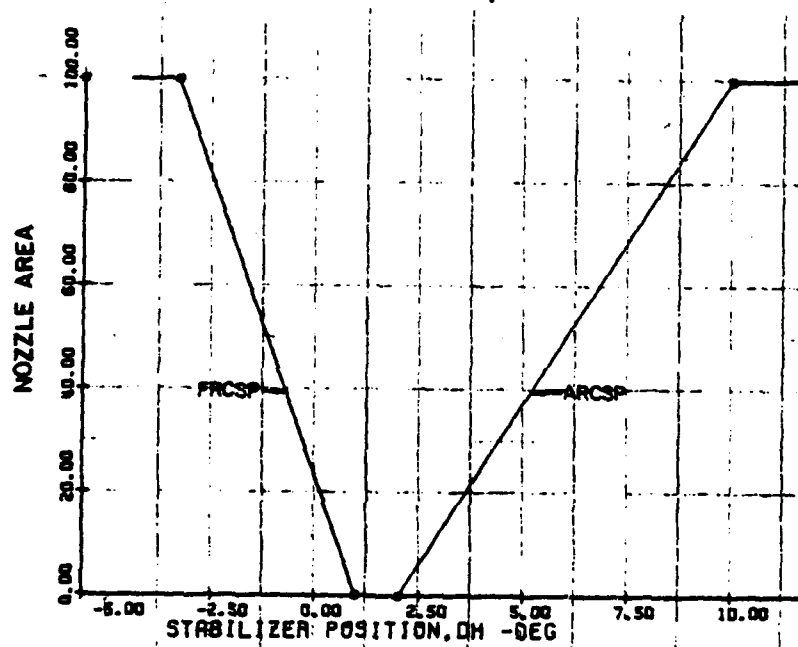


FIGURE 55 - RCS Nozzle Opening as a Function of Stabilizer Position.

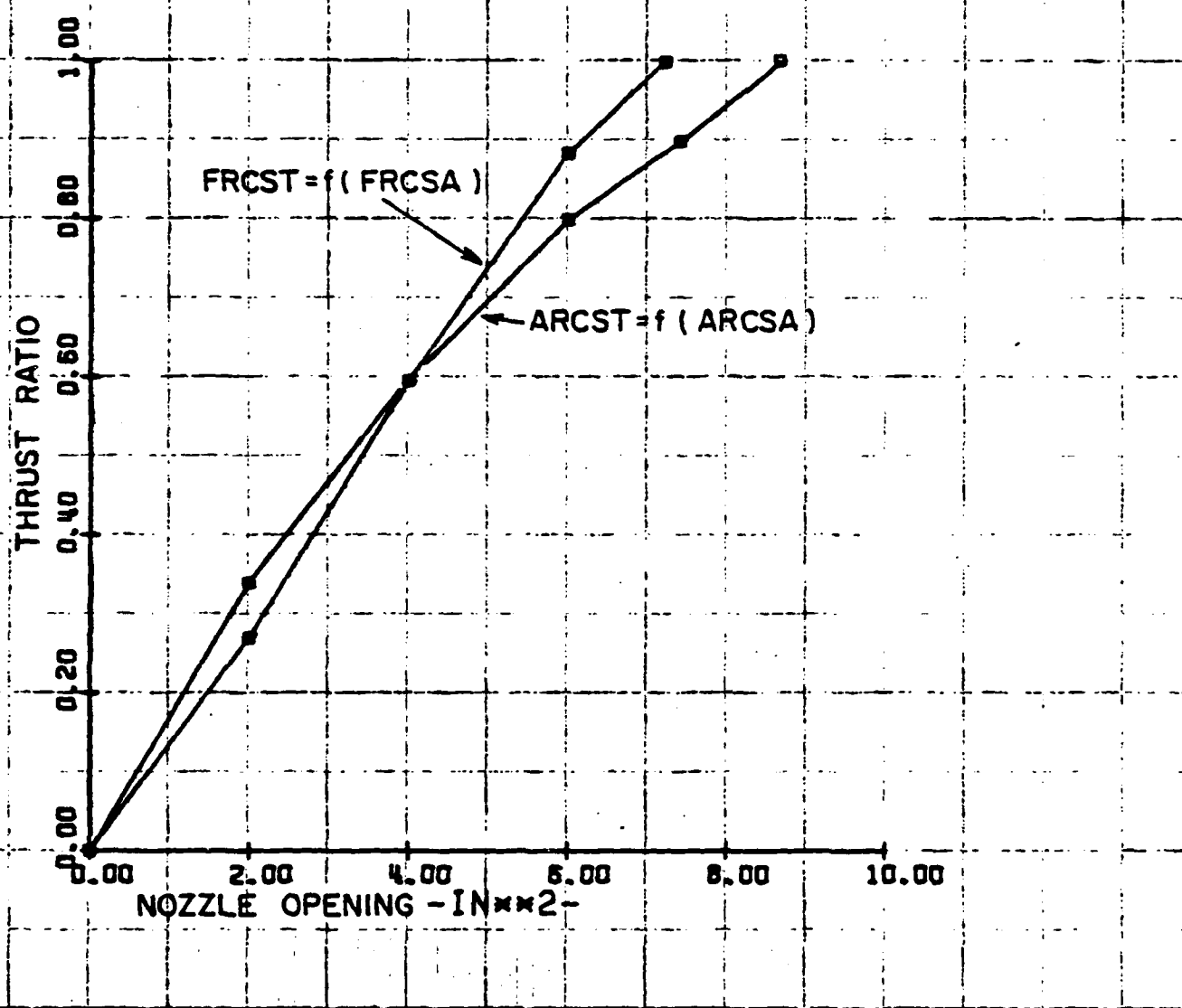


FIGURE 56 - Forward and Aft RCS Thrust Ratios as Functions of Their Respective Nozzle Openings.

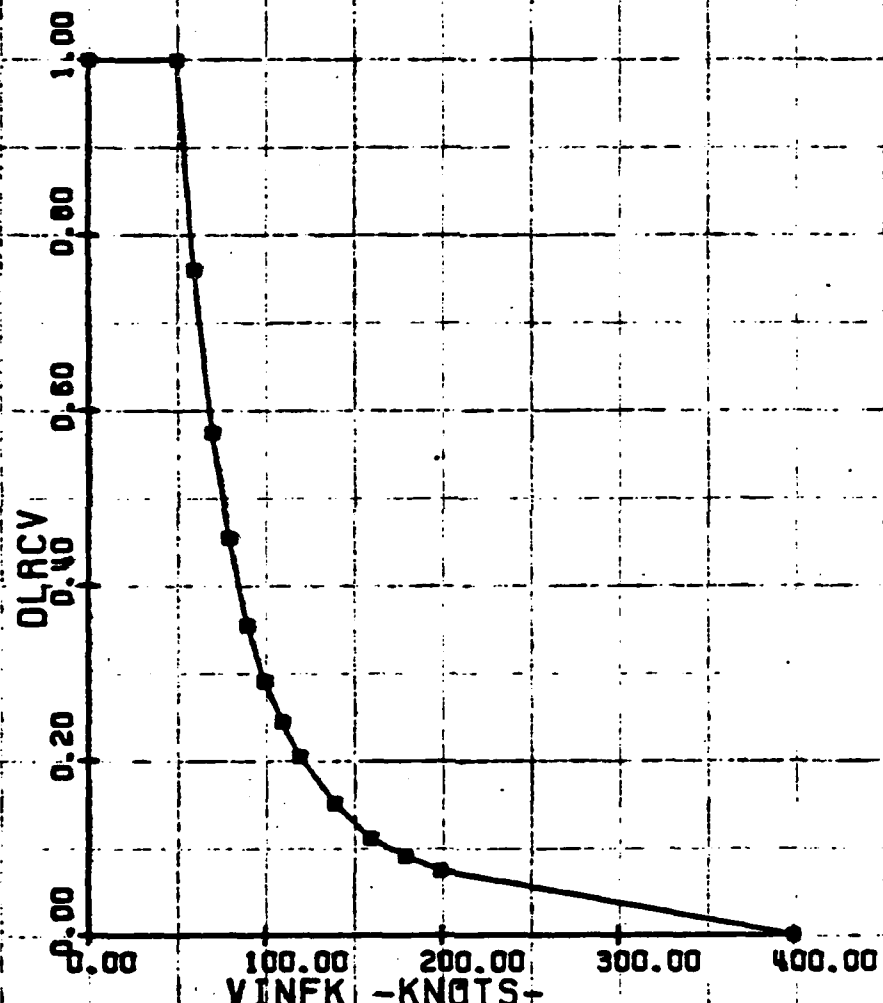


FIGURE 57 - RCS Effectiveness as a Function of Freestream Velocity.

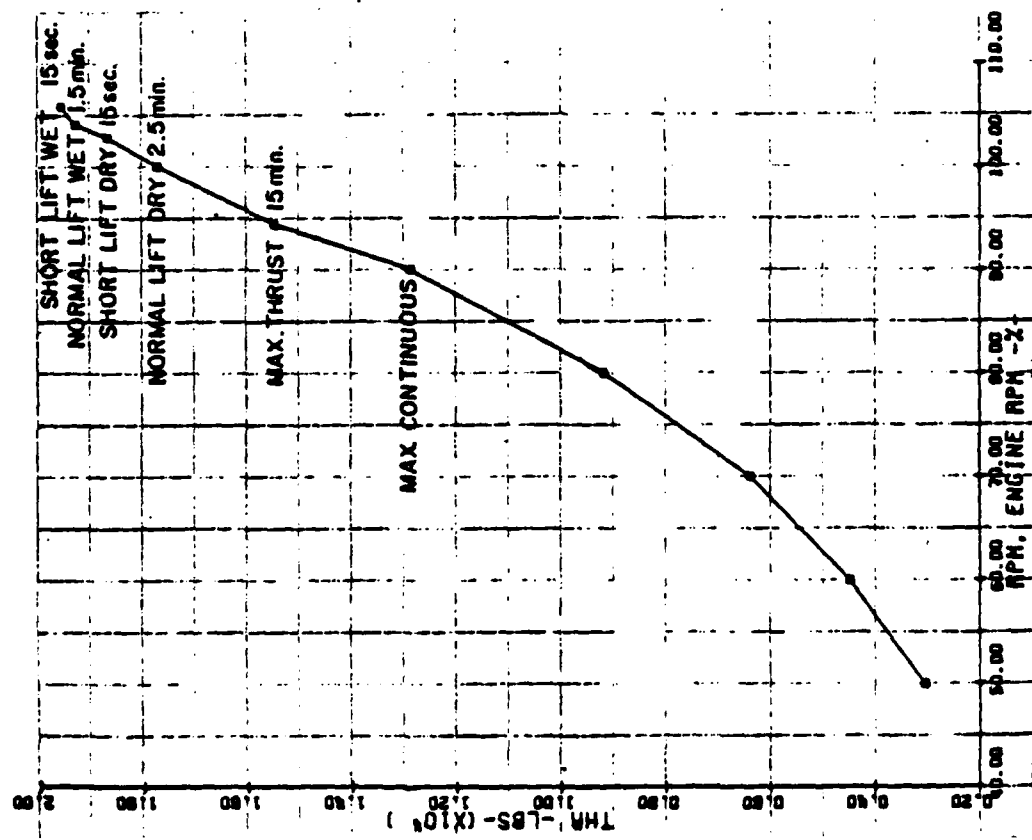


FIGURE 58 - Gross Thrust as a Function of Engine RPM.

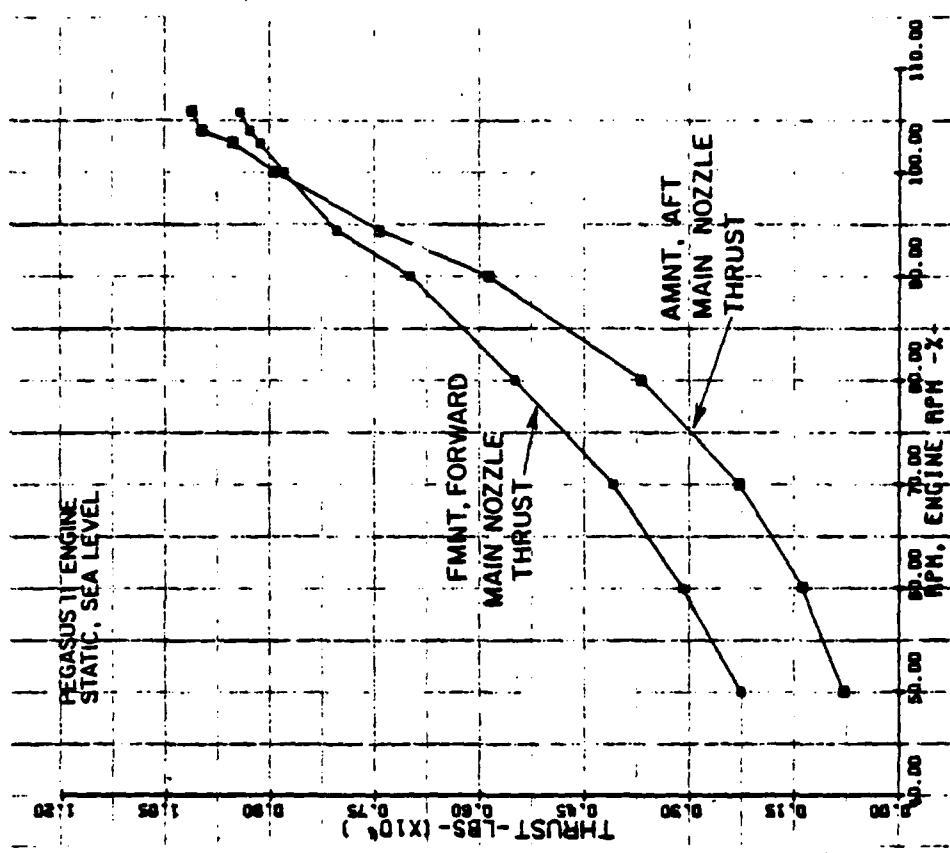


FIGURE 59 - Main Nozzle Thrust Distribution as a Function of Engine RPM.

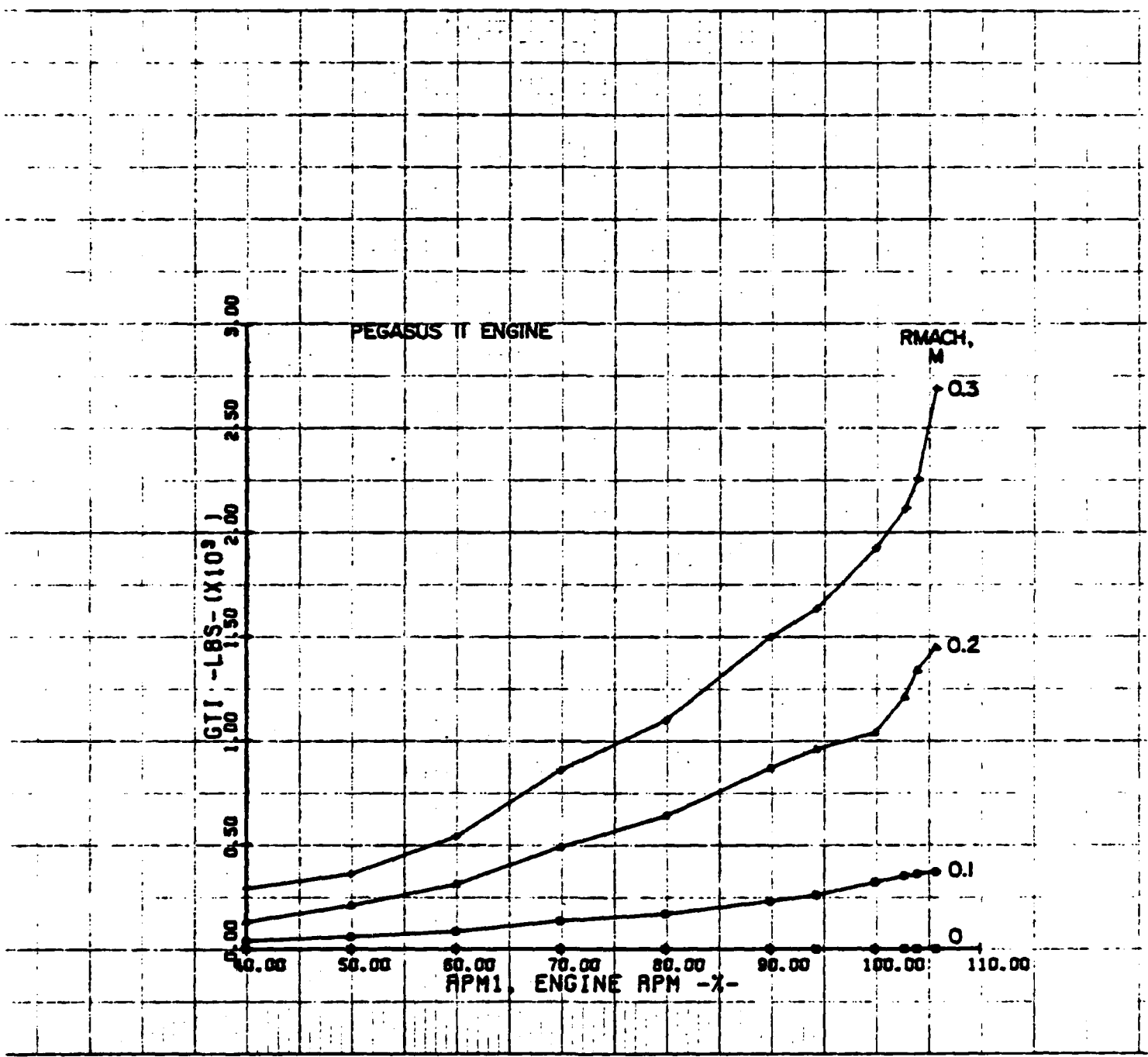


FIGURE 60 - Gross Thrust Increase Due to Freestream Velocity.

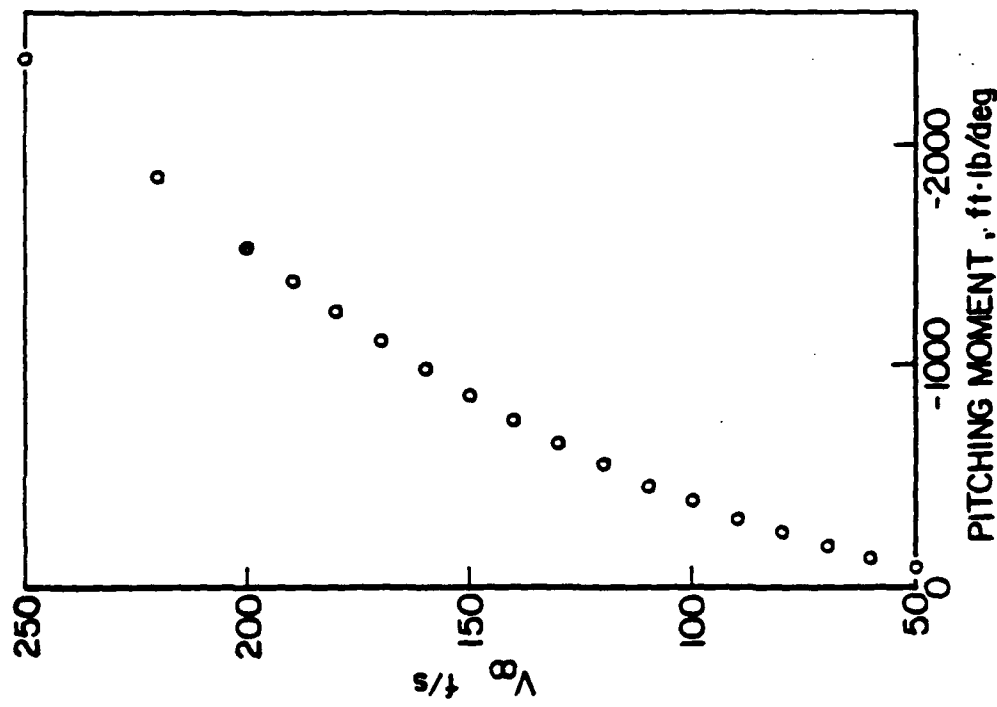


FIGURE 61 - Pitching Moment per Degree of Stabilizer Deflection.

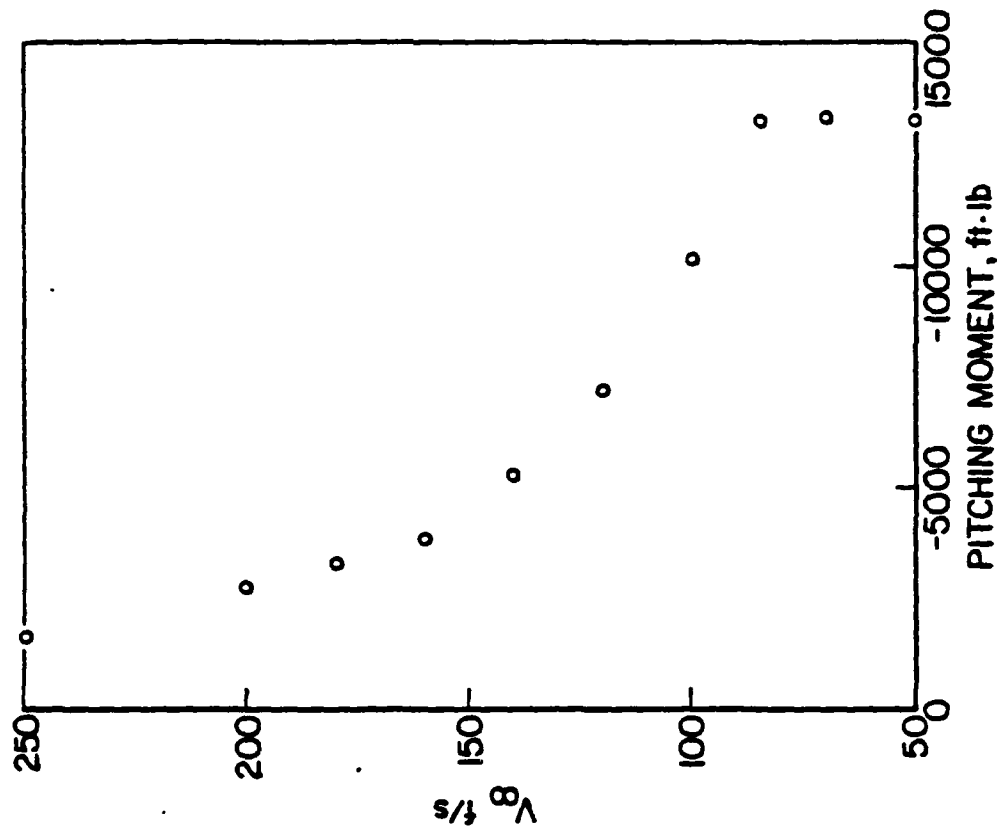


FIGURE 62 - Maximum Nose Down RCS Control Pitching Moment.

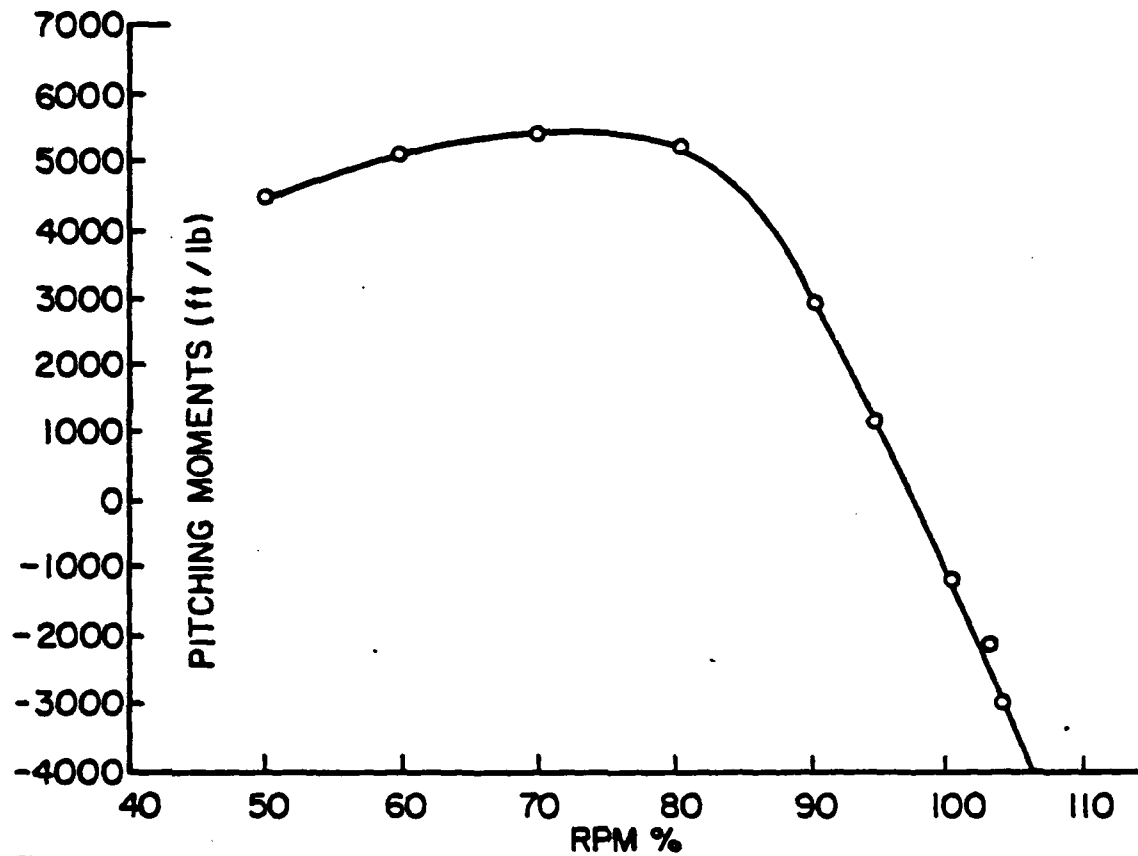


FIGURE 63 - Variation of Pitching Moment with Gross Thrust at $\theta_j = 90^\circ$.

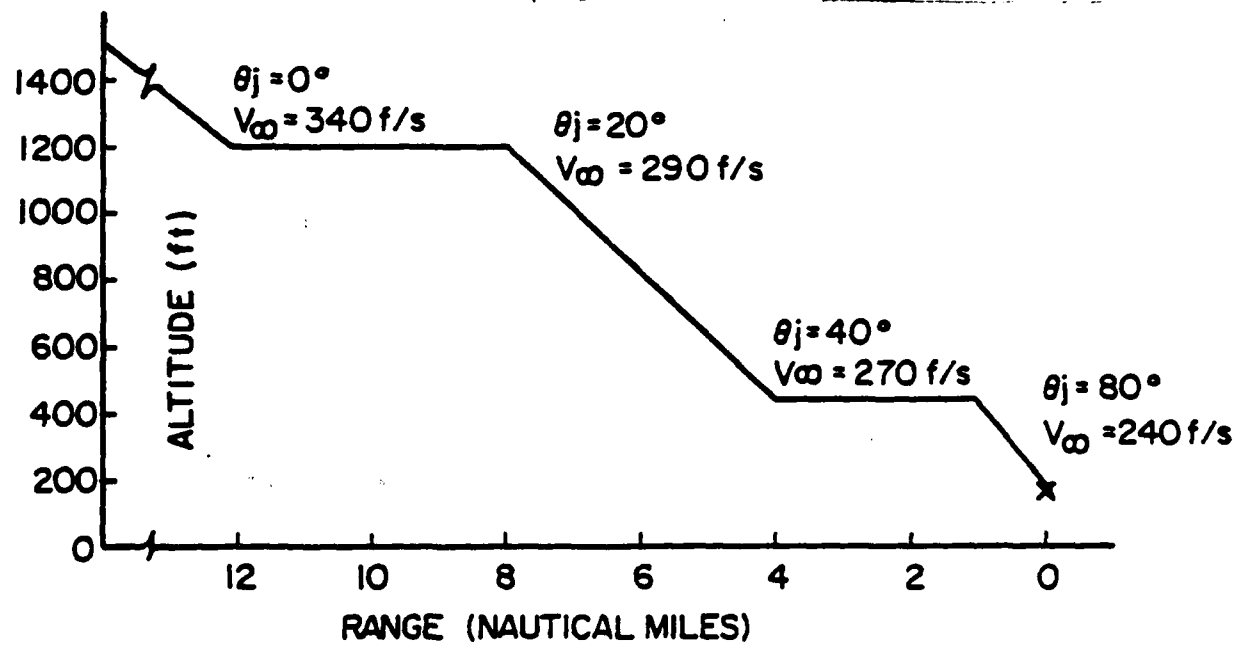


FIGURE 64 - Shipboard Approach Profile as Used by the United States Marine Corps.

(PT/SEC) 52:HAFRIER;V=0-300; THETJ=0-98.5; PLAP=50.0; APAR= 0.1; GAM= 0.1

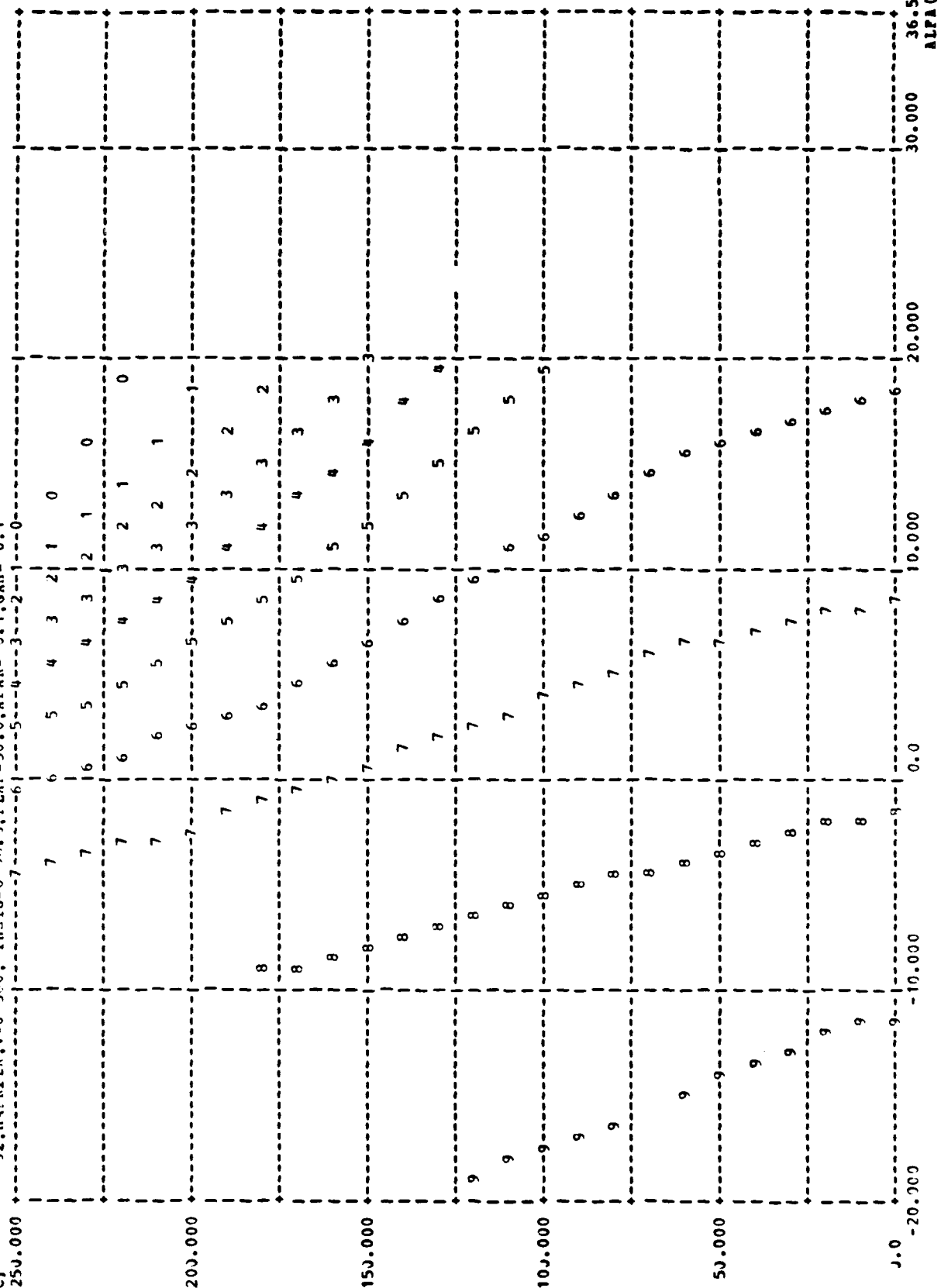


FIGURE 65 - Trimmap of $\alpha(\theta_j, V_\infty)$; with $\delta_F = 50^\circ$, $U_{V_\infty} = 0.1 g$, $\gamma_c = 0.1$ rad.

52:HARRIER; V=0-300; THEIJ=C-98.5; FLAP=50.0; APAR= 0.1; GAM= 0.1

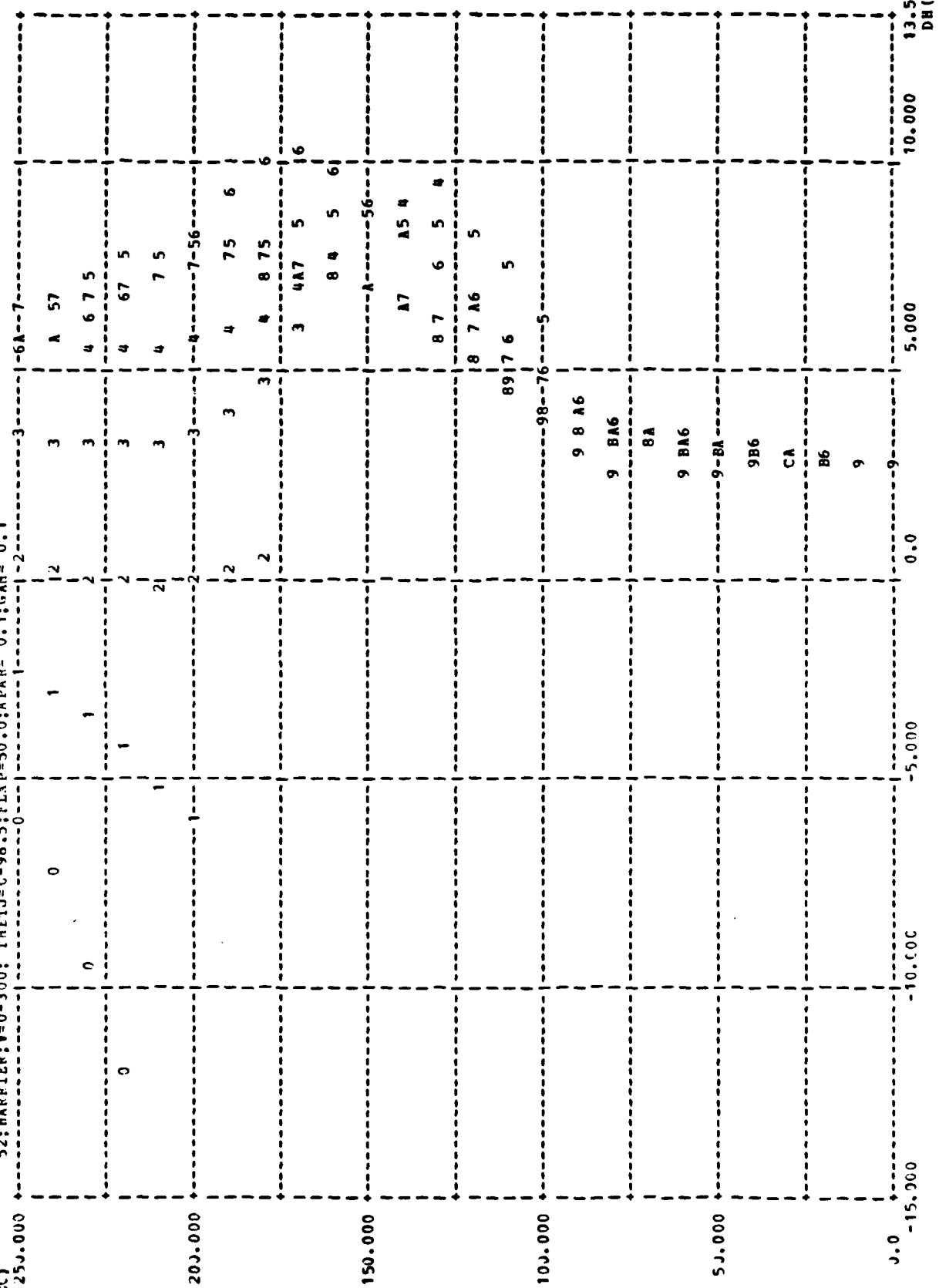


FIGURE 66 - Tr-1 map of $\delta_H(\theta_j, V_\infty)$; with $\delta_F = 50^\circ$, $u_{V_c} = 0.1 g$, $\gamma_c = 0.1$ rad.

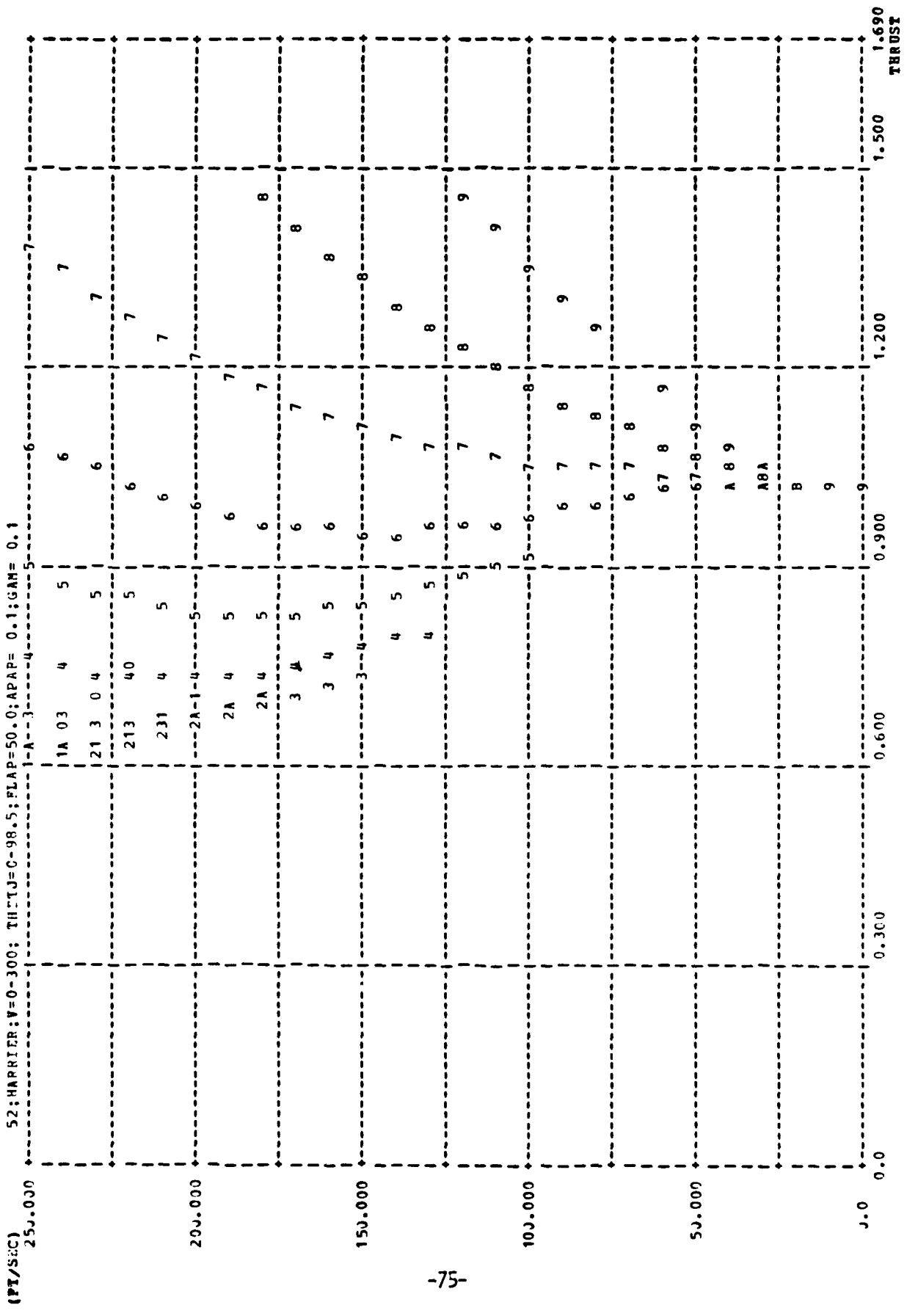


FIGURE 67 - Trimmap of $T/W(\theta_j, V_\infty)$; with $\delta_F = 50^\circ$, $\delta_{V_C} = 0.19$, $\gamma_C = 0.1$ rad.

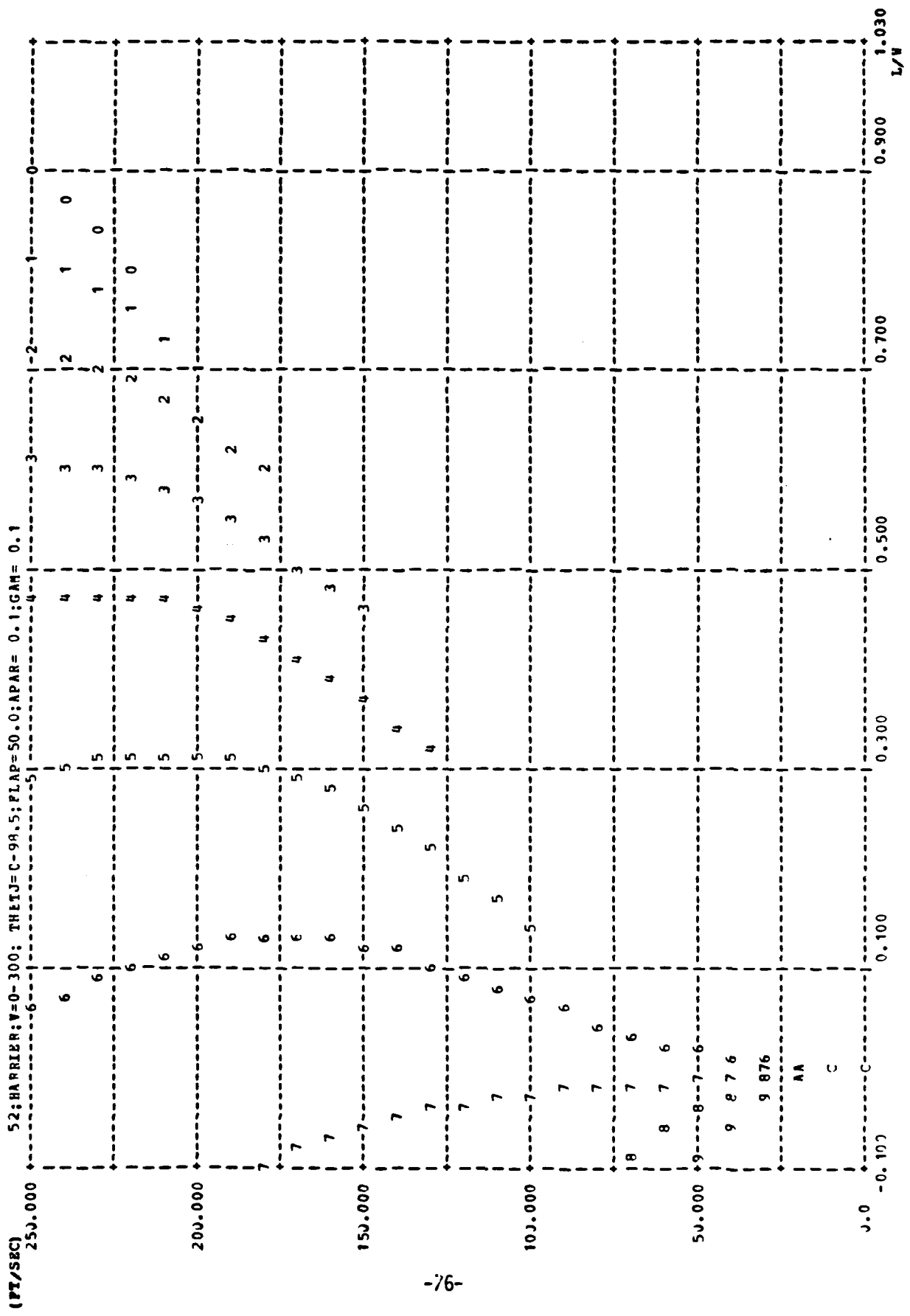


FIGURE 68 - Trimmap of $L/M(\theta_j, V_\infty)$; with $\delta_F = 50^\circ$, $\dot{u}_{V_c} = 0.1$ g, $\gamma_c = 0.1$ rad.

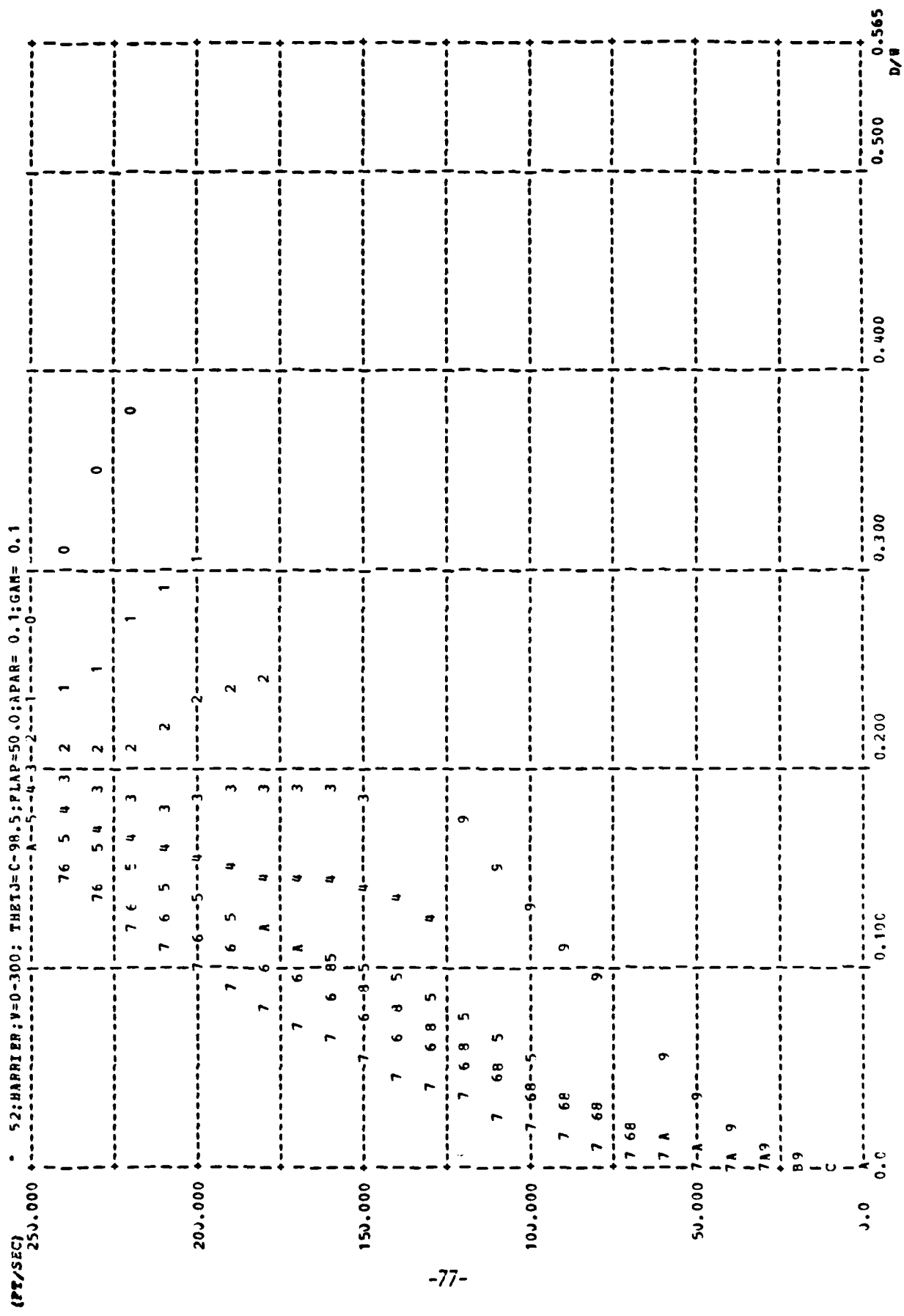
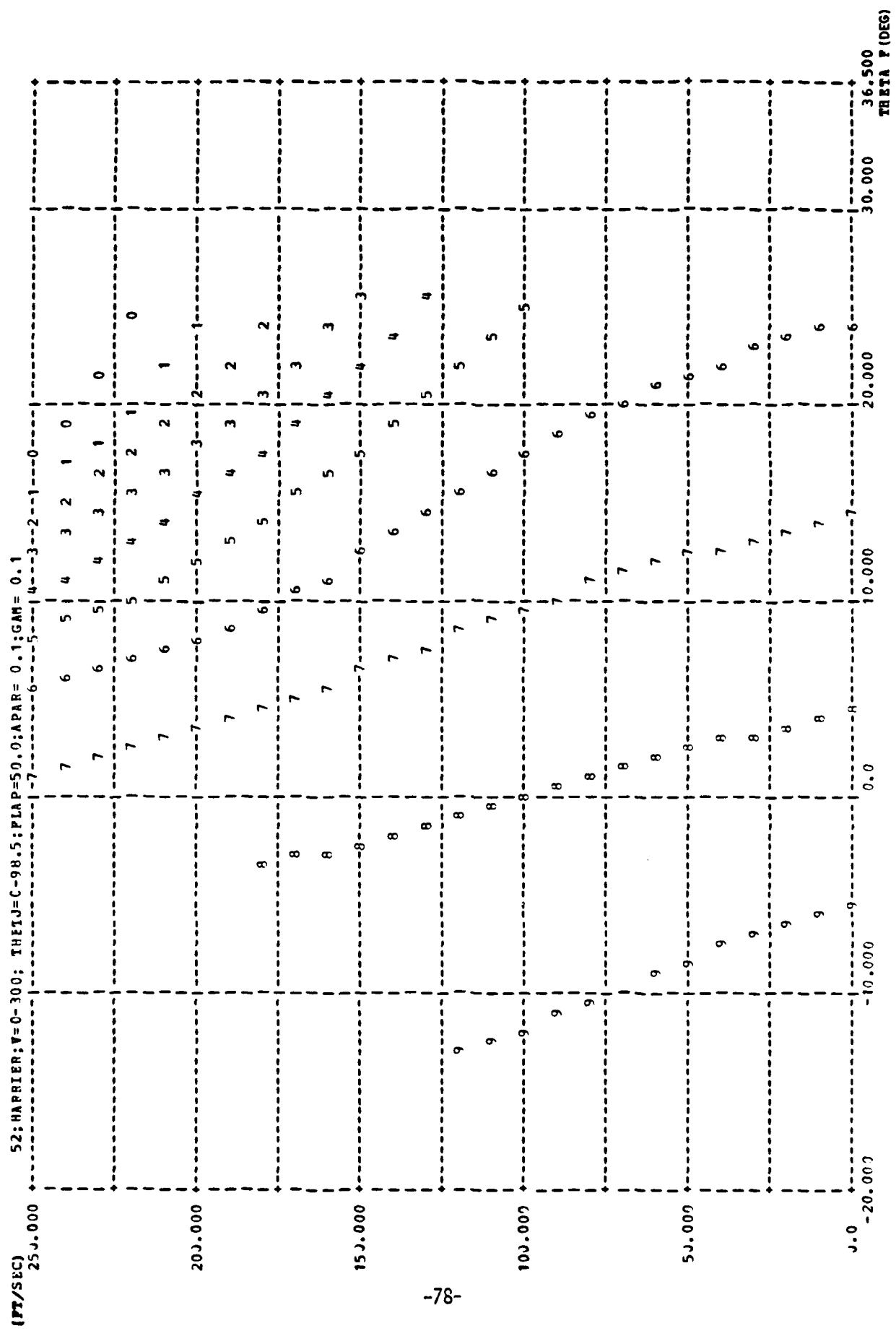


FIGURE 69 - Trimmapp of $D/W(\theta_j, V_\infty)$; with $\delta_F = 50^\circ$, $U_{V_c} = 0.1 g$, $\gamma_c = 0.1 \text{ rad.}$



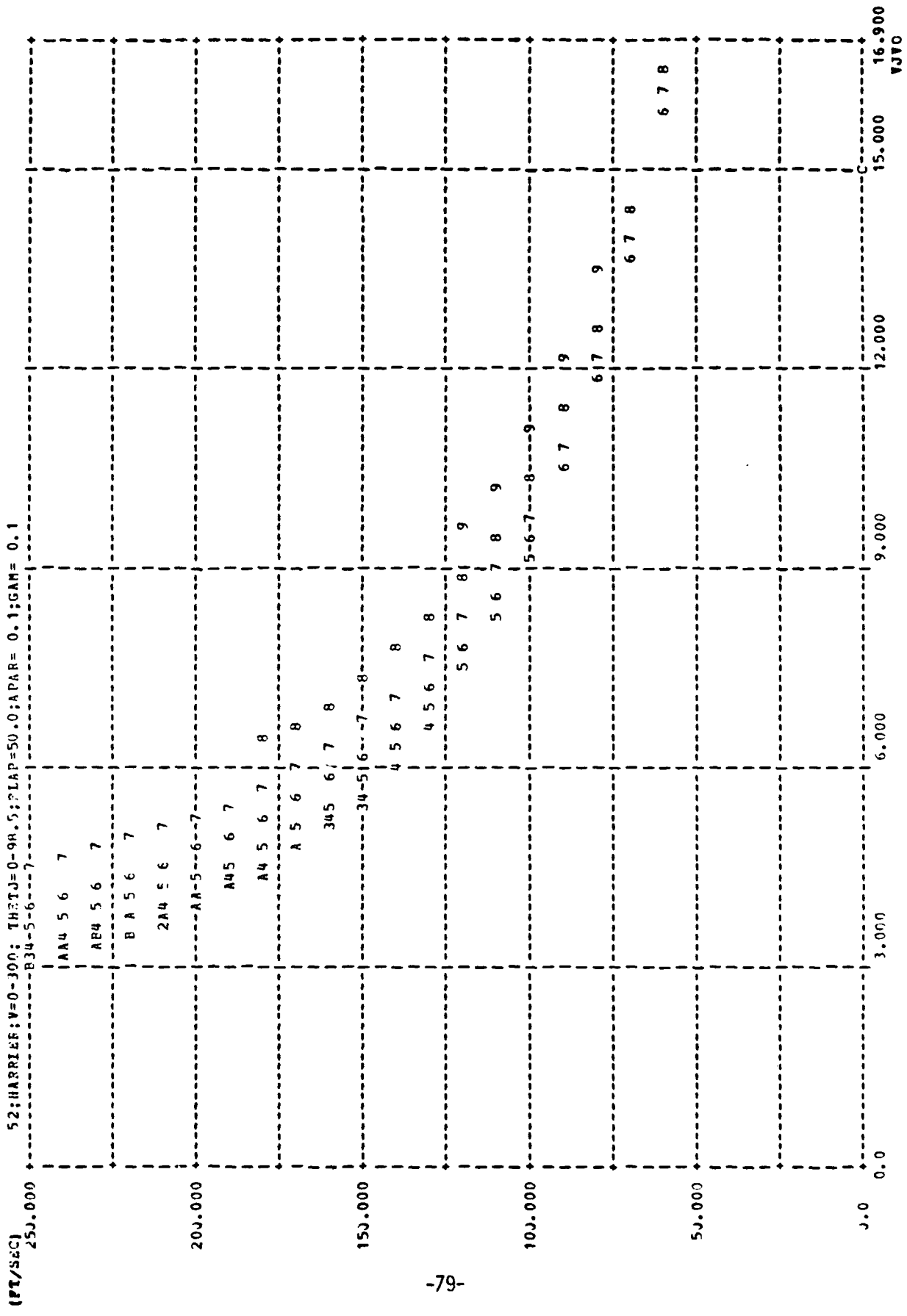


FIGURE 71 - Trimmap of $V_j/V_{\infty}(\theta_j, V_{\infty})$; with $\delta_F = 50^\circ$, $\dot{V}_{V_C} = 0.1$ g, $\gamma_C = 0.1$ rad.

AD-A102 155

PRINCETON UNIV NJ DEPT OF MECHANICAL AND AEROSPACE --ETC F/G 1/2
TRANSITION AND CONVERSION TRIM-MAPS FOR THE AV-8A VTOL AIRCRAFT--ETC(U)
AUG 80 B HILDRETM

N00014-78-C-0381

UNCLASSIFIED

MAE-1466

ONR-CR215-262-1F

NL

2 of 2

AD-A
100-159

END
DATE
FILED
8-31
DTIC

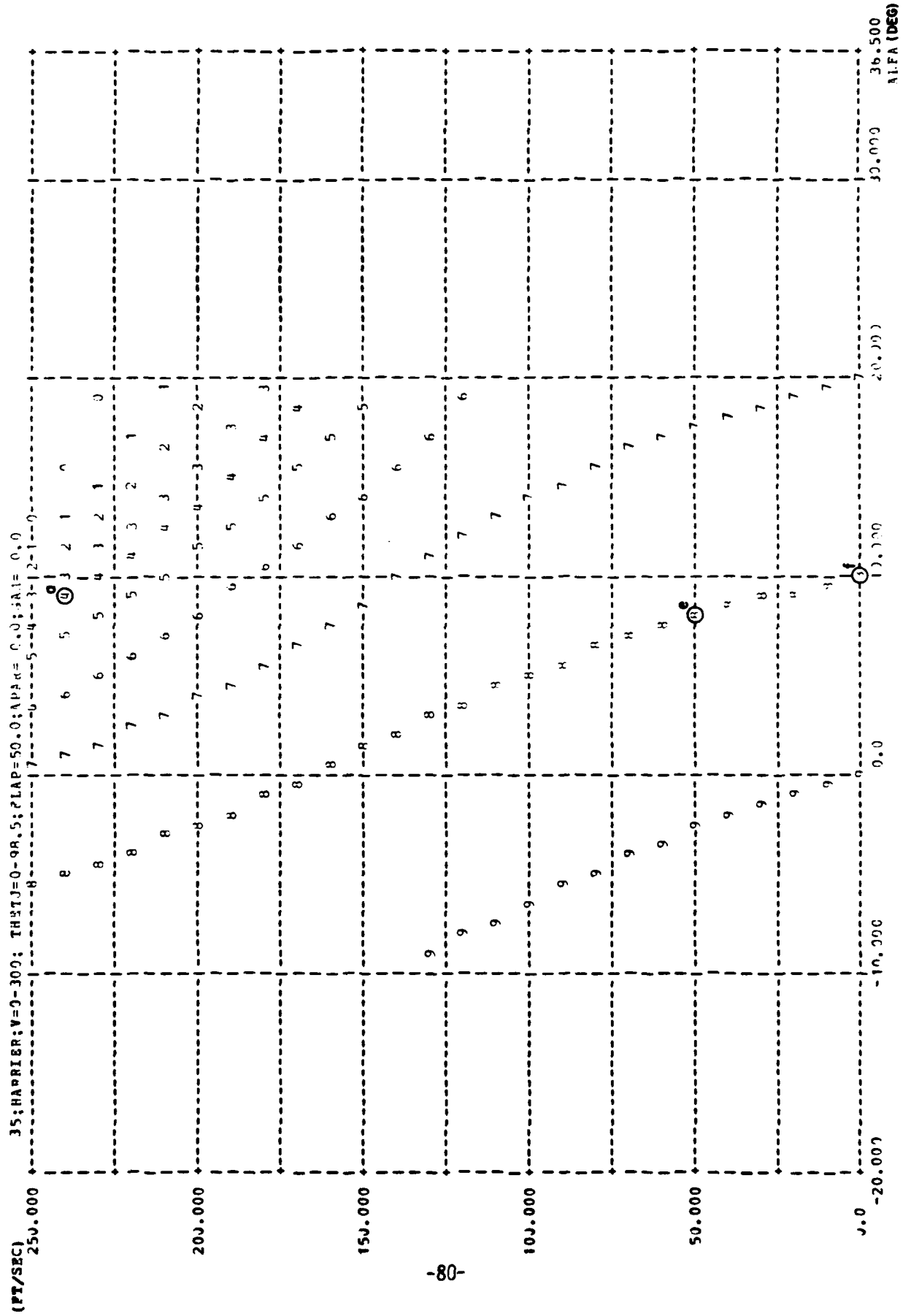


FIGURE 72 - Trimmap of $\alpha(\theta_j, v_\infty)$; with $\delta_F = 50^\circ$, $q_{v_c} = 0.0$ g, $\gamma_c = 0.0$ rad.

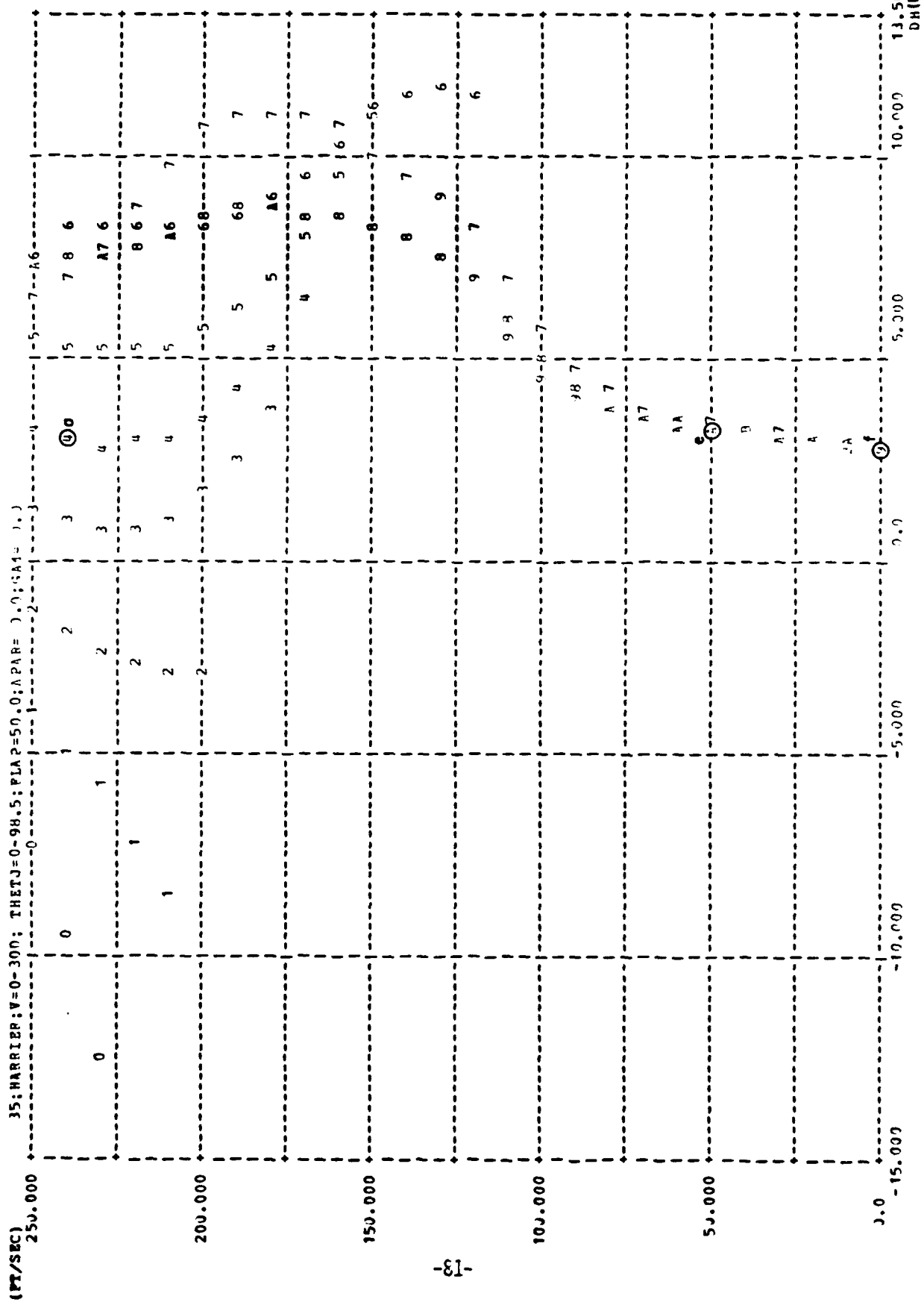


FIGURE 73 - Trimmap of $\delta_H(\theta_j, V_\infty)$; with $\delta_F = 50^\circ$, $\dot{V}_{v_c} = 0.0$ g, $\gamma_c = 0.0$ rad.

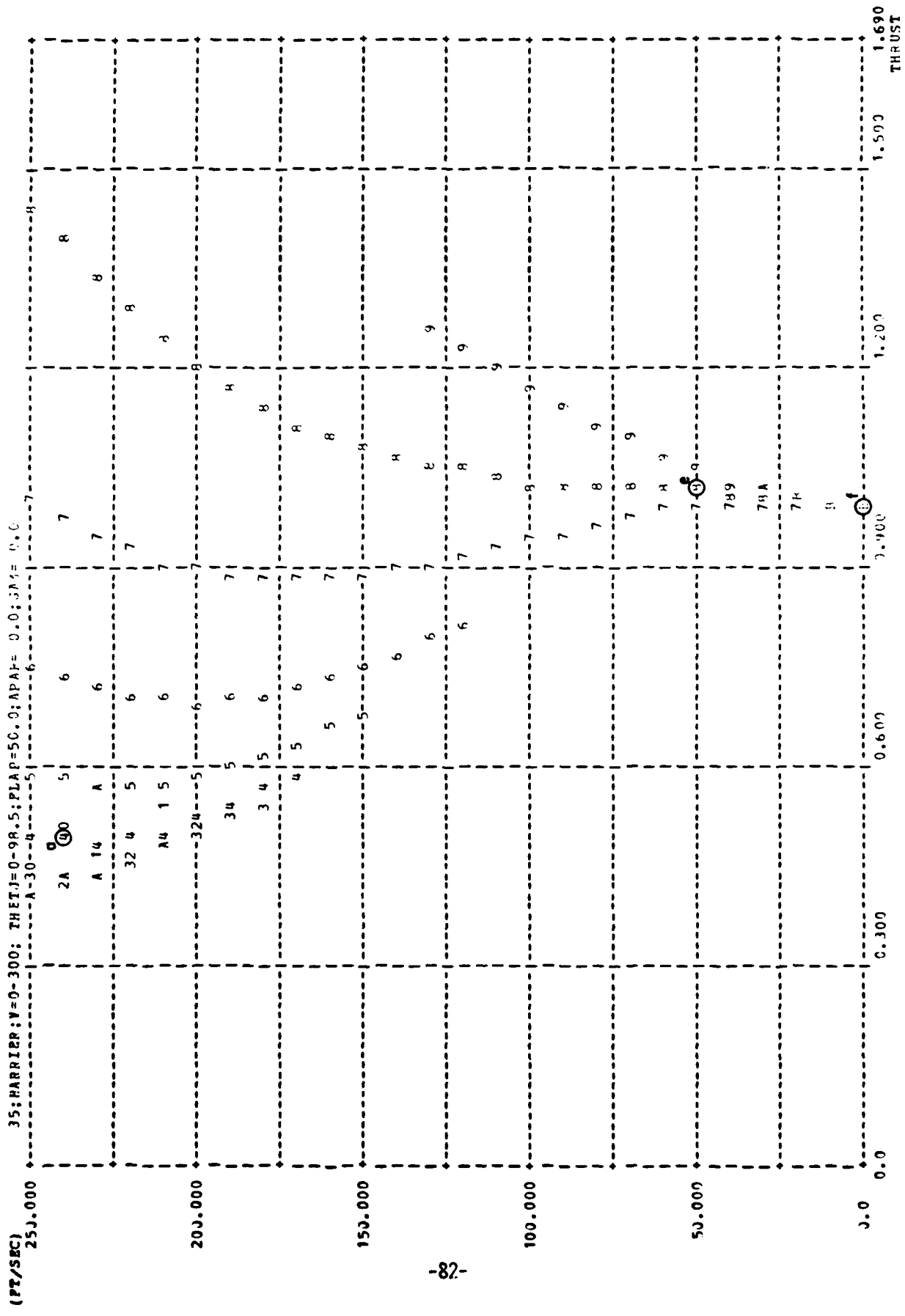


FIGURE 74 - Trimmap of $T/W(\theta_j, V_\infty)$; with $\delta_F = 50^\circ$, $\eta_{V_C} = 0.0$ g, $\gamma_C = 0.0$ rad.

35; HAPRIER; W=9-300; TH; RJ=0-398.5; TAP=50.0; MAR=7.0; J; JAM= 0, C

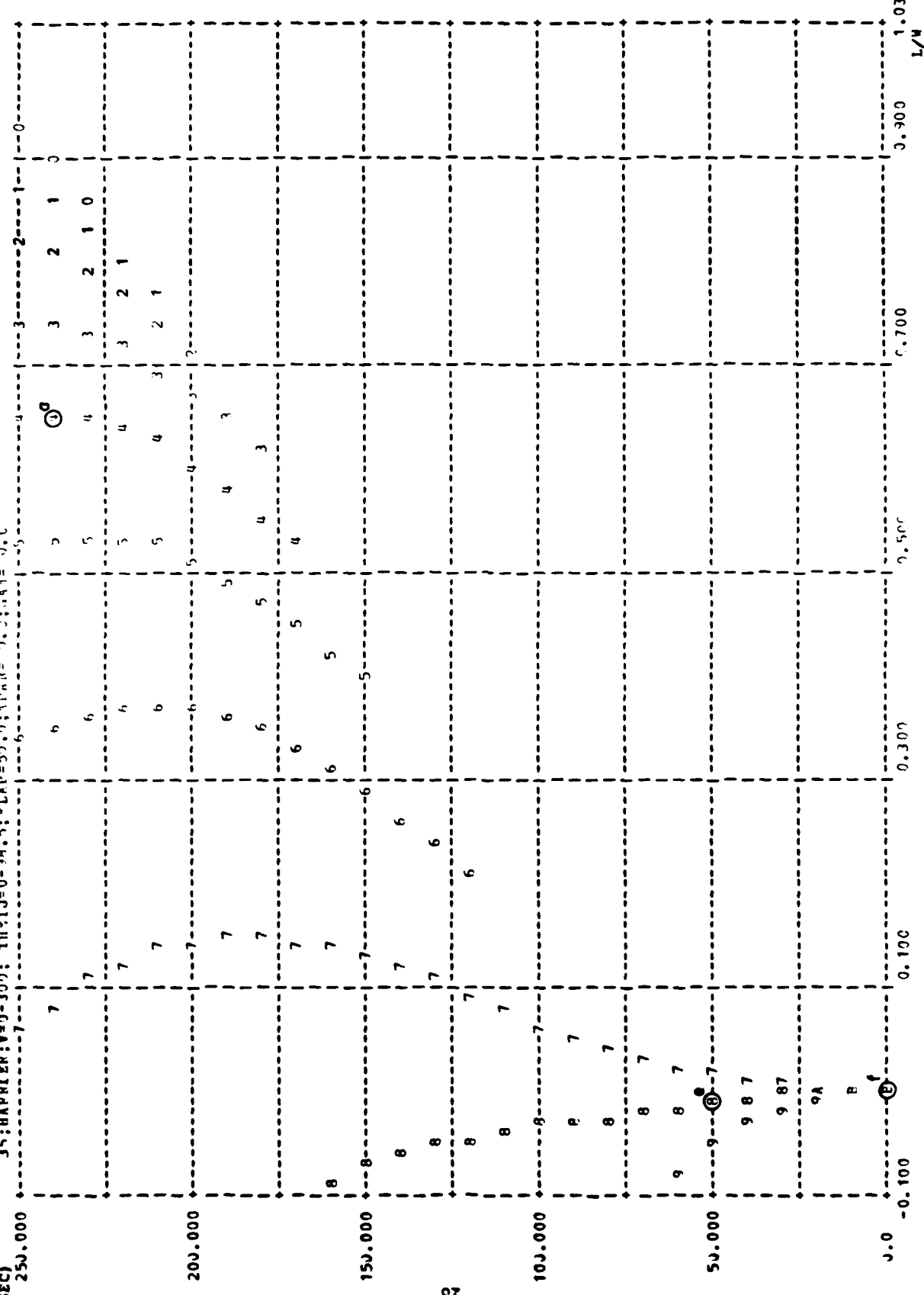


FIGURE 75 - Trimmap of $L/W(\theta_j, V_\infty)$; with $\delta_F = 50^\circ$, $V_C = 0.0$ g, $\gamma_C = 0.0$ rad.

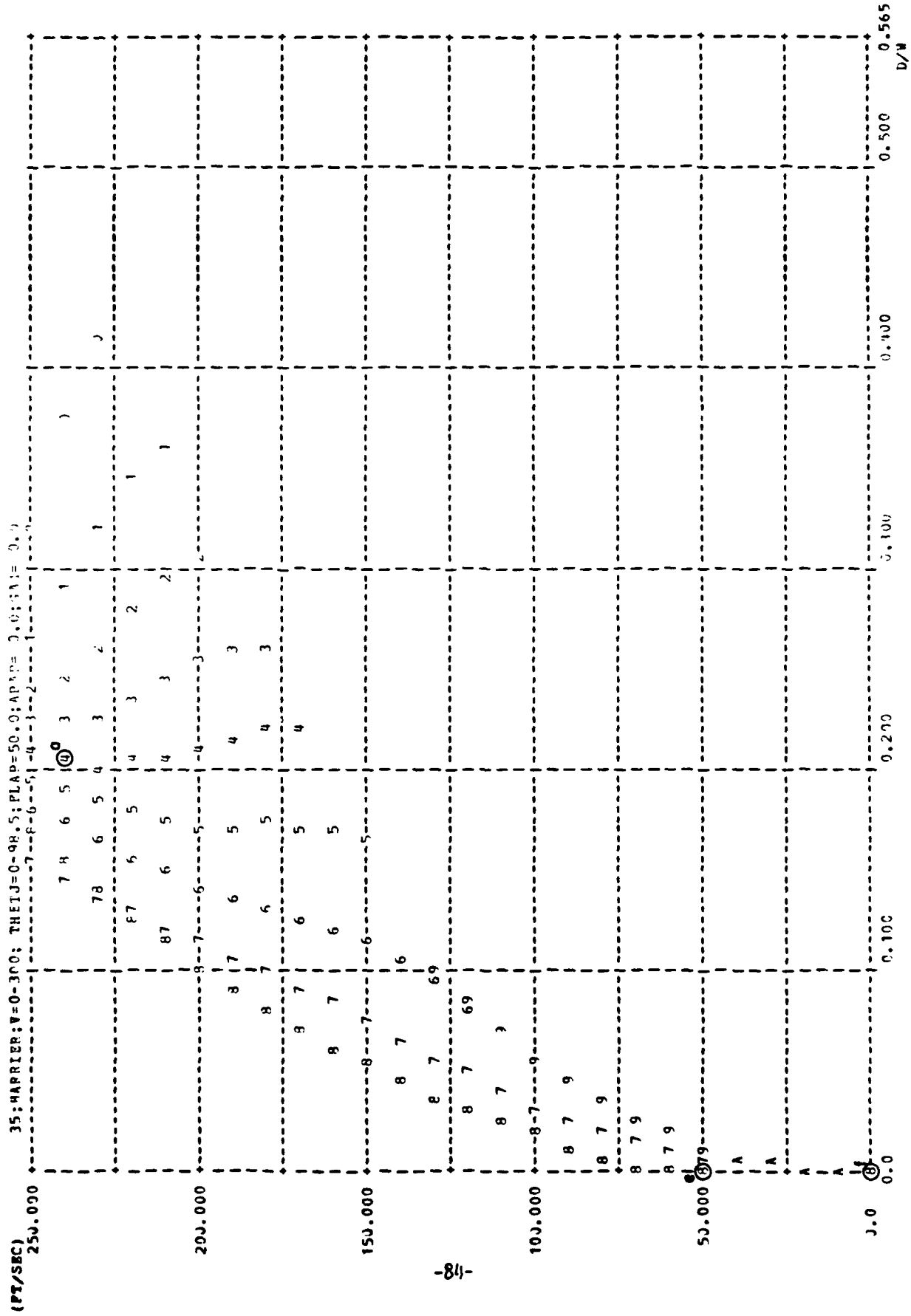


FIGURE 76 - Trimmable of $D/H(\theta_f, V_\infty)$; with $\delta_f = 50^\circ$, $\dot{V}_{V_C} = 0.0 \text{ g}$, $\gamma_C = 0.0 \text{ rad}$.

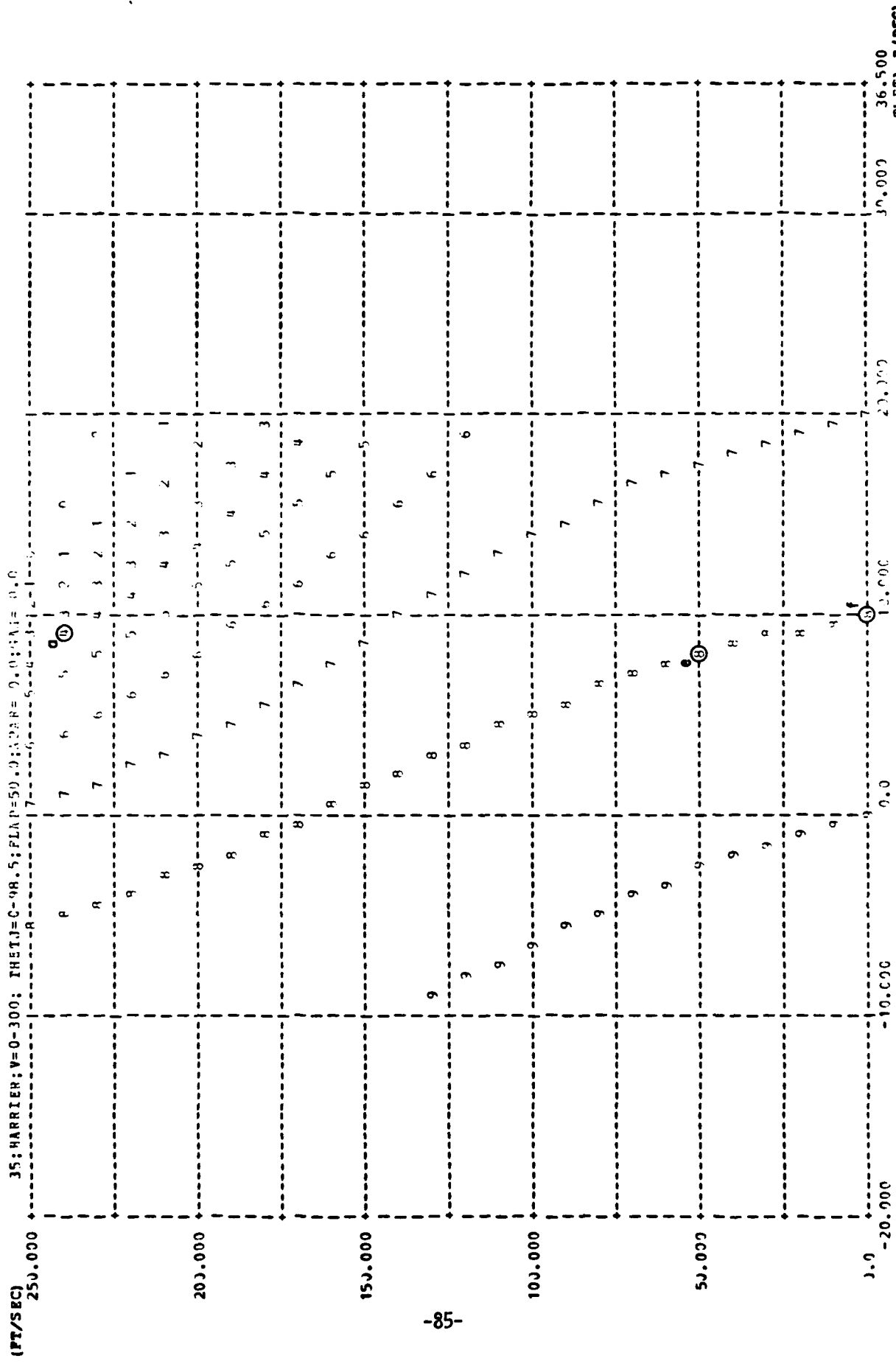


FIGURE 77 - Trimmap of $\theta(\theta_j, V_m)$; with $\delta_f = 50^\circ$, $V_{V_c} = 0.0$ g, $\gamma_c = 0.0$ rad.

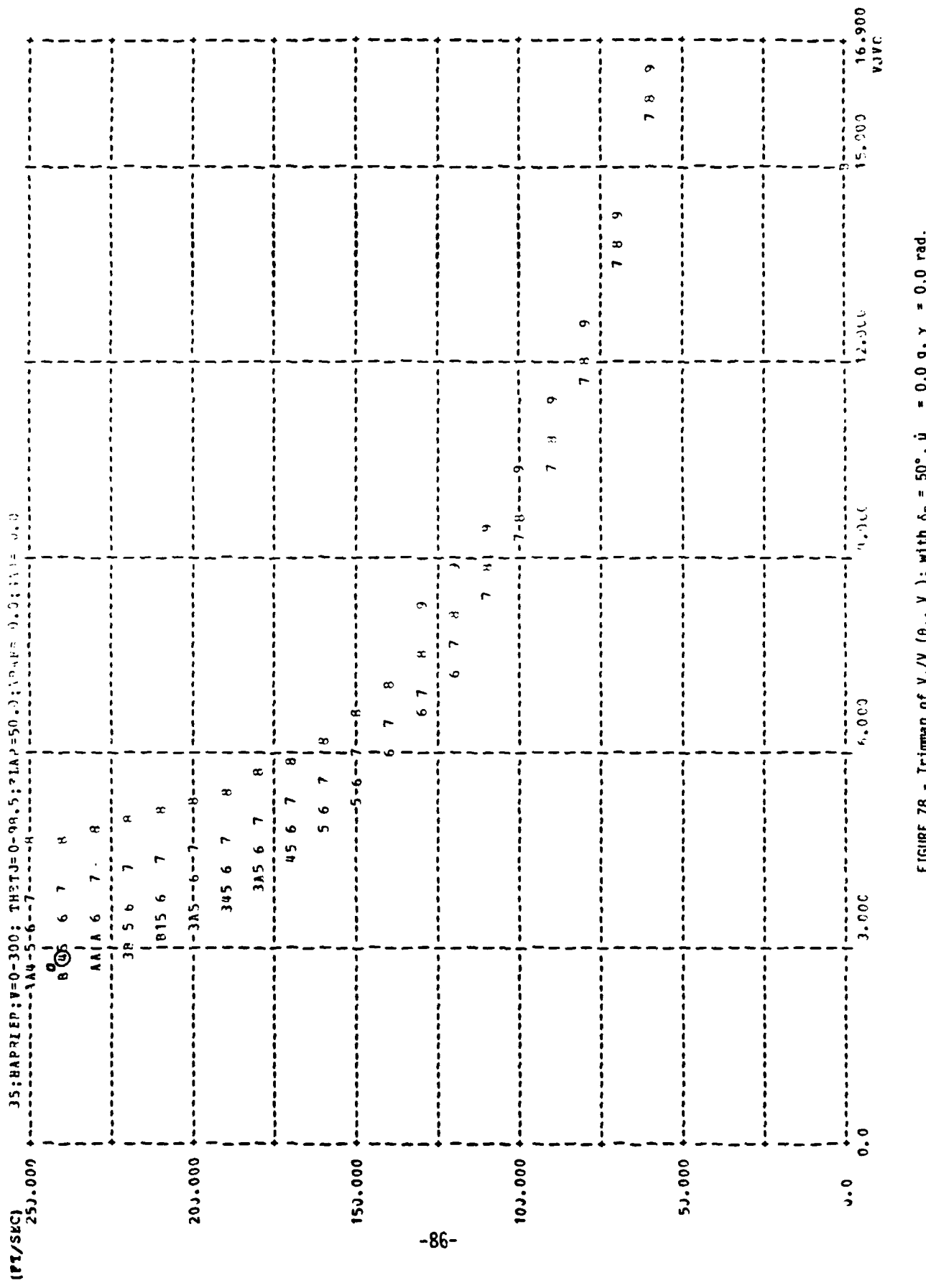


FIGURE 78 - Trimmapp of $V_j/V_\infty(\theta_j, V_\infty)$: with $\delta_f = 50^\circ$, $\dot{u}_V = 0.0$ g, $\gamma_c = 0.0$ rad.

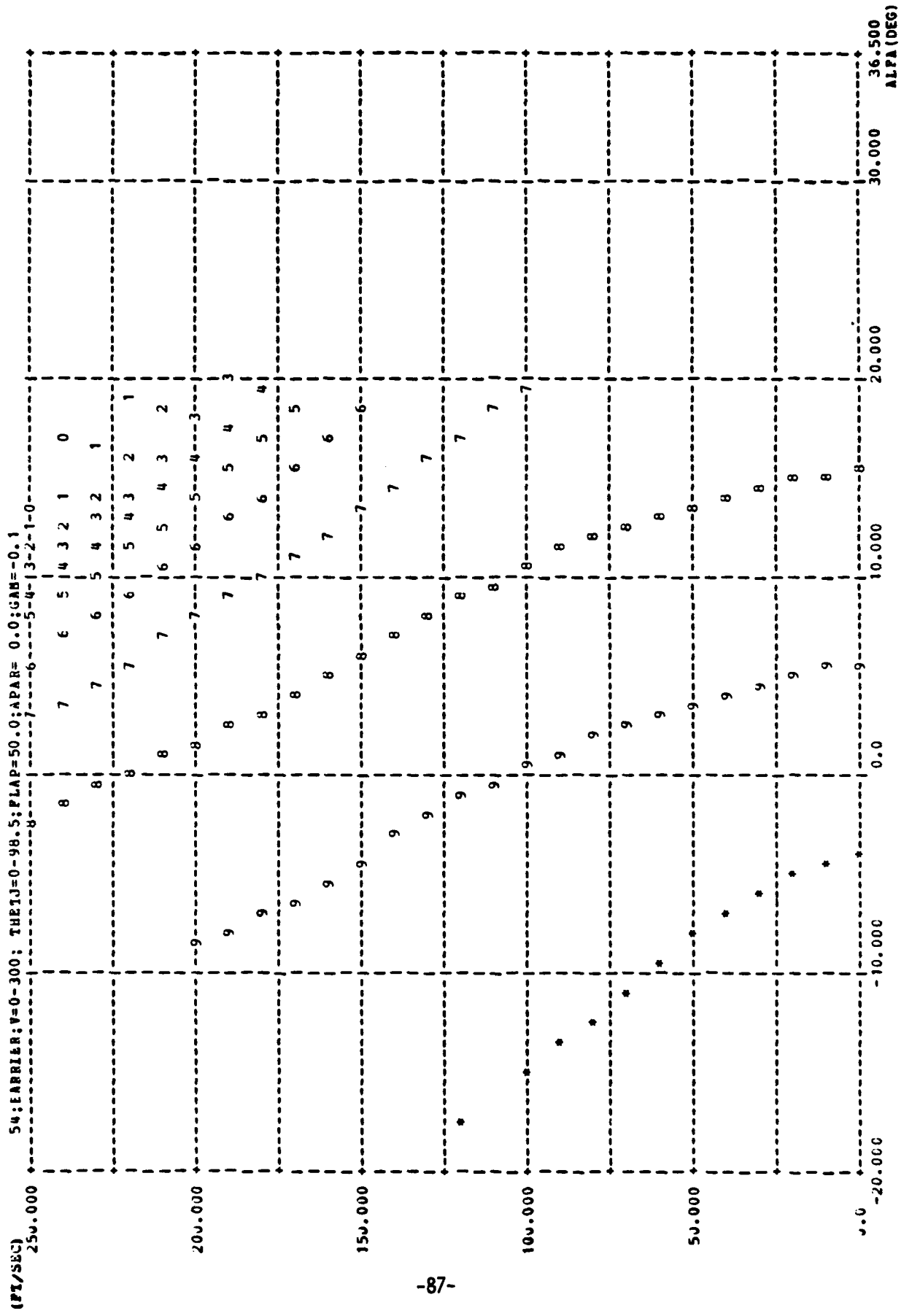


FIGURE 79 - Trimmap of $\alpha(\theta_j, V_\infty)$; with $\delta_F = 50^\circ$, $V_\infty = 0.0$ g, $\gamma_c = -0.1$ rad.

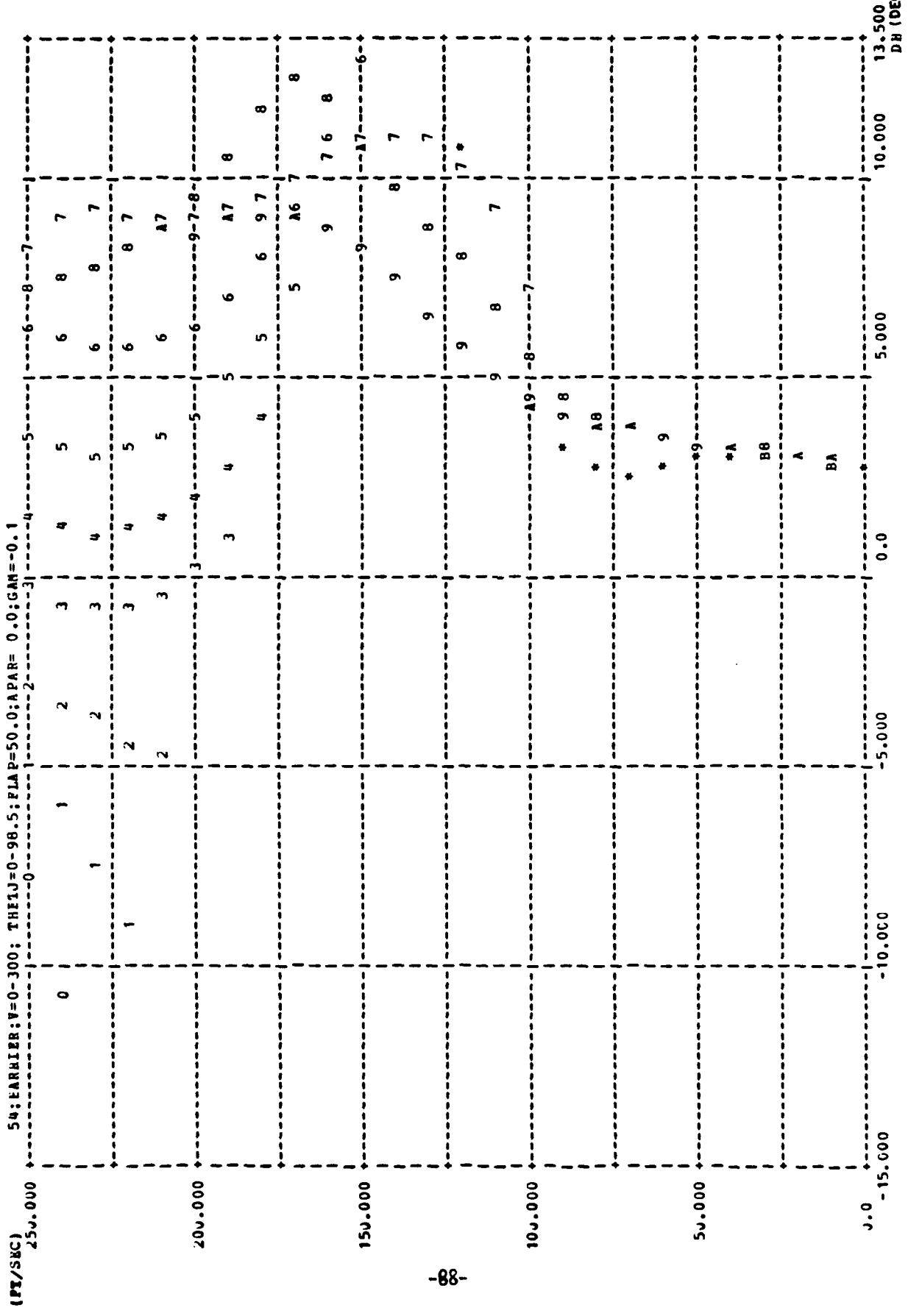


FIGURE 80 - Trimmapp of $\delta_H(\theta_j, v_\infty)$; with $\delta_F = 50^\circ$, $v_\infty = 0.0$ g, $\gamma_c = -0.1$ rad.

54: FARRIER: V=0-300; THETJ=0-98.5; PLAP=50.0; APAR= 0.0; GAM=-0.1

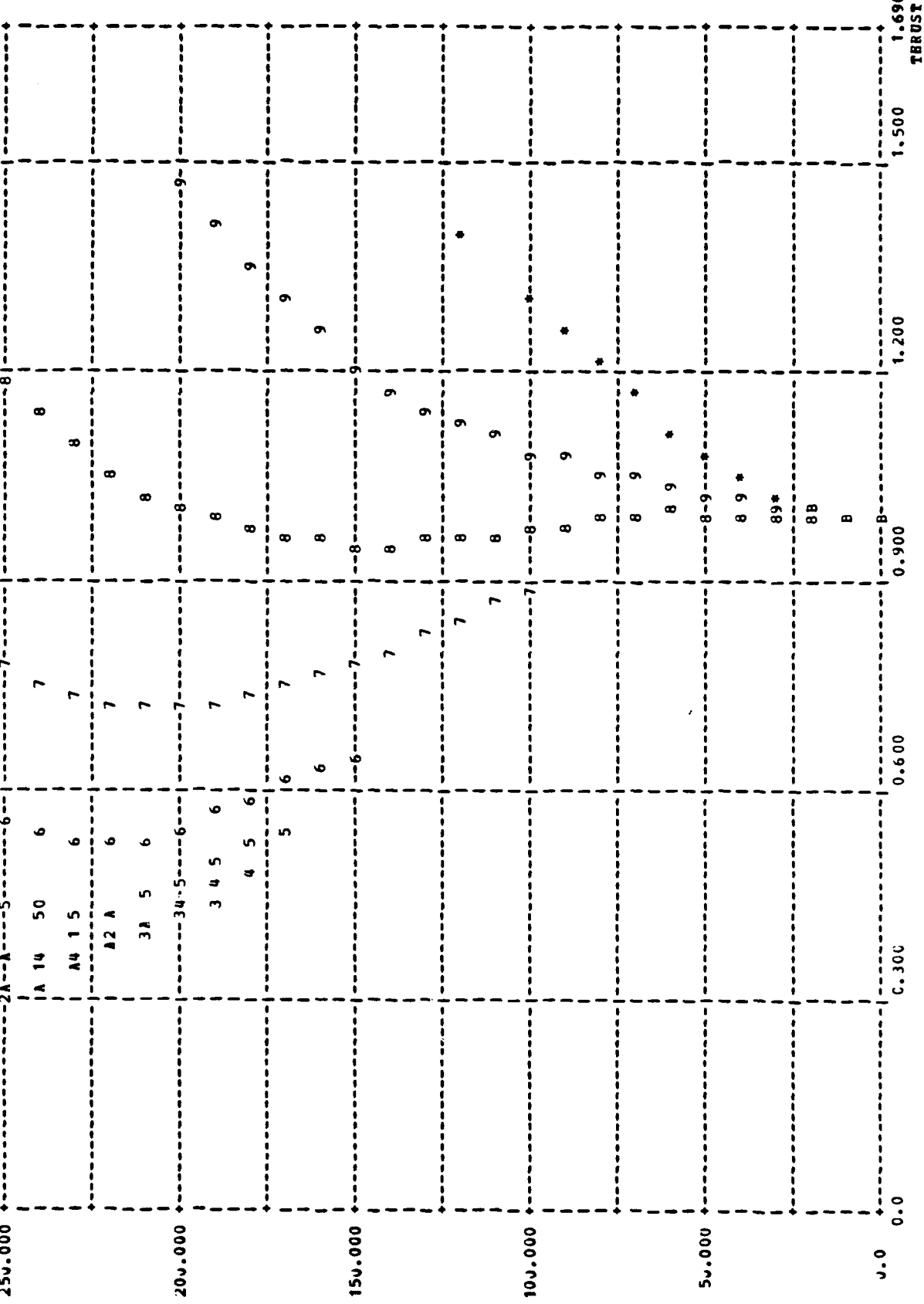


FIGURE 81 - Trimmap of $T/W(\theta_j, V_\infty)$; with $\delta_F = 50^\circ$, $d_{V_C} = 0.0$ g, $\gamma_C = -0.1$ rad.

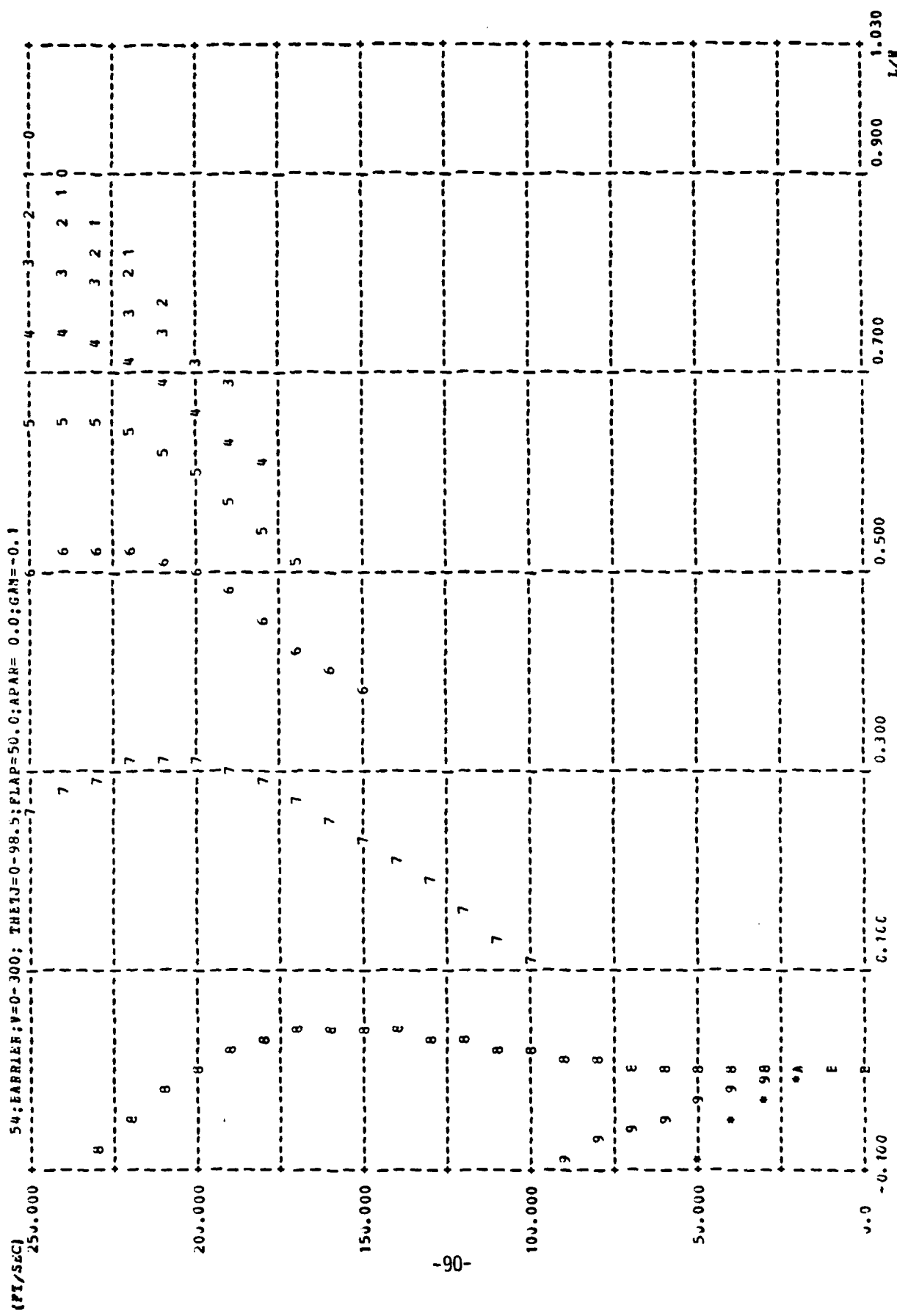


FIGURE 82 - Trimmap of $L/W(\theta_j, v_\infty)$; with $\delta_f = 50^\circ$, $v_\infty = 0.0$ g, $\gamma_c = -0.1$ rad.

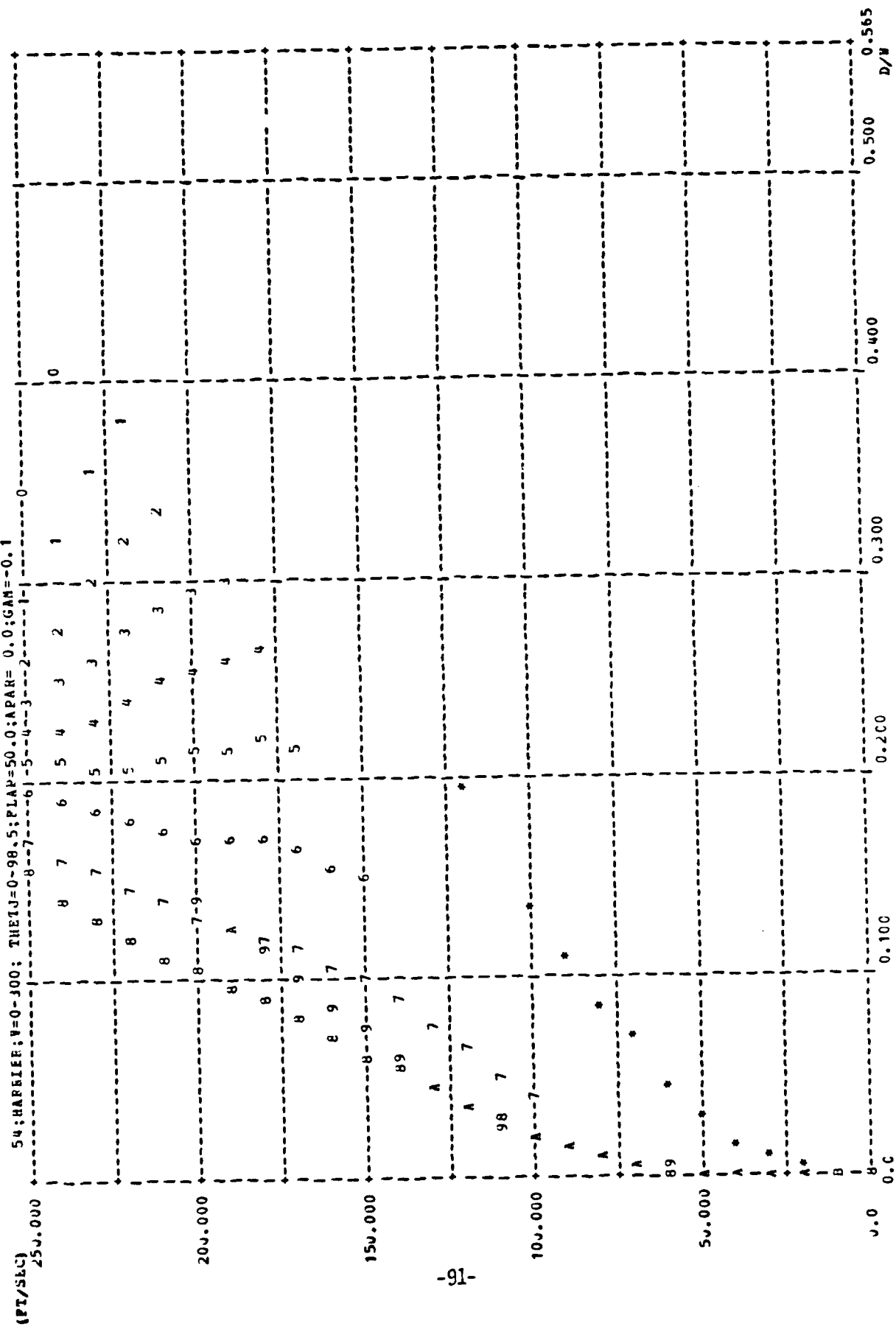


FIGURE 83 - Trimmapp of D/W(α_j , v_∞); with $\delta_F = 50^\circ$, $\dot{v}_{v_C} = 0.0$ g, $\gamma_C = -0.1$ rad.

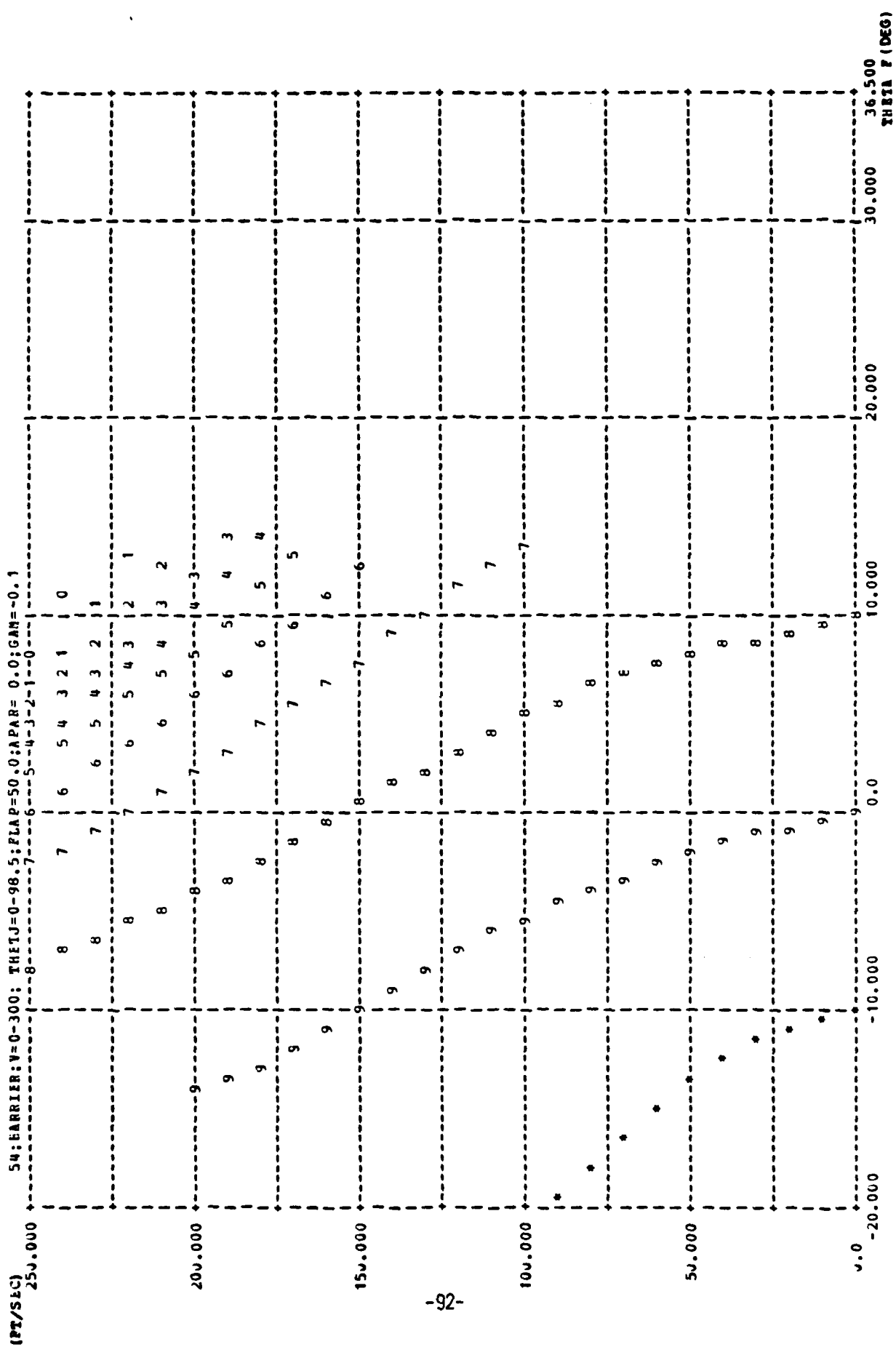


FIGURE 84 - Trimmap of $\theta(\theta_j, V_\infty)$; with $\delta_F = 50^\circ$, $V_{V_C} = 0.0 \text{ g}$, $\gamma_C = -0.1 \text{ rad}$.

54: BARRIERE: V=0-300; THEIJ=0-98.5; P1AP=50.0; APAR= 0.0; GAM=-0.1

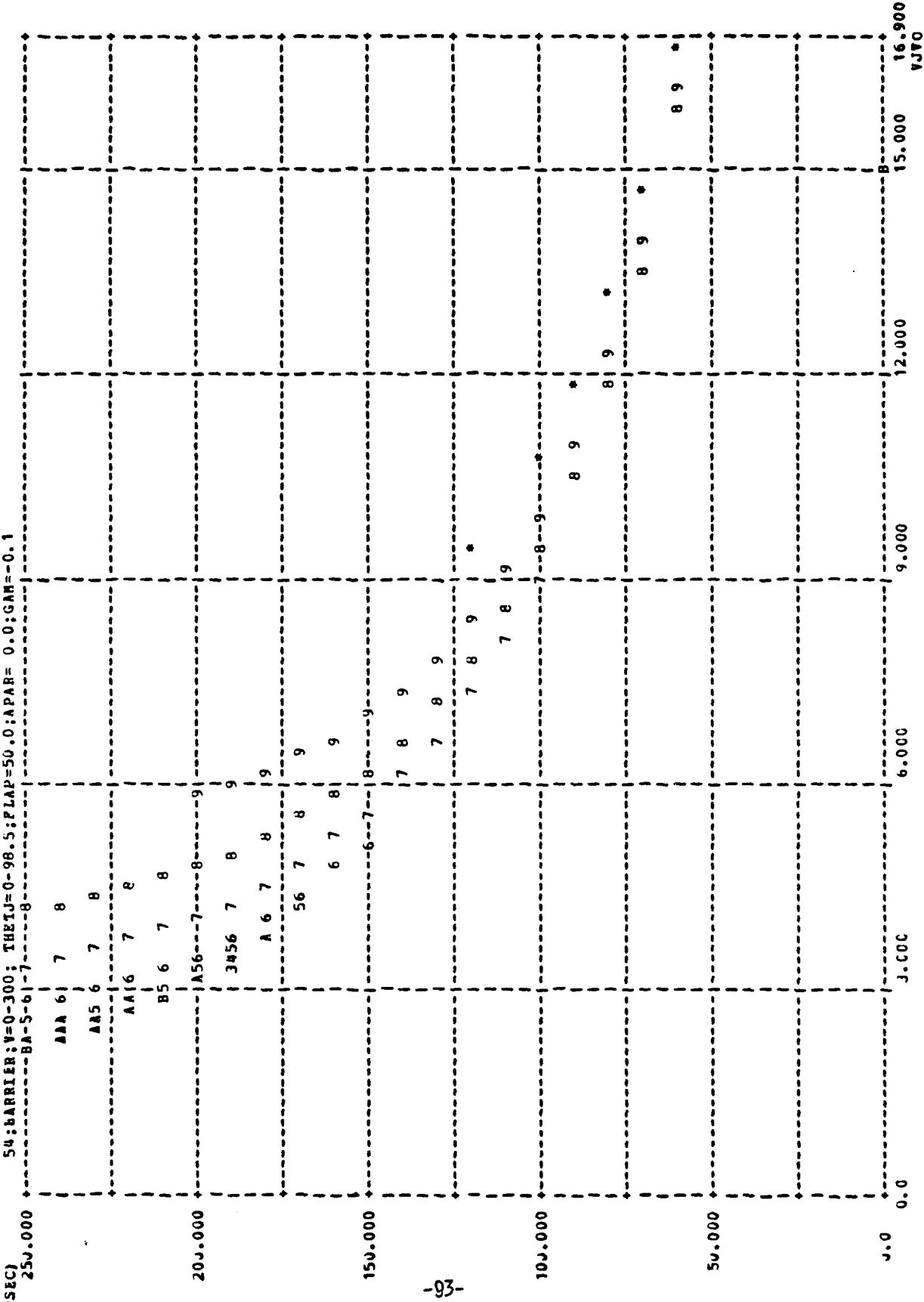


FIGURE 85 - Trimmap of $V_j/V_{m\infty}(\theta_j, V_\infty)$; with $\delta_F = 50^\circ$, $V_\infty = 0.09$, $\gamma_C = -0.1$ rad.

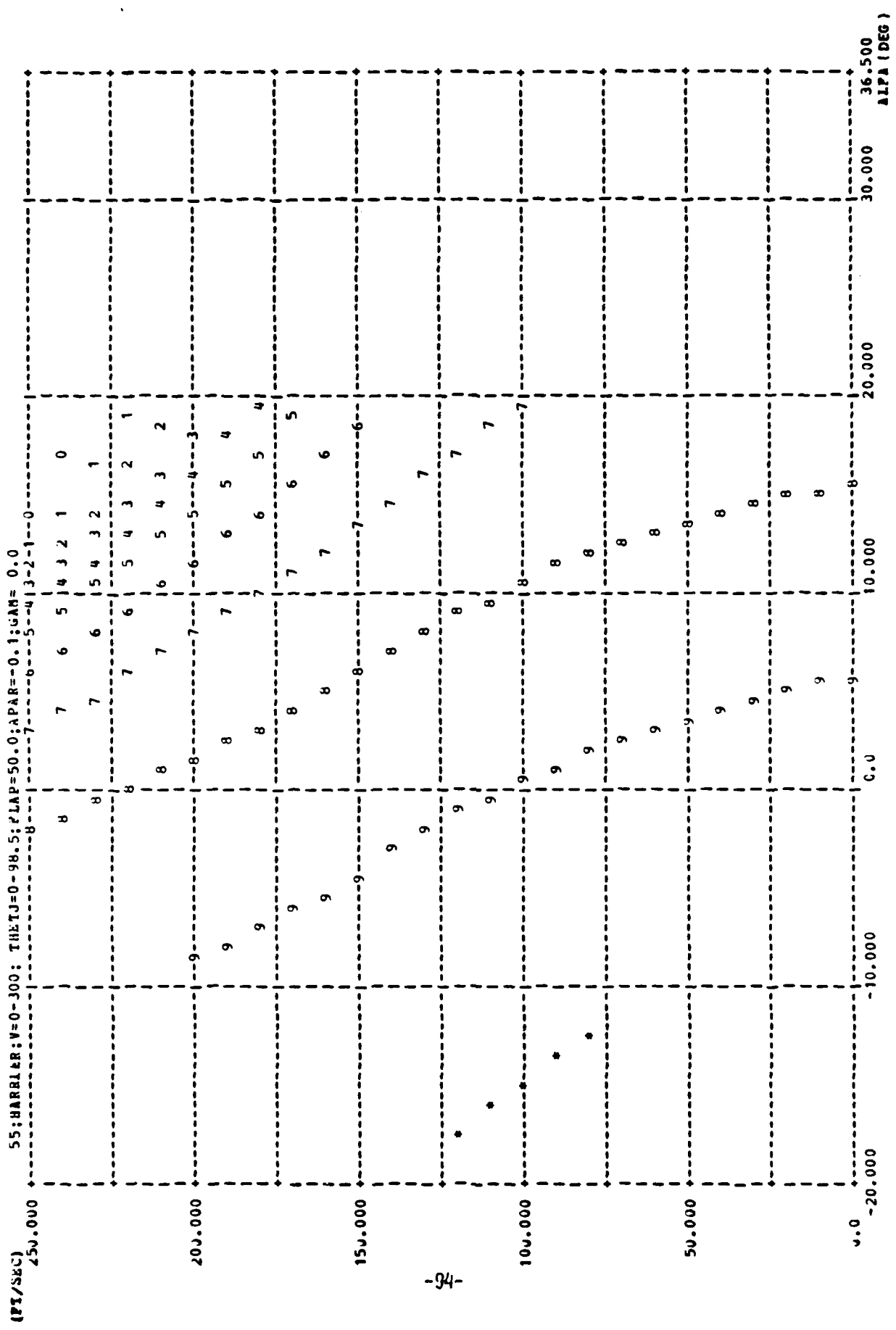


FIGURE 86 - Trimmap of $\alpha(\theta_j, \gamma_\infty)$; with $\delta_F = 50^\circ$, $\delta_{V_C} = -0.1$ g, $\gamma_C = 0.0$ rad.

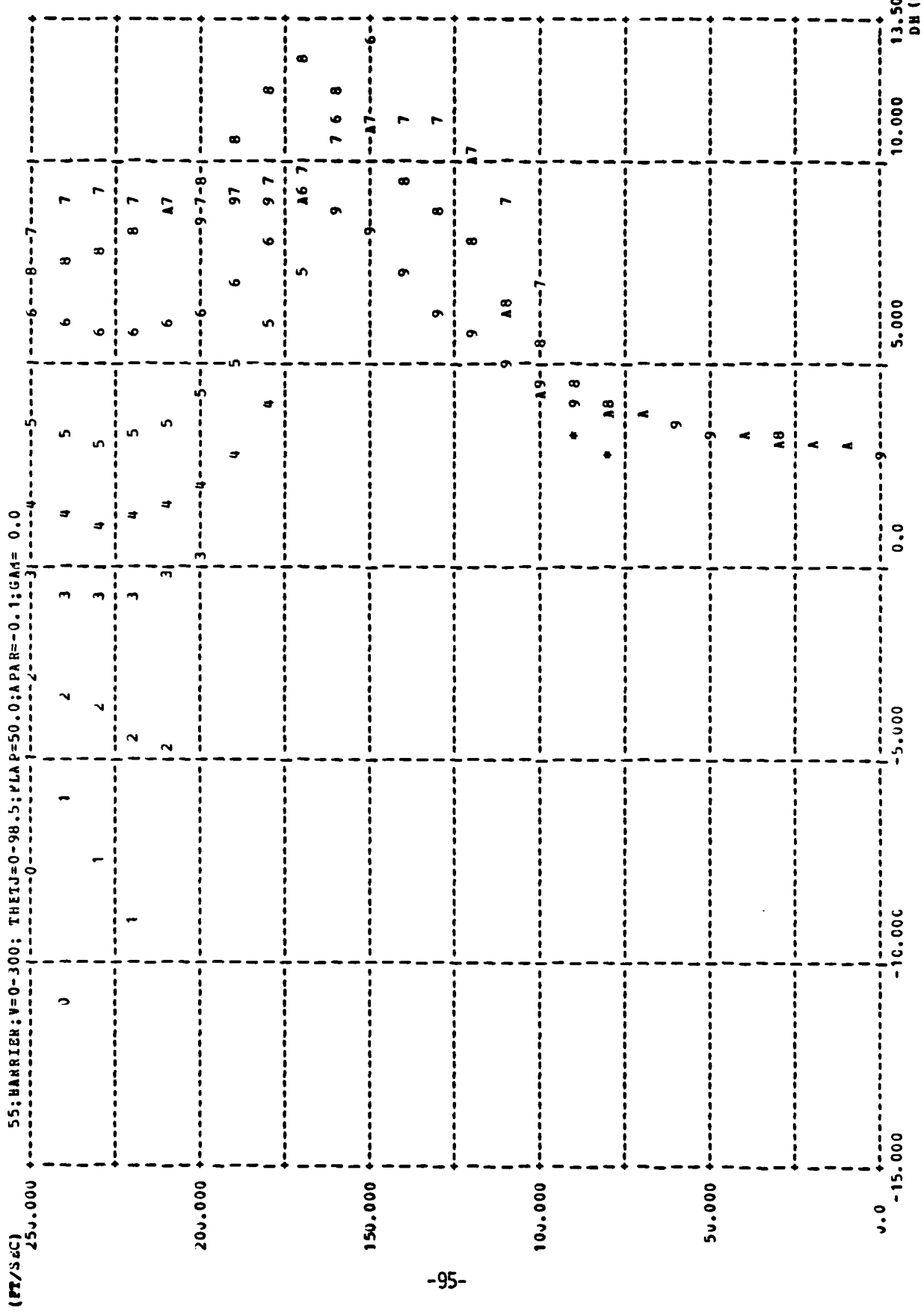
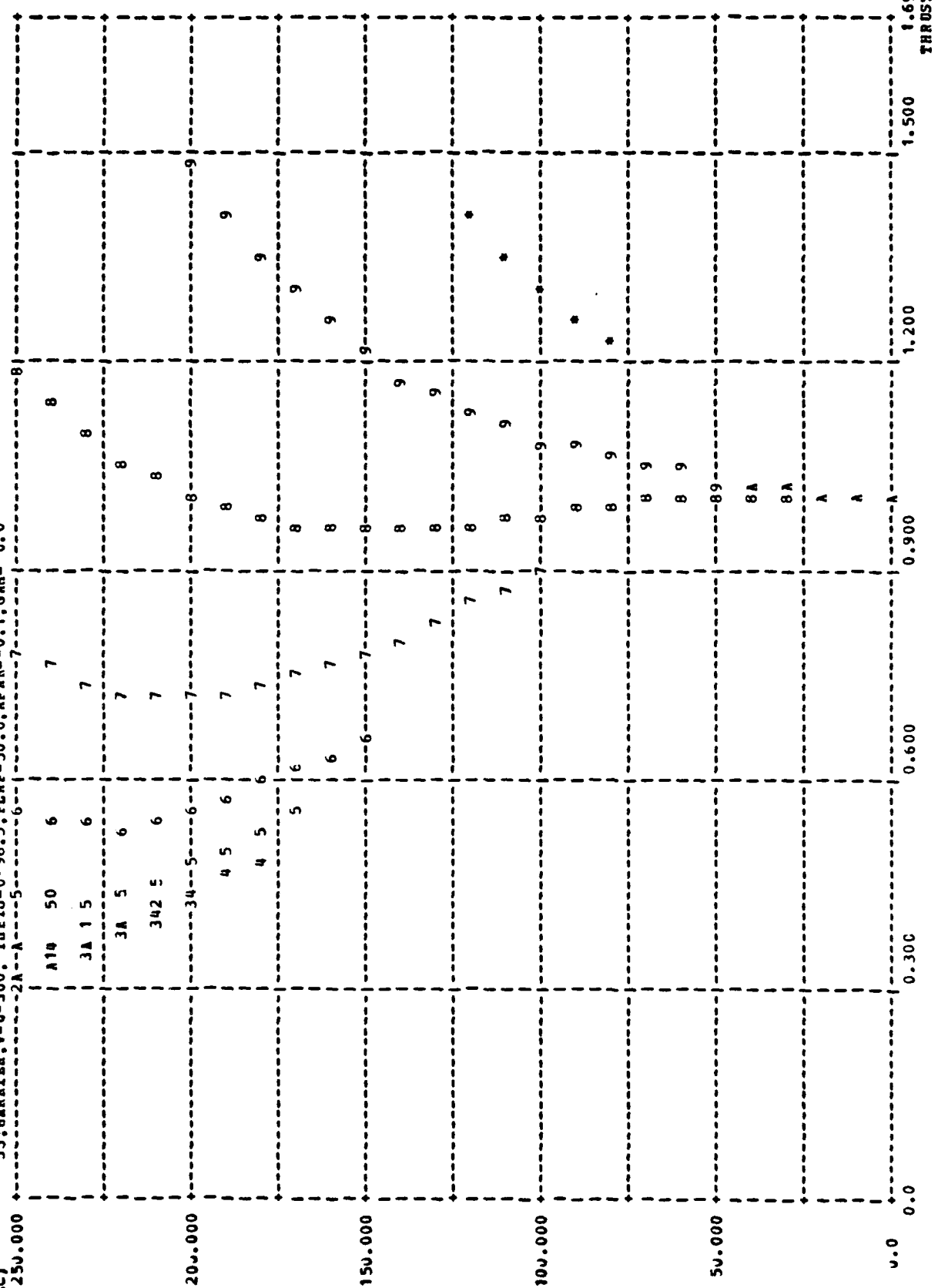


FIGURE 87 - Trimmap of $\delta_H(\theta_j, V_\infty)$; with $\delta_F = 50^\circ$, $\delta_{V_C} = -0.1$ g, $\gamma_C = 0.0$ rad.

(PT/SUBC) 55; HARRIER; I=0-300; THEIJ=0-98.5; PLAP=50.0; APAR=-0.1; GAM= 0.0



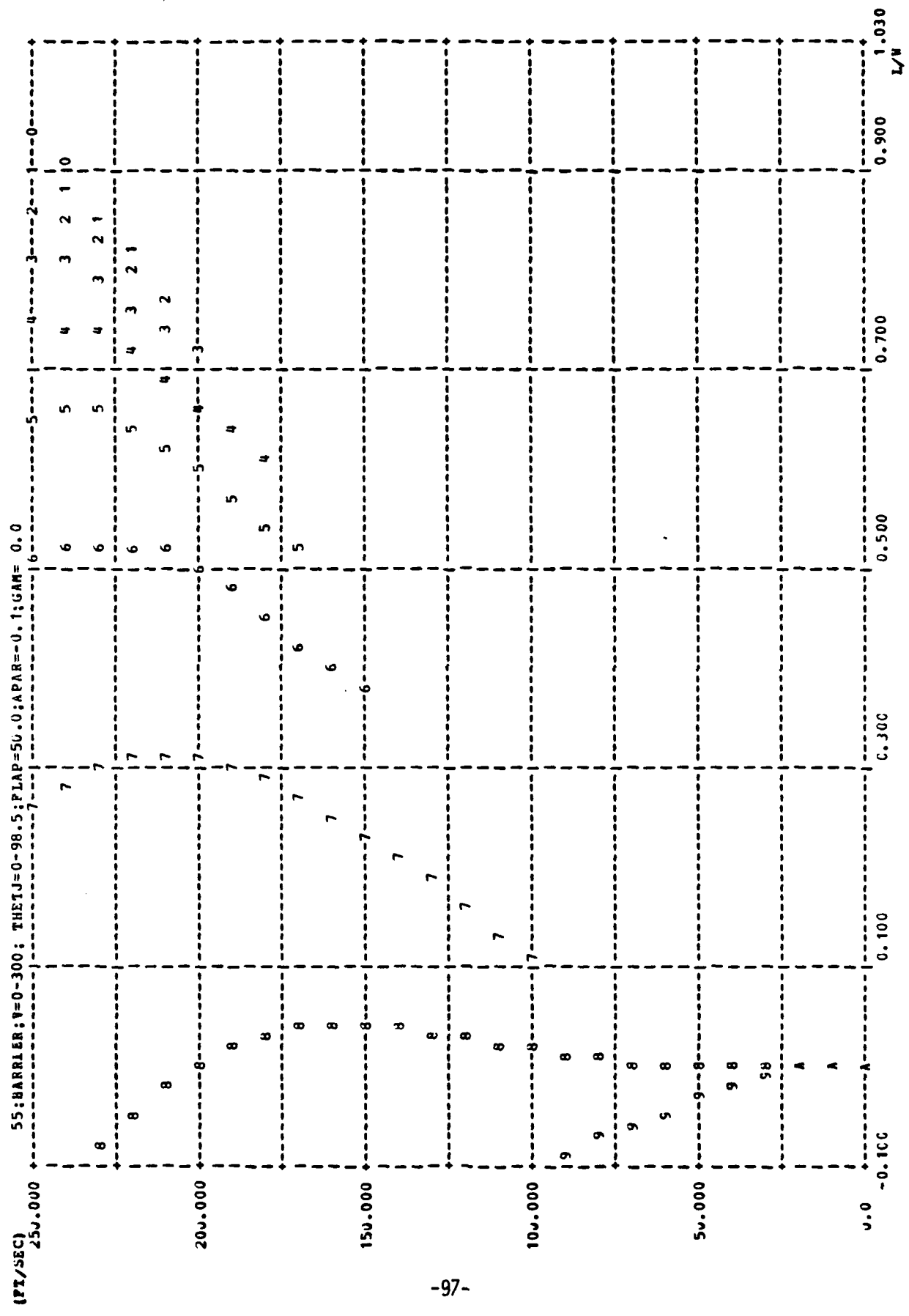


FIGURE 89 - Trimmap of $L/W(\theta_j, v_\infty)$; with $\delta_F = 50^\circ$, $\dot{v}_{V_C} = -0.1 g$, $\gamma_C = 0.0$ rad.

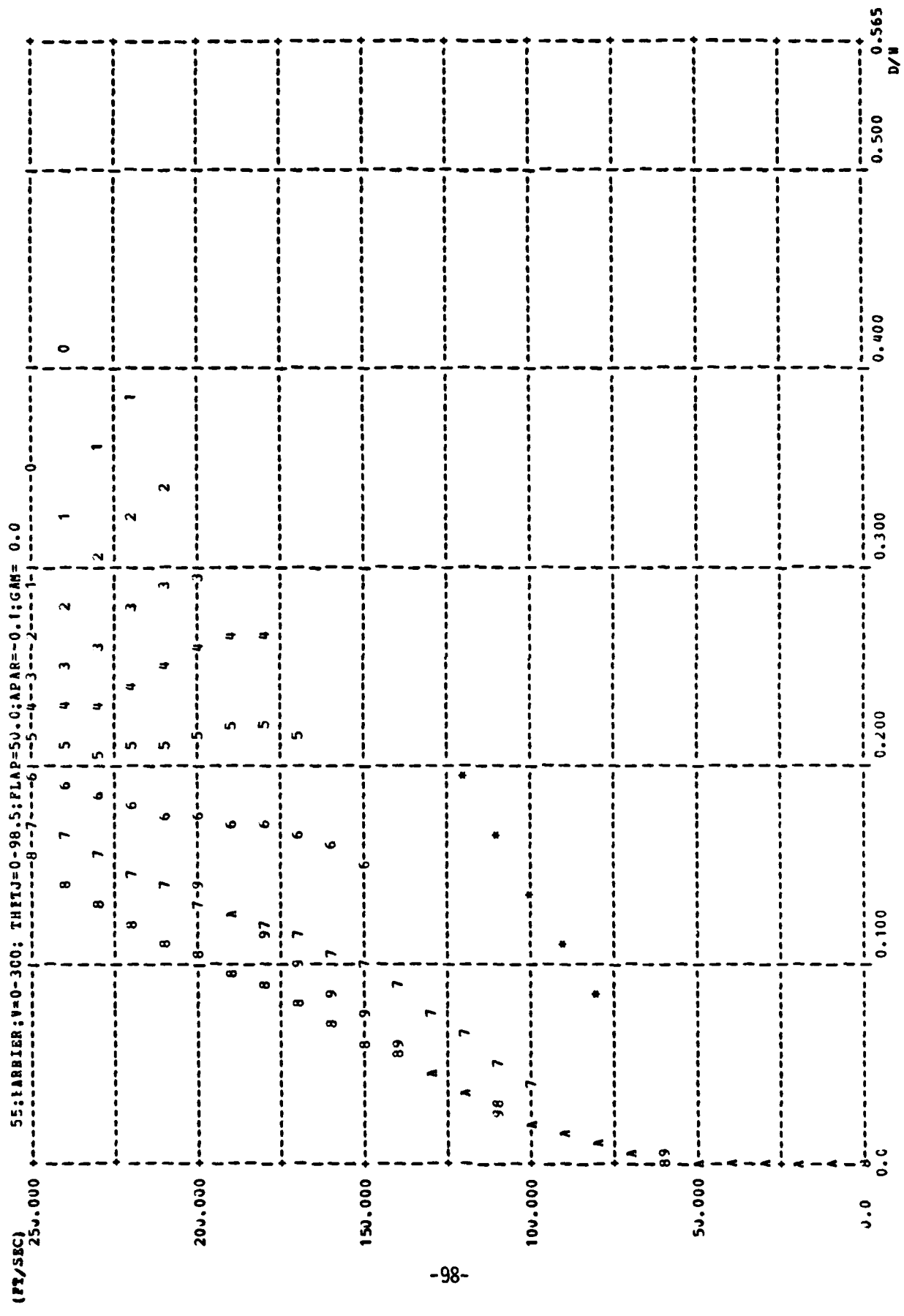


FIGURE 90 - Trimmap of D/W(θ_j , V_∞); with $\delta_F = 50^\circ$, $u_{V_C} = -0.1$ g, $\gamma_C = 0.0$ rad.

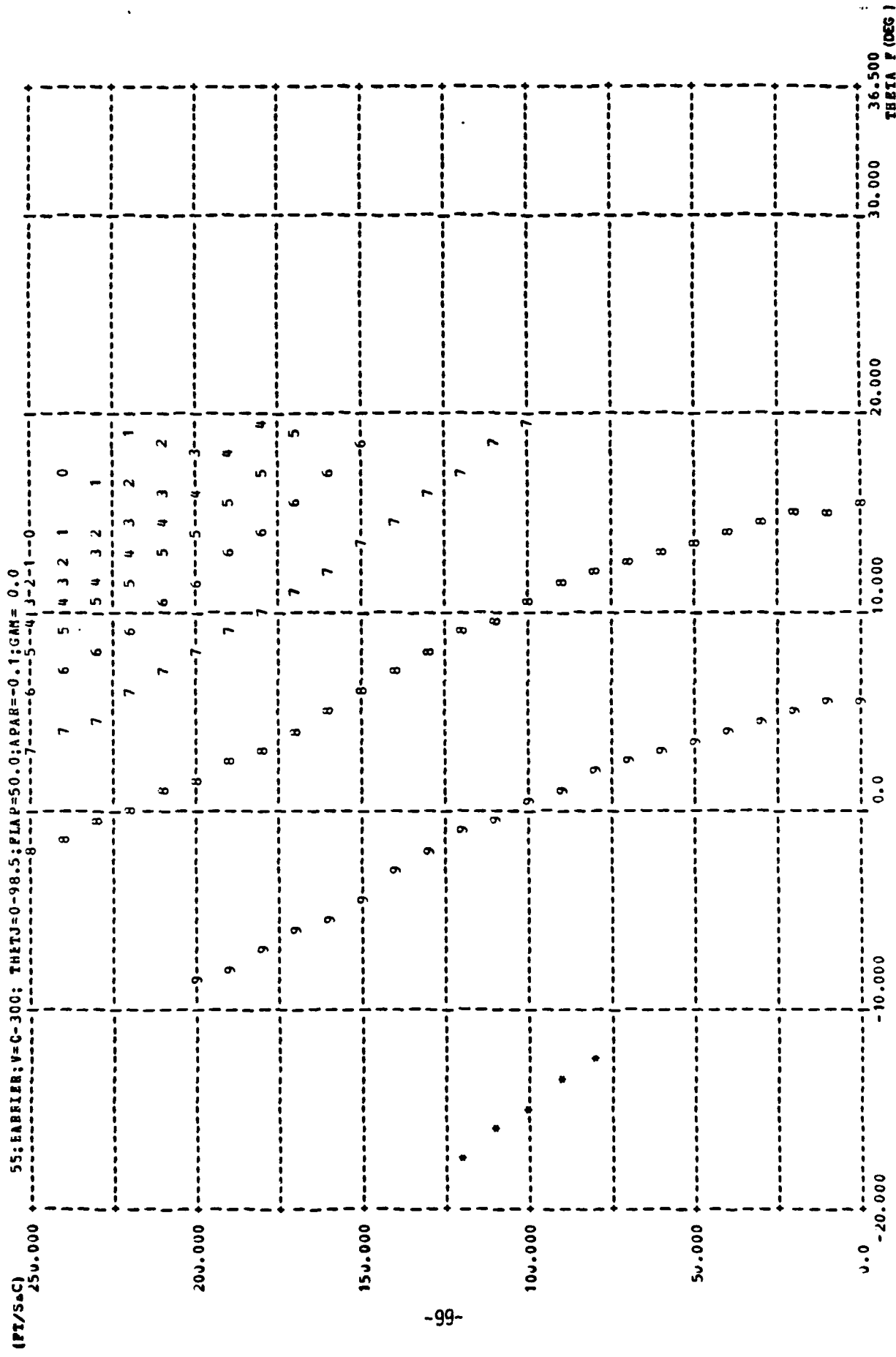


FIGURE 91 - Triimap of $\theta(\theta_J, V_\infty)$; with $\delta_F = 50^\circ$, $U_{V_C} = -0.1$ g, $\gamma_C = 0.0$ rad.

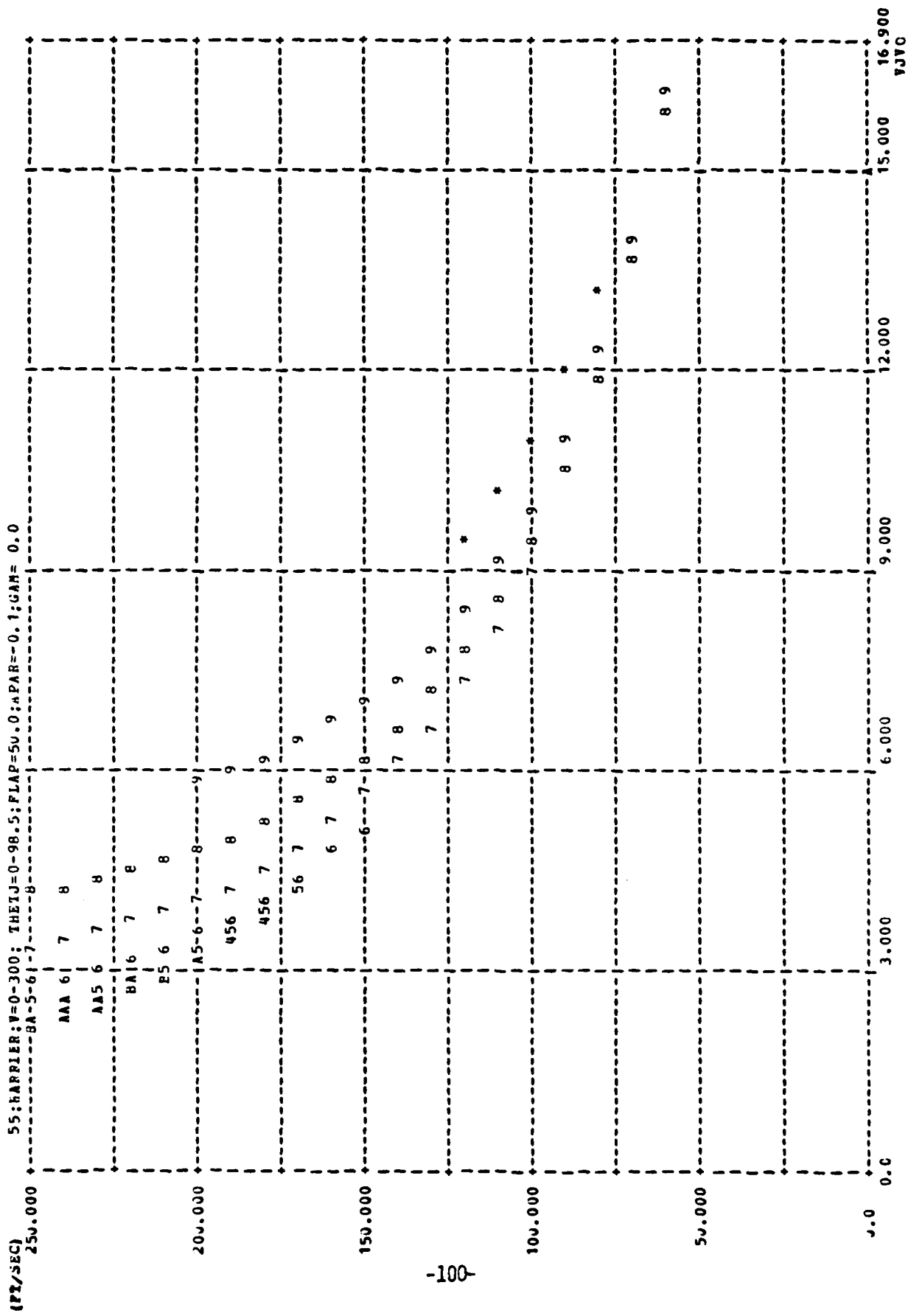


FIGURE 92 - Trimap of $V_j/V_\infty(\theta_j, V_\infty)$; with $\delta_f = 50^\circ$, $\alpha_{V_c} = -0.1$ g, $\gamma_c = 0.0$ rad.

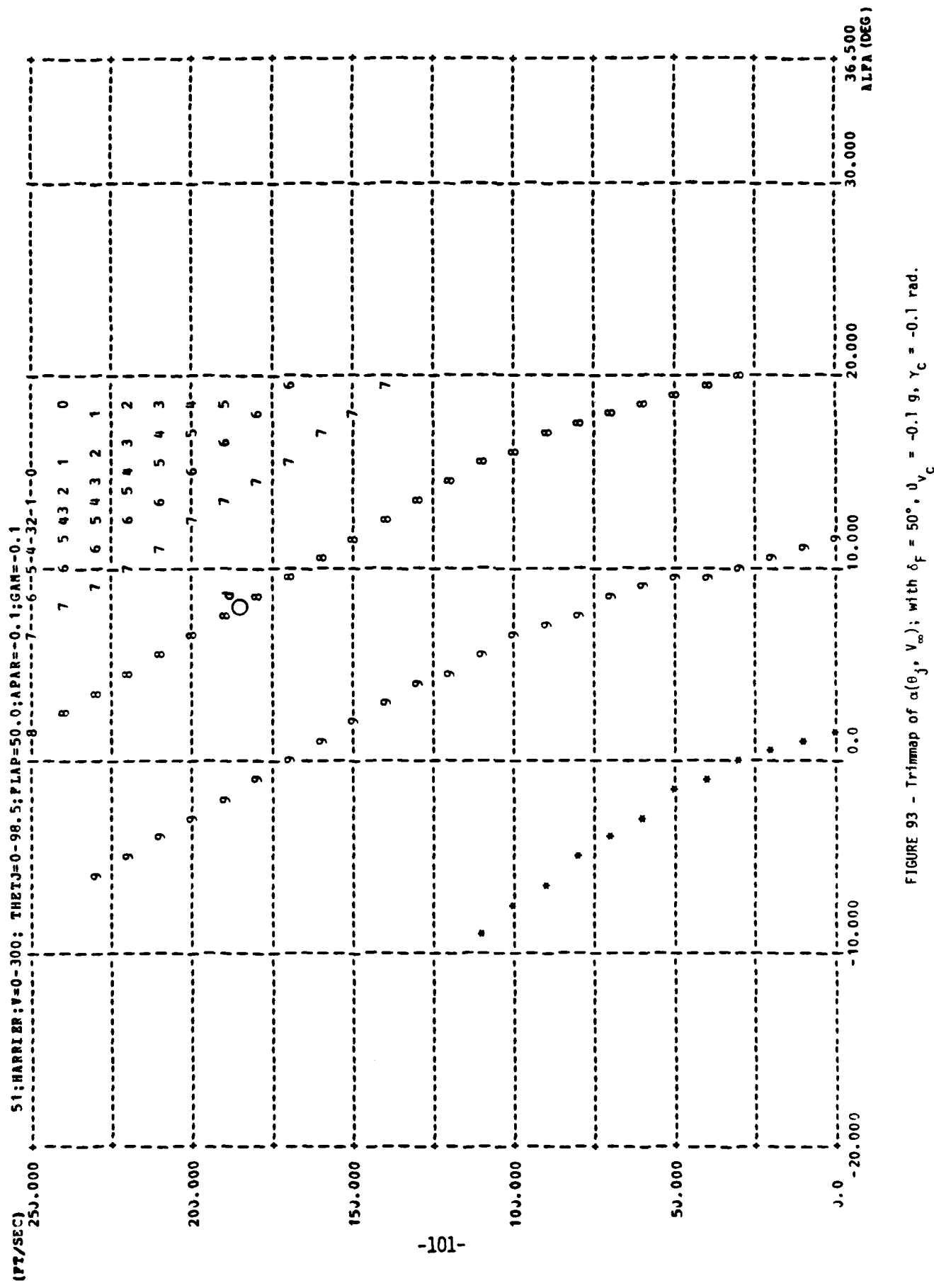


FIGURE 93 - Trimmap of $\alpha(\theta_j, V_\infty)$; with $\delta_F = 50^\circ$, $u_{V_C} = -0.1$ g, $\gamma_C = -0.1$ rad.

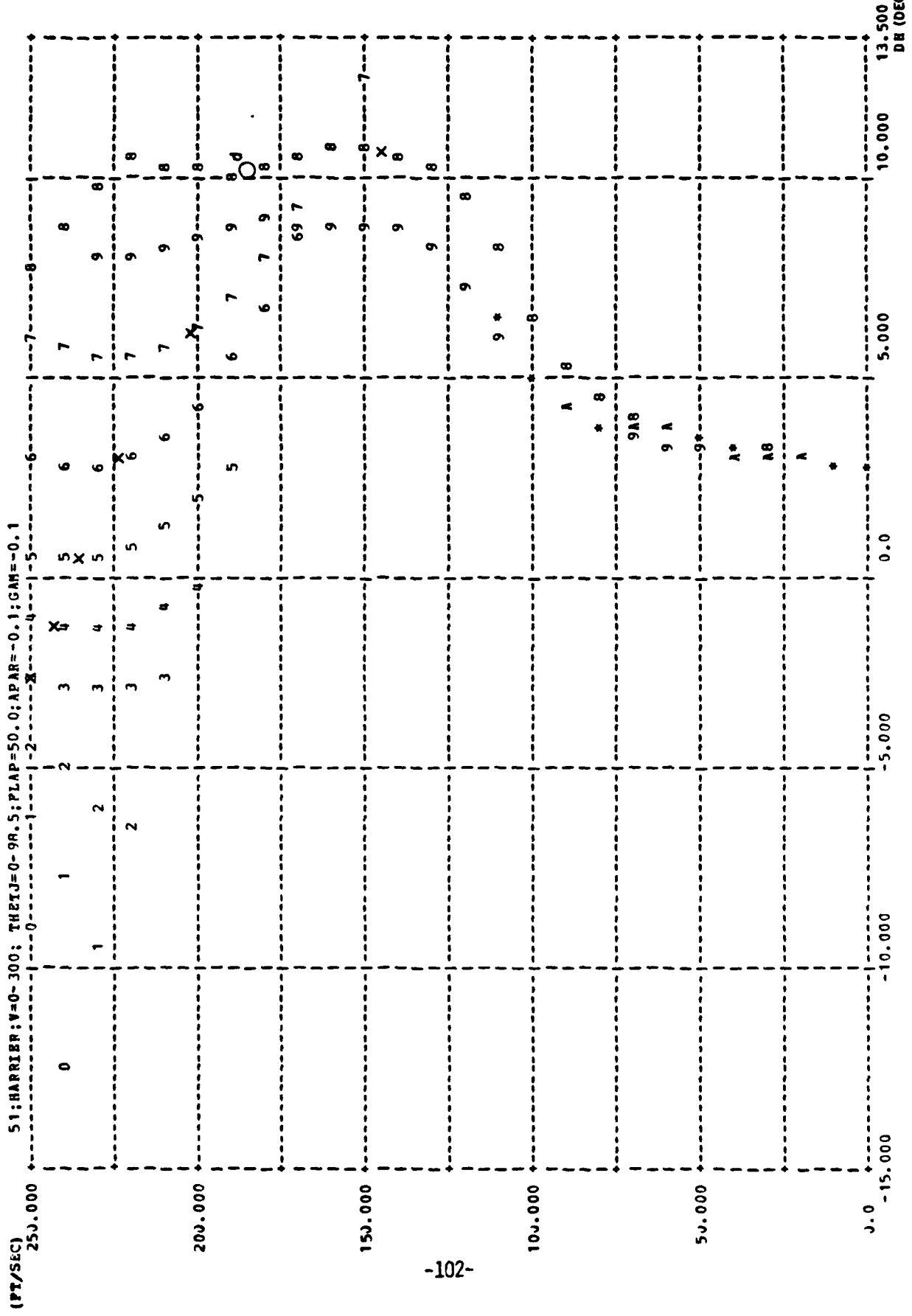
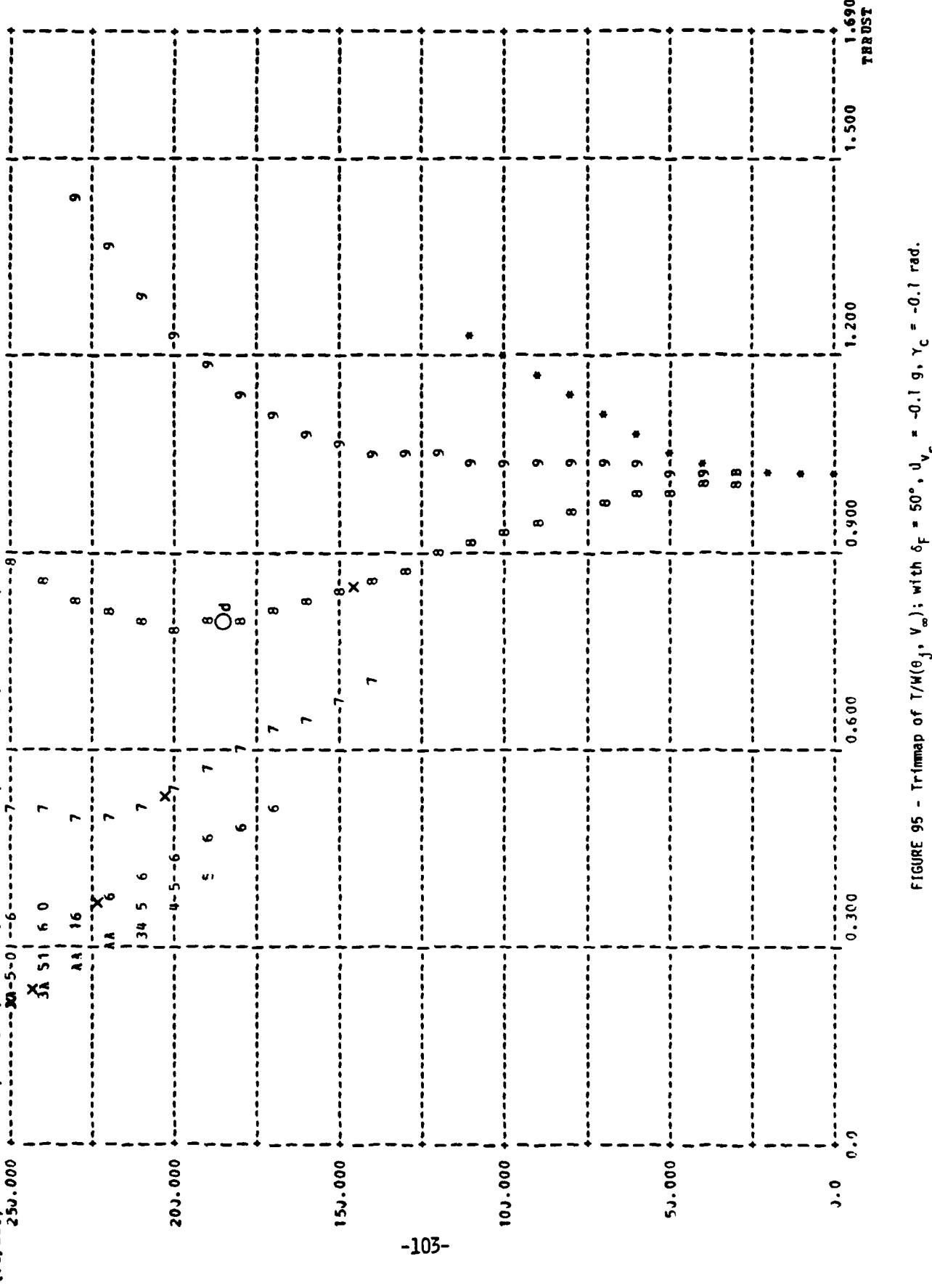


FIGURE 94 - Trimmapp of $\delta_H(\theta_j, V_\infty)$; with $\delta_F = 50^\circ$, $\dot{v}_{V_C} = -0.1 \text{ g}$, $\gamma_C = -0.1 \text{ rad}$.

51:HARRIER:V=0-300; THETJ=C-98.5:PLAP=50,0;APAR=0,1;GAM=0,1



51:HARRIER:V=0-300: THETAJ=0-98.5:PLAP=50.0:APAR=0. 1:GAM=0. 1

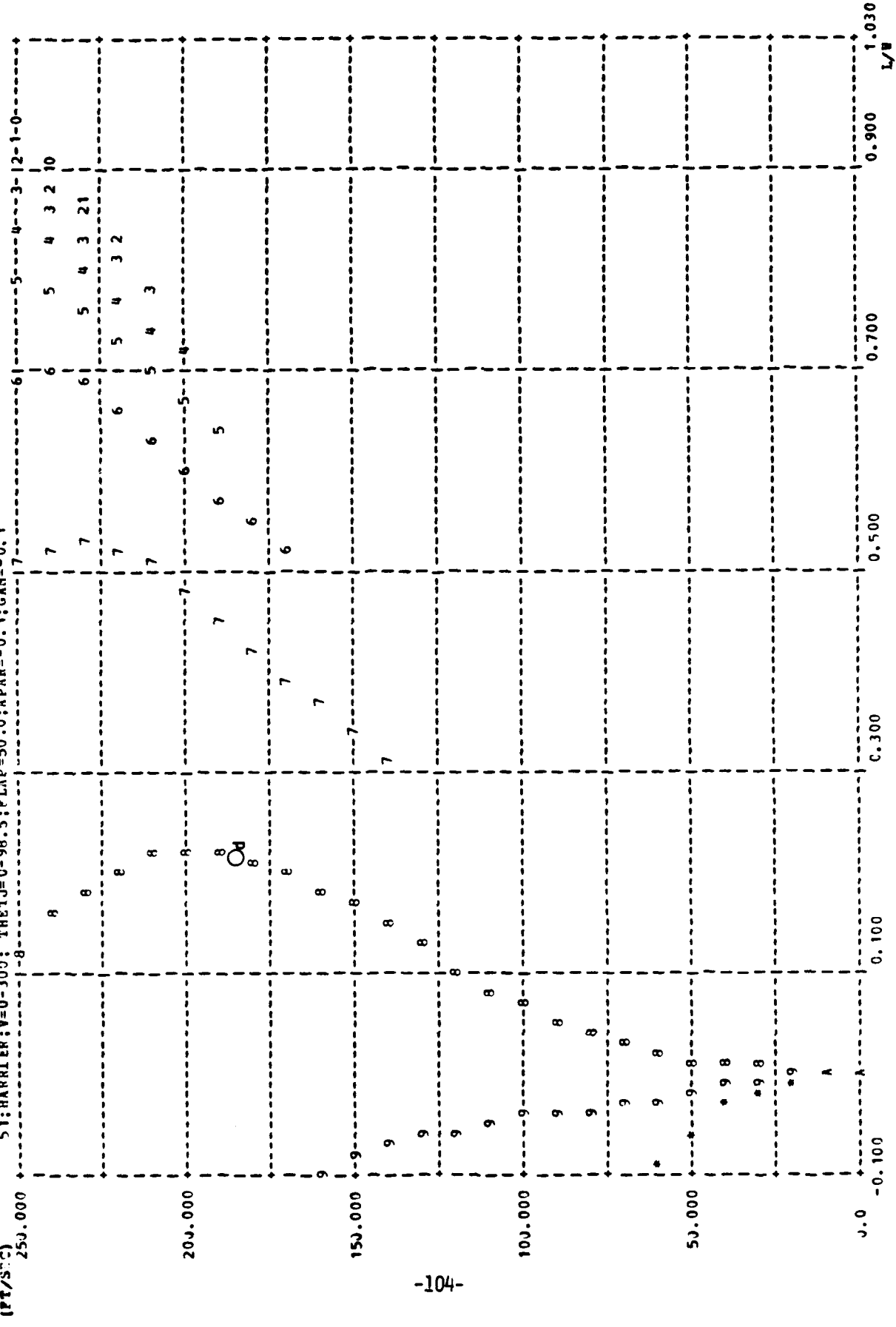


FIGURE 96 - Trimmap of $L/W(\theta_j, V_\infty)$; with $\delta_F = 50^\circ$, $\dot{v}_{V_C} = -0.1$ g, $\gamma_C = -0.1$ rad.

51; HARRIER; V=0-300; THFTJ=0-98.5; PLAP=50.0; APAR=-0.1; GAM=-0.1

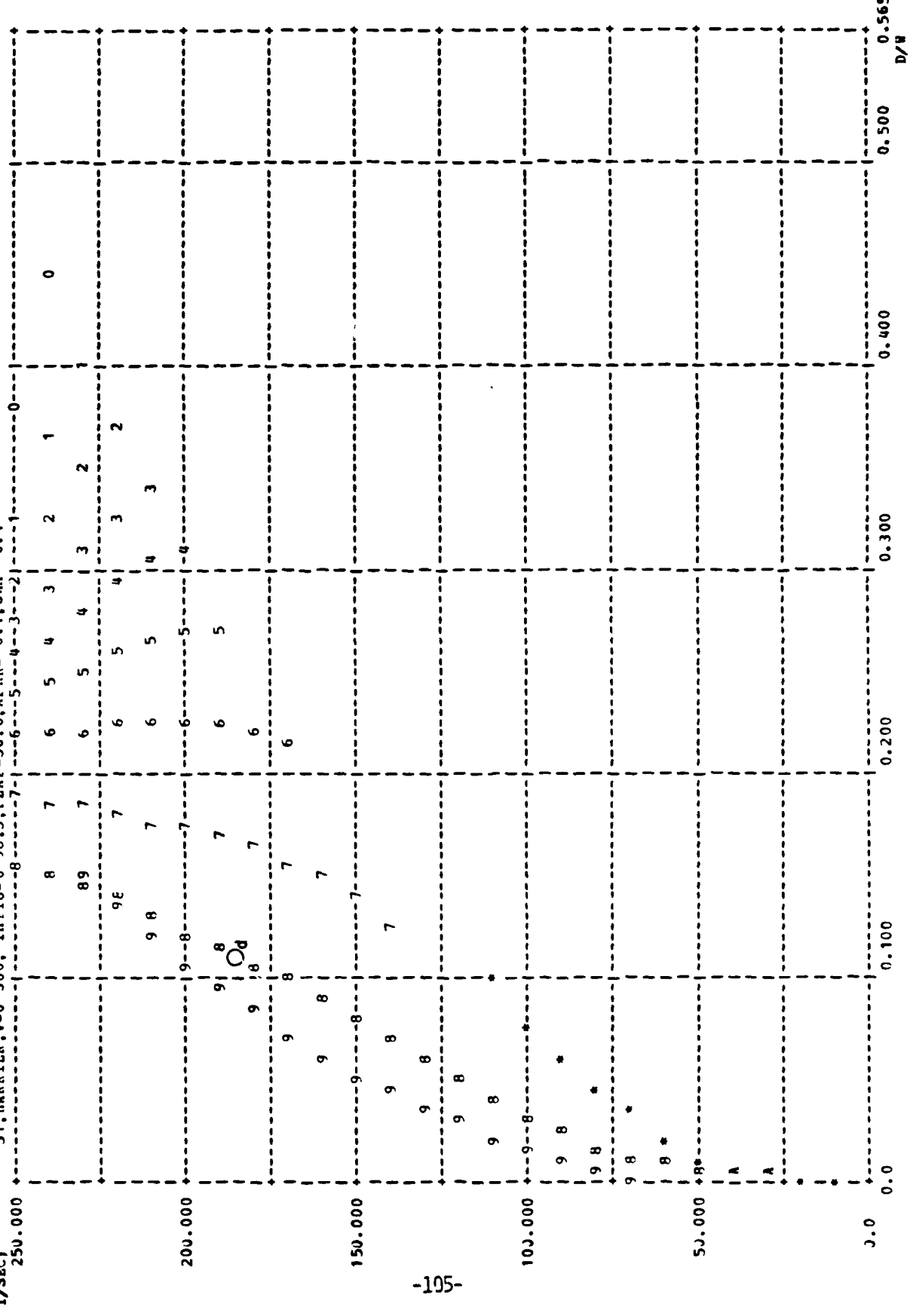


FIGURE 97 - Trimmap of $D/W(\theta_j, V_\infty)$; with $\delta_F = 50^\circ$, $V_c = -0.1$ g, $\gamma_c = -0.1$ rad.

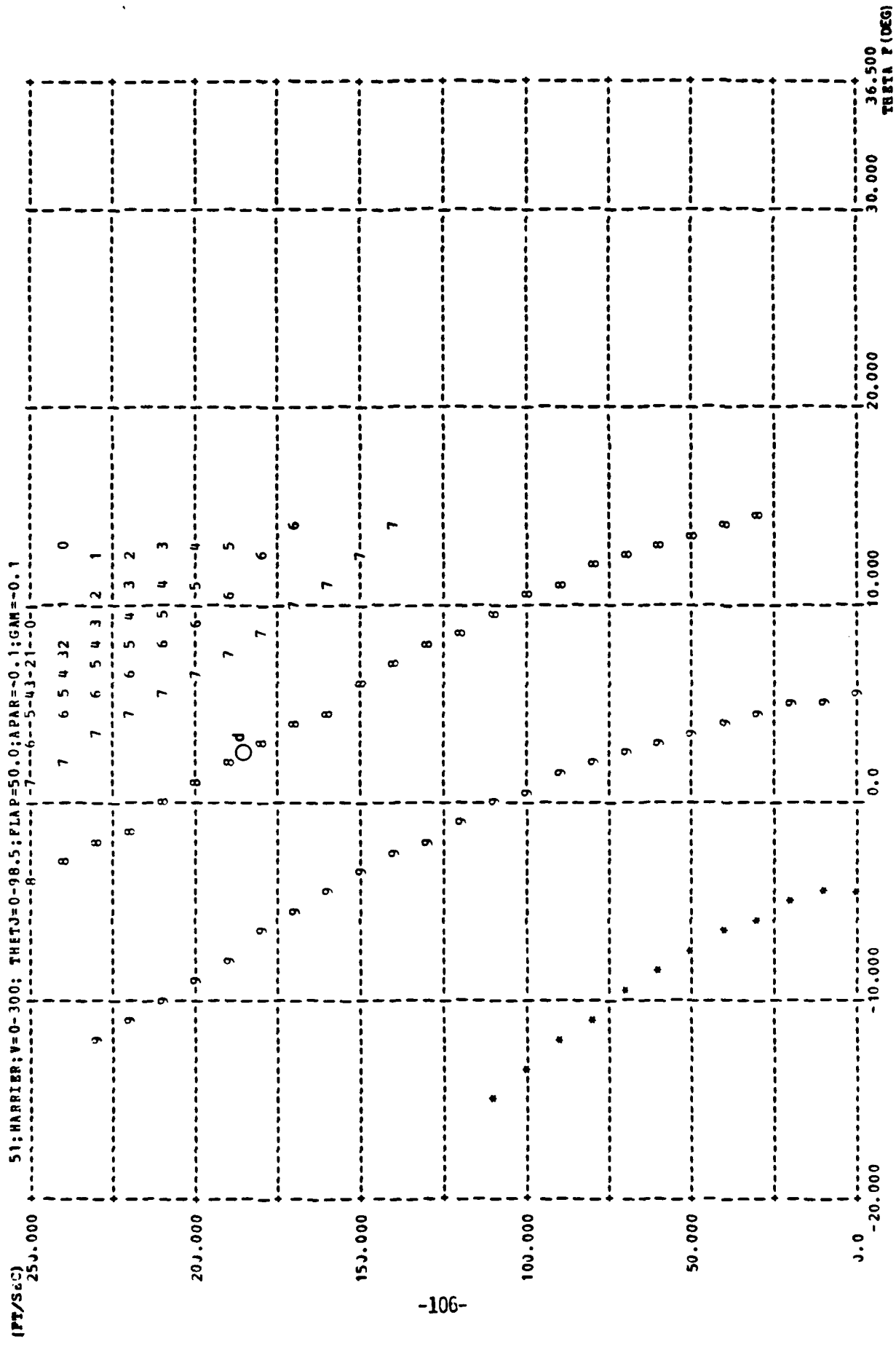


FIGURE 98 - Trimmap of $\theta(\theta_j, v_\infty)$; with $\delta_F = 50^\circ$, $v_{v_c} = -0.1$ g, $\gamma_c = -0.1$ rad.

51:HARRIER:V=0-300: THETJ=0-9H.5;PLAP=50.0;APAR=0.1;GAN=-0.1

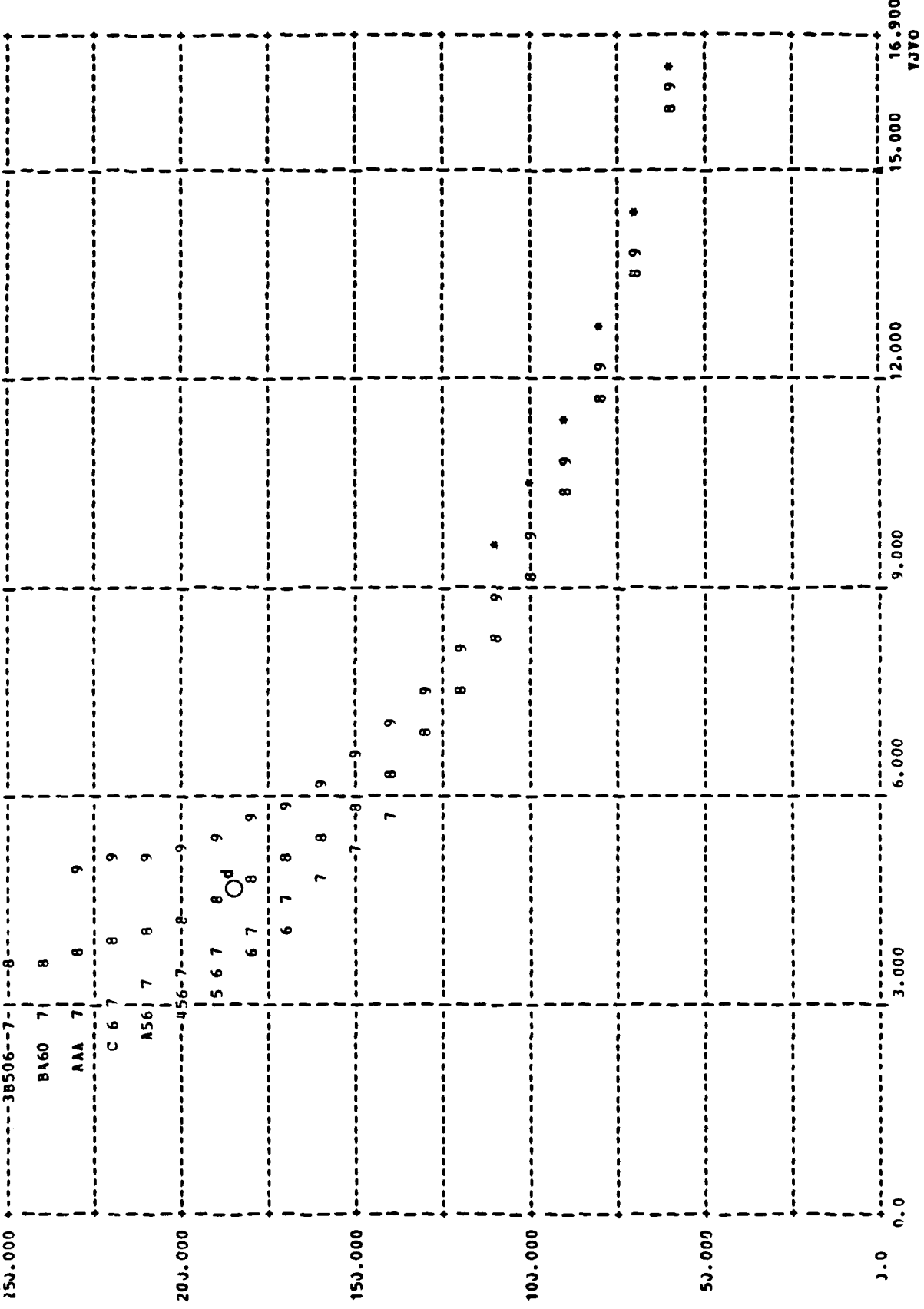


FIGURE 99 - Trimmap of $V_j/V_{\infty}(\theta_j, V_{\infty})$; with $\delta_F = 50^\circ$, $\dot{V}_{V_c} = -0.1$ g, $\gamma_c = -0.1$ rad.

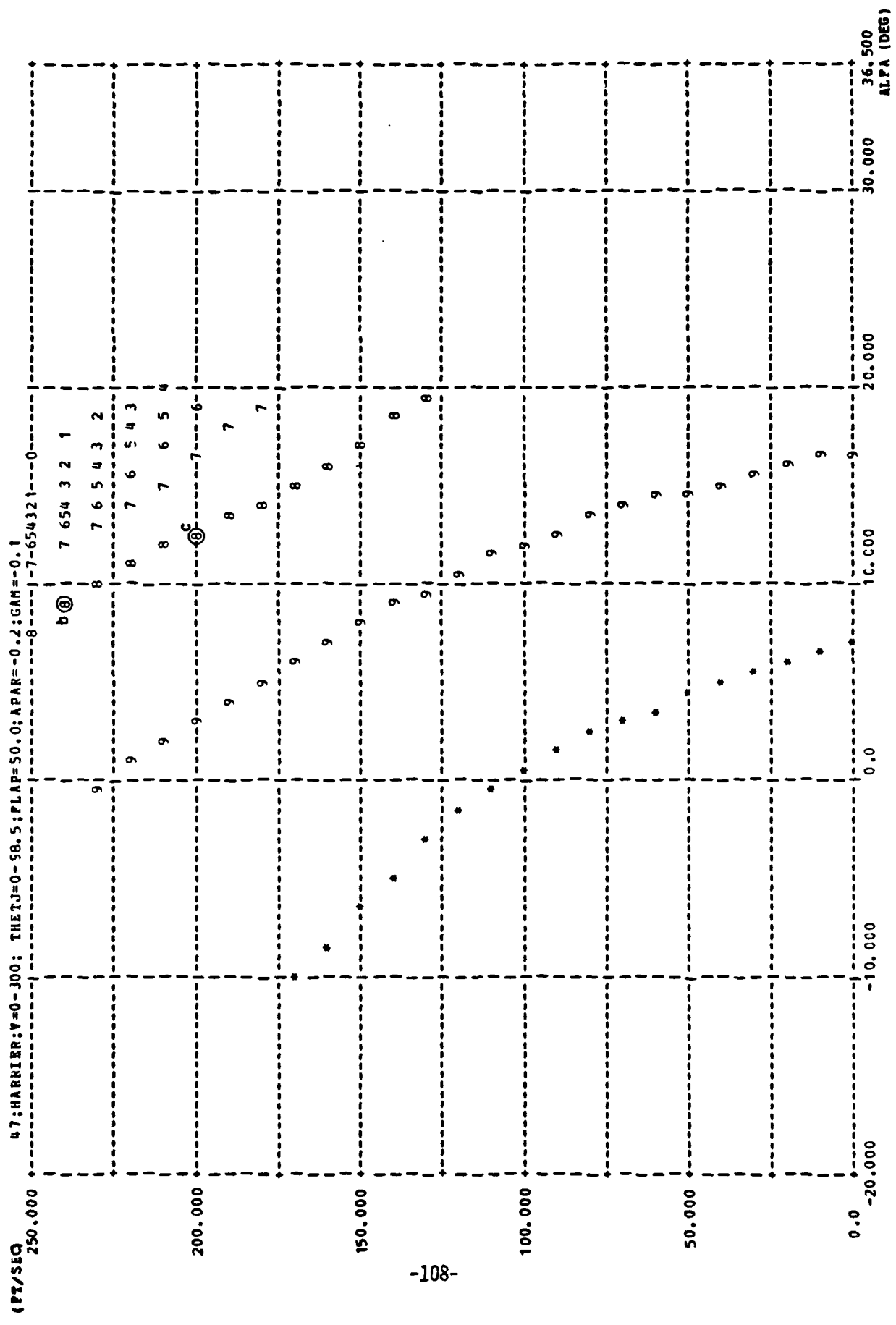


FIGURE 100 - Trimmap of $\alpha(\theta_j, V_\infty)$; with $\delta_F = 50^\circ$, $\dot{V}_C = -0.2$ g, $\gamma_C = -0.1$ rad.

47:HARRIER2: Y=0-300; THE TJ=0-98.5; PLMP=50.0; APAR=-0.2; GAM=-0.1

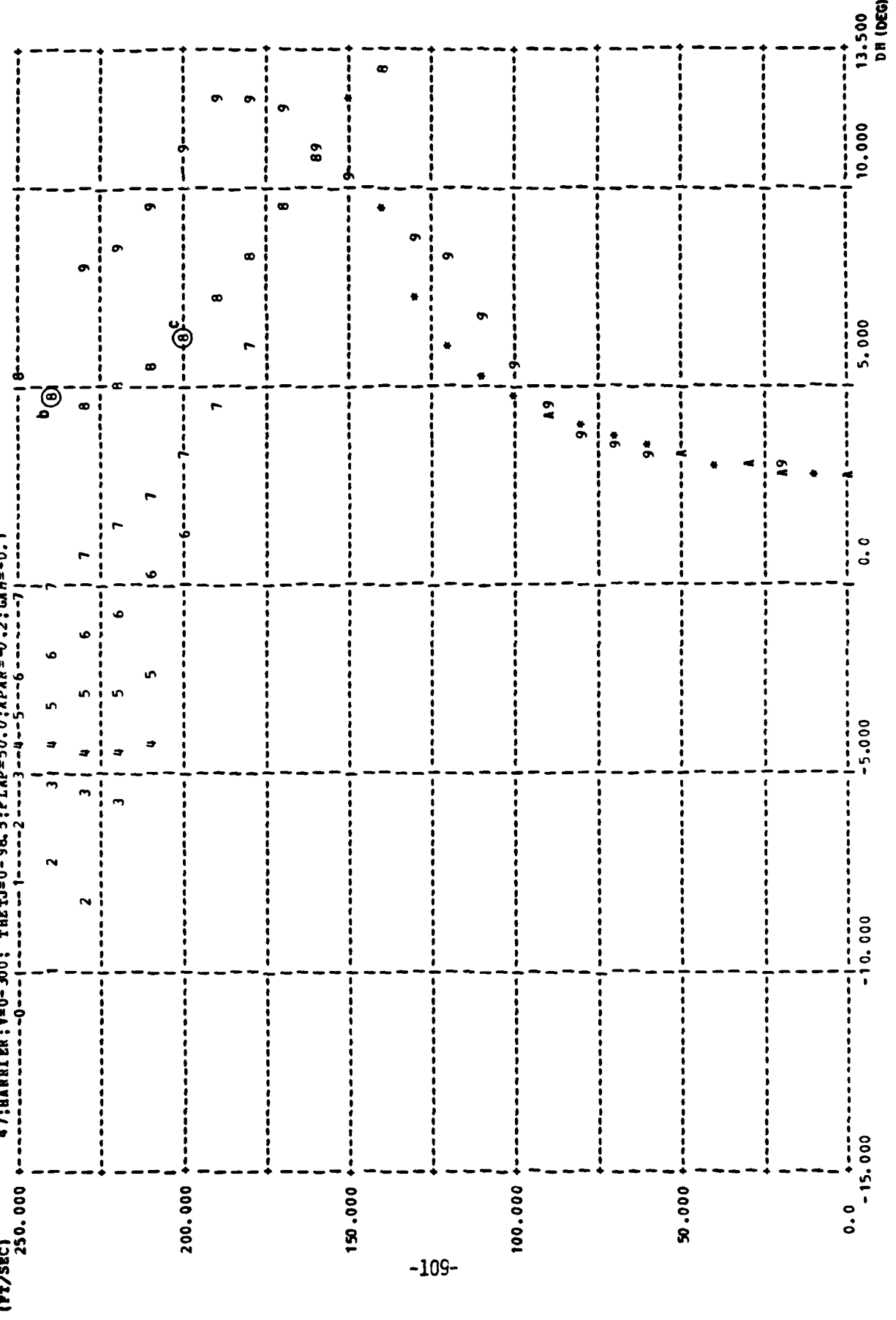


FIGURE 101 - Triimap of $\delta_H(\theta_j, V_\infty)$; with $\delta_F = 50^\circ$, $\delta_{V_C} = -0.2$ g, $\gamma_C = -0.1$ rad.

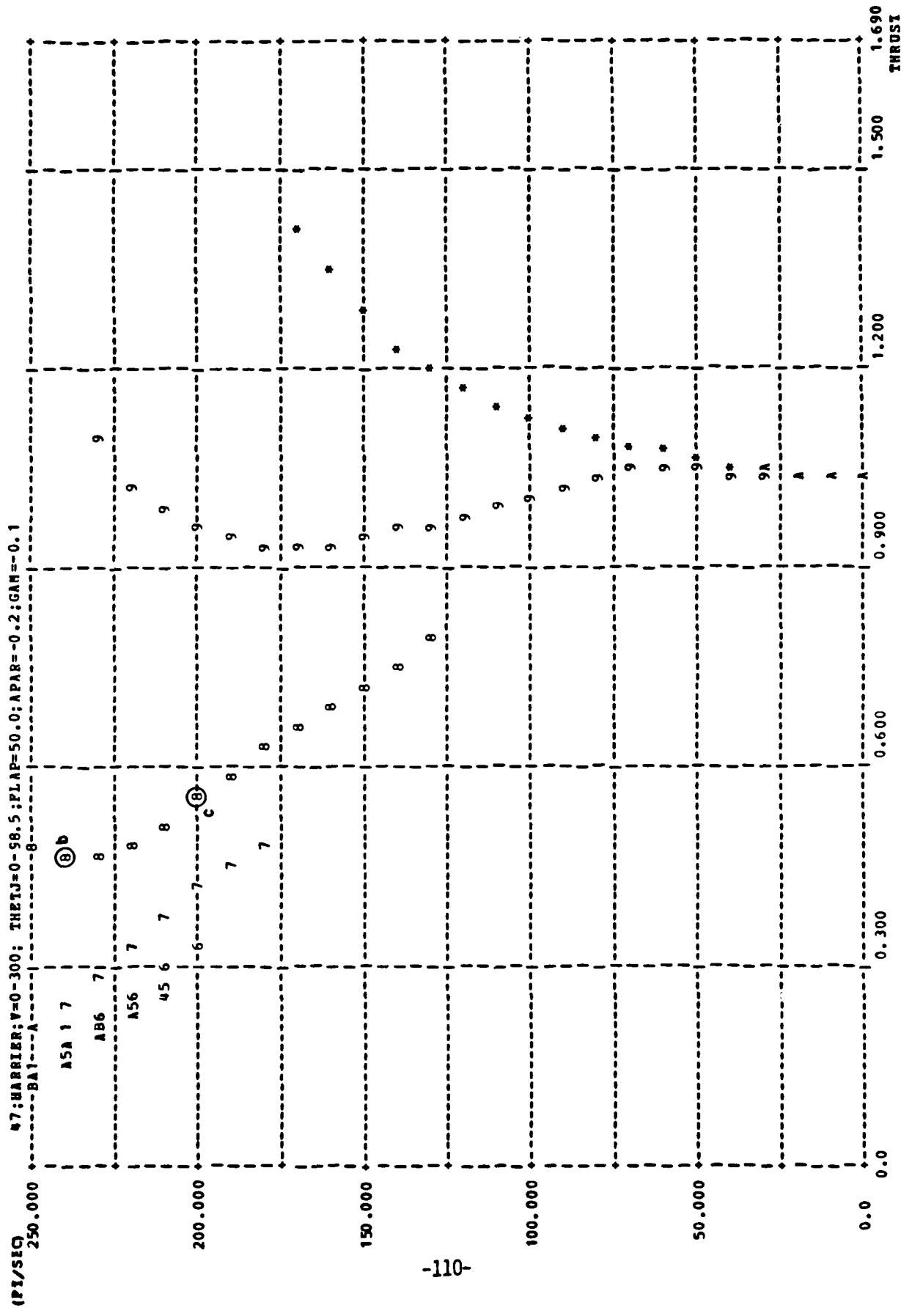


FIGURE 102 - Trimmap of $T/W(\theta_j, V_\infty)$: with $\delta_F = 50^\circ$, $u_{V_c} = -0.2$ g, $\gamma_c = -0.1$ rad.

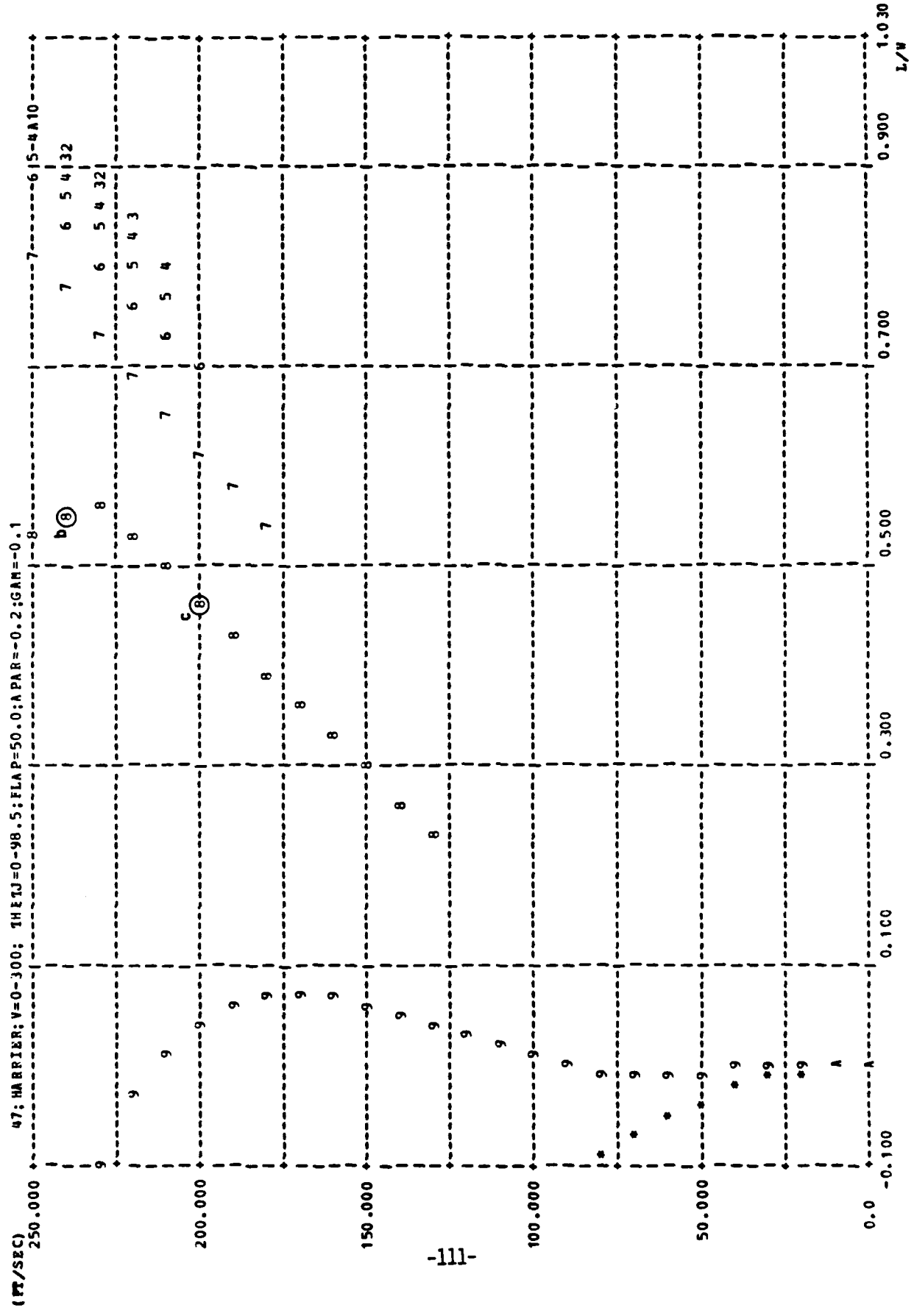


FIGURE 103 - Trimmap of $L/W(\theta_j, V_\infty)$; with $\delta_F = 50^\circ$, $\dot{V}_{V_c} = -0.2$ g, $\gamma_c = -0.1$ rad.

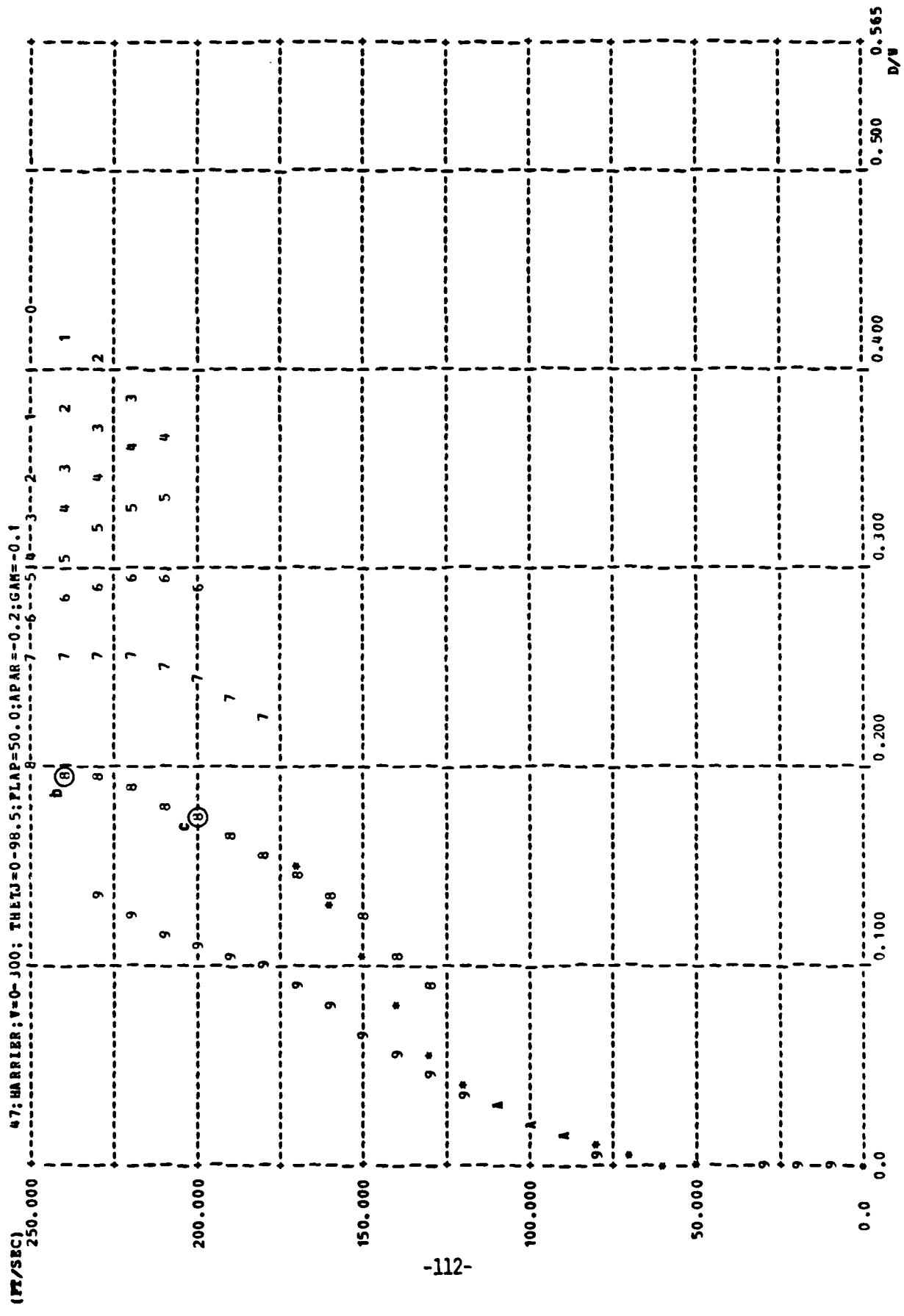


FIGURE 104 - Trimap of $D/W(\theta_j, V_\infty)$; with $\delta_F = 50^\circ$, $U_{V_C} = -0.2 g$, $\gamma_C = -0.1$ rad.

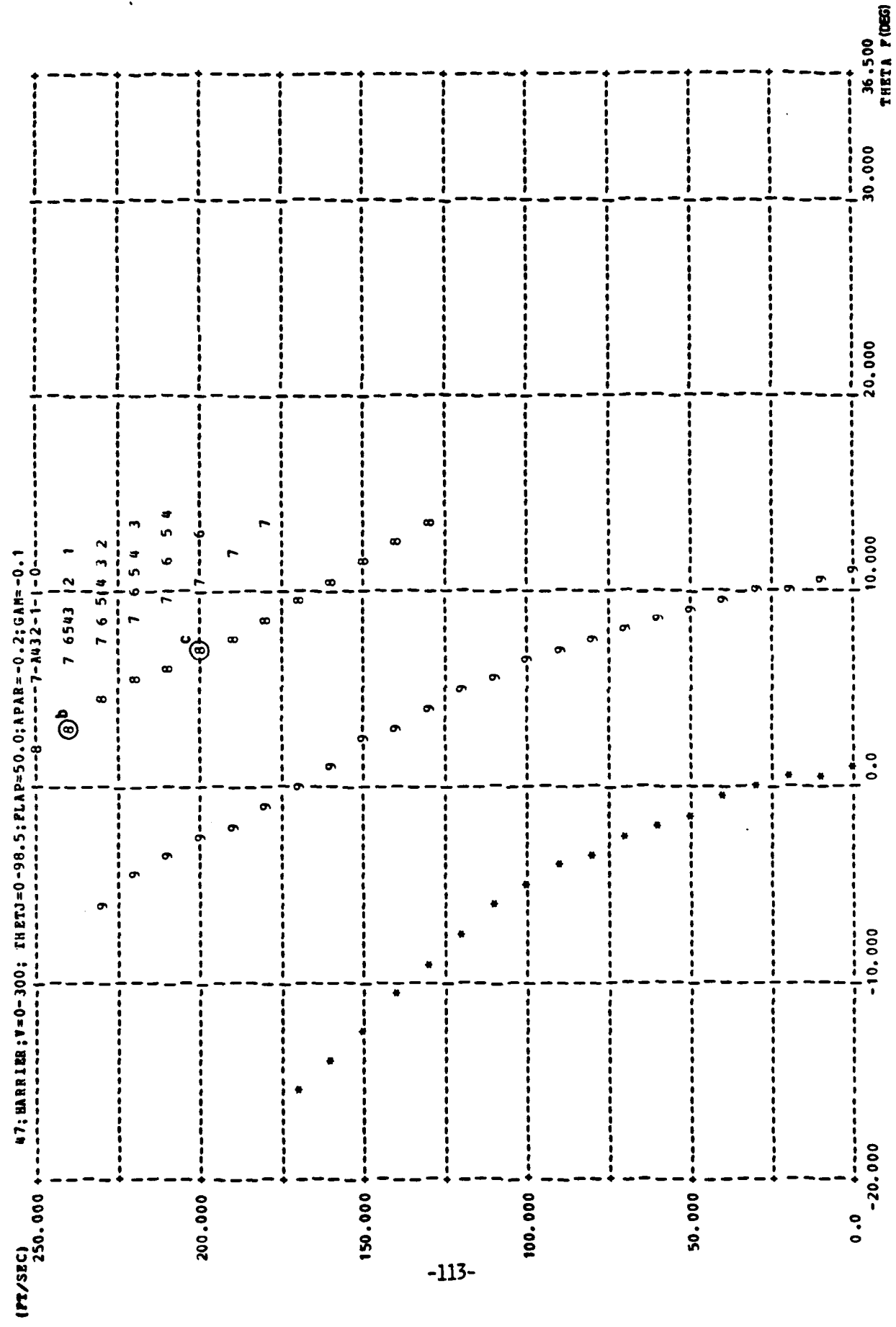


FIGURE 105 - Trimmap of $\theta(\theta_j, v_\infty)$: with $\delta_F = 50^\circ$, $\dot{u}_{v_c} = -0.2$ g, $\gamma_c = -0.1$ rad.

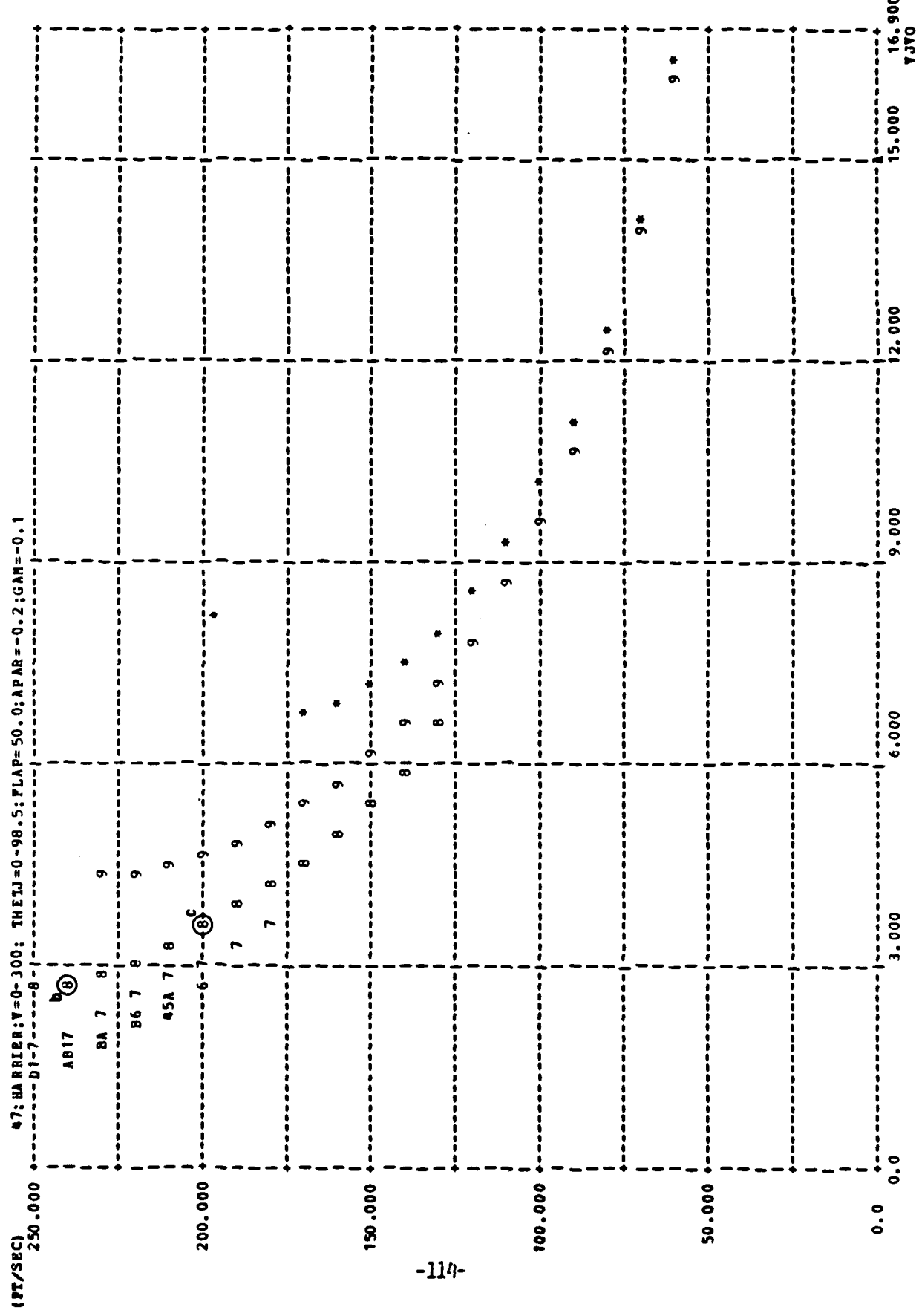


FIGURE 106 - Trimmap of $V_j/V_\infty(\theta_j, V_\infty)$; with $\delta_F = 50^\circ$, $0_{V_c} = -0.2$ g, $\gamma_c = -0.1$ rad.

APPENDIX A
EQUATIONS OF MOTION

In this section the equations used in modeling the transition of the AV-8A will be presented. First the equations will be derived for three dimensional flight, one set at a time. Then each set of equations will be reduced to consider only flight in a vertical plane with zero sideslip. As stated in Chapter 2, all aircraft body rotational velocities and accelerations are assumed to be zero in quasi-equilibrium flight. Therefore, $p_B = q_B = r_B = \dot{p}_B = \dot{q}_B = \dot{r}_B = 0$.

TRANSLATIONAL ACCELERATIONS

Now the equations for \dot{u}_B , \dot{v}_B and \dot{w}_B will be derived. It is first assumed that the rate of fuel consumption ($\frac{W}{g}$) has a negligible effect on the dynamics of the aircraft. However, the fuel consumed throughout a maneuver may still be considered by adjusting W to reflect fuel consumed. With the assumption $W = \text{constant}$.

$$F = m\dot{v} = \frac{W}{g} \dot{v}$$

or

$$\dot{v} = a = \frac{F}{W} \text{ for acceleration in g's.}$$

In aircraft body axes

$$\dot{v}_B = (F_B + T_B)/W + g_B \text{ (in g's)} \quad (A-1)$$

where

$$\dot{v}_B \triangleq \begin{bmatrix} \dot{u}_B \\ \dot{v}_B \\ \dot{w}_B \end{bmatrix} \quad \text{translational accelerations, body frame (in g's)}$$

$$\underline{F}_B \triangleq \begin{bmatrix} F_{x_B} \\ F_{y_B} \\ F_{z_B} \end{bmatrix} \quad \text{aerodynamic forces, body frame}$$

$$\underline{T}_B \triangleq \begin{bmatrix} T_{x_B} \\ T_{y_B} \\ T_{z_B} \end{bmatrix} \quad \text{engine and reaction control system forces, body frame}$$

$$\underline{g}_B \triangleq \begin{bmatrix} g_{x_B} \\ g_{y_B} \\ g_{z_B} \end{bmatrix} \quad \text{local unit gravity vector, body frame}$$

While \underline{T}_B is normally defined in body axes, the aerodynamic forces are usually expressed in wind axes and the gravity force in the local inertial axes (flat, non-rotating earth). Therefore, these forces must be transformed to body axes.

$$\underline{F}_B = H_w^B \underline{F}_w$$

$$\begin{bmatrix} F_{x_B} \\ F_{y_B} \\ F_{z_B} \end{bmatrix} = \begin{bmatrix} (\cos \alpha \cos \beta) & (-\cos \alpha \sin \beta) & (-\sin \alpha) \\ (\sin \beta) & (\cos \beta) & (0) \\ (\sin \alpha \cos \beta) & (-\sin \alpha \sin \beta) & (\cos \alpha) \end{bmatrix} \begin{bmatrix} F_{x_w} \\ F_{y_w} \\ F_{z_w} \end{bmatrix}$$

$$\underline{g}_B = H_I^B \underline{g}_I$$

$$\begin{bmatrix} \underline{g}_{x_B} \\ \underline{g}_{y_B} \\ \underline{g}_{z_B} \end{bmatrix} = \begin{bmatrix} (\cos \theta \cos \psi) & (\cos \theta \sin \psi) & (-\sin \theta) \\ (\sin \phi \sin \theta \cos \psi) & (\sin \phi \sin \theta \sin \psi) & (\sin \phi \cos \theta) \\ (\cos \phi \sin \theta \cos \psi) & (\cos \phi \sin \theta \sin \psi) & (\cos \phi \cos \theta) \end{bmatrix} \begin{bmatrix} 0 \\ 0 \\ 1 \end{bmatrix}$$

expanding

$$\underline{g}_B = \begin{bmatrix} -\sin \theta \\ \sin \phi \cos \theta \\ \cos \phi \cos \theta \end{bmatrix} \text{ for the acceleration of gravity in g's}$$

Now \underline{F}_w and \underline{T}_B must be determined. \underline{F}_w includes all of the aerodynamic forces acting on the aircraft including effects of the thrust on the wing, body, and tail aerodynamics. Referring to Figure 2,

$$\underline{F}_w \triangleq \begin{bmatrix} -D \\ Y \\ -L \end{bmatrix}$$

The equations determining L and D are presented later in this section. Since lateral motion is not addressed in this paper, sideforce (Y), is not discussed.

\underline{T}_B represents the engine and reaction control system (RCS) forces. For simplicity it will be assumed the cg and all the RCS and main engine nozzles are located in the $x-y_B$ plane. All RCS thrust vectors will be assumed to act perpendicular to the $x-y$ body plane. This is reasonable because all RCS nozzles are 8° or less from the perpendicular. The main engine nozzles are assumed to be perpendicular to the y_B axis.

$$\underline{T}_B \triangleq \begin{bmatrix} T_{x_B} \\ T_{y_B} \\ T_{z_B} \end{bmatrix} = \begin{bmatrix} T \cos \theta_j \\ -T_\psi \\ -T \sin \theta_j - T_{\theta_A} - T_{\theta_F} - T_{\phi_P} - T_{\phi_S} \end{bmatrix}.$$

The RCS thrusts are functions of the stabilizer, aileron and rudder positions and gross thrust. The fore and aft distribution of main nozzle thrust is a function of gross thrust. The methods for computing the thrusts are given in Chapter 2.

Substituting the above relations into equation A-1 and expanding,

$$\dot{u}_B = \frac{1}{W} [-D \cos \alpha \cos \beta - Y \cos \alpha \sin \beta + L \sin \alpha + T \cos \theta_j] - \sin \theta$$

$$\dot{v}_B = \frac{1}{W} [-D \sin \beta + Y \cos \beta - T_\psi] + \sin \phi \cos \theta \quad (A-2)$$

$$\dot{w}_B = \frac{1}{W} [-D \sin \alpha \cos \beta - Y \sin \alpha \sin \beta - L \cos \alpha - T \sin \theta_j - T_{\theta_A} - T_{\theta_F} - T_{\phi_P} - T_{\phi_S}] + \cos \phi \cos \theta$$

where \dot{u}_B , \dot{v}_B and \dot{w}_B are all in g's

Since this report considers only flight in a vertical plane and assumes that there are no ambient winds, the equation for \dot{v}_B drops out and the equations for \dot{u}_B and \dot{w}_B become

$$\begin{aligned} \dot{u}_B &= \frac{1}{W} [-D \cos \alpha + L \sin \alpha + T \cos \theta_j] - \sin \theta \\ \dot{w}_B &= \frac{1}{W} [-D \sin \alpha - L \cos \alpha - T \sin \theta_j \\ &\quad - T_{\theta_A} - T_{\theta_F}] + \cos \theta \end{aligned} \quad (A-3)$$

These two equations are the basis for equations FO(1) and FO(2) in the HARRIER.

LIFT AND DRAG EQUATIONS

For the AV-8A the aerodynamic lift and drag functions are quite complicated because of jet interference effects. C_L is not only a function of angle of attack (α), stabilizer position (δ_H), flap deflection (δ_F), etc. as in conventional aircraft, but it also depends on the nozzle deflection (θ_j) and the thrust (T). Chapter 2 describes how C_L and C_D are determined based on available data.

Given C_L , C_Y and C_D , and $\bar{q} \triangleq \frac{1}{2} \rho V_\infty^2$, the equations for aerodynamic lift, side force and drag are simply

$$\begin{aligned} L &= \bar{q} SC_L \\ Y &= \bar{q} SC_Y \\ D &= \bar{q} SC_D \end{aligned} \tag{A-4}$$

Again, since only flight in the vertical plane with no winds is considered, only the lift and drag are relevant for this study.

$$\begin{aligned} L &= \bar{q} SC_L \\ D &= \bar{q} SC_D \end{aligned} \tag{A-5}$$

These two equations are the basis for FO(3) and FO(4) in HARRIER.

AXIS TRANSFORMATIONS

As stated in Chapter 2, inputs are defined in the flight path axis system. They are then transformed to the local inertial axis system

for comparison to the aircraft velocity to test convergence.

The transformation from the flight path axis system to the inertial axis system is as follows;

$$\dot{\underline{x}}_I = H_{V-V}^1 \underline{v} \quad (A-6)$$

where

$$\dot{\underline{x}}_I \triangleq [\dot{x}_I \dot{y}_I \dot{z}_I]^T$$

with no wind, and rotating first to horizontal

$$\begin{bmatrix} \dot{x}_I \\ \dot{y}_I \\ \dot{z}_I \end{bmatrix} = \begin{bmatrix} \cos \gamma \cos \xi & -\sin \xi & \sin \gamma \cos \xi \\ \cos \gamma \sin \xi & \cos \xi & \sin \gamma \sin \xi \\ -\sin \gamma & 0 & \cos \gamma \end{bmatrix} \begin{bmatrix} V_\infty \\ 0 \\ 0 \end{bmatrix}$$

Where V_∞ is the aircraft velocity and ξ is the flight path azimuth angle referenced to North. Expanding the above;

$$\begin{aligned} \dot{x}_I &= V_\infty \cos \gamma \cos \xi \\ \dot{y}_I &= V_\infty \cos \gamma \sin \xi \\ \dot{z}_I &= -V_\infty \sin \gamma \end{aligned} \quad (A-7)$$

Assuming ξ to be zero, \dot{y}_I can be omitted.

$$\begin{aligned} \dot{x}_I &= V_\infty \cos \gamma \\ \dot{z}_I &= -V_\infty \sin \gamma \end{aligned} \quad (A-8)$$

These two relations express the commanded inertial velocity components, VPC(1) and VPC(3), in the equations for F0(5) and F0(6) in the HARRIER.

The remaining components of equations F0(5) and F0(6) are the elements of the transformation from body to inertial axes. Given \underline{v}_W^I , the components of the wind with respect to the earth,

$$\dot{\underline{x}}_I = H_B^I \underline{v}_B + \underline{v}_W^I \quad (A-9)$$

$$\begin{bmatrix} \dot{x}_I \\ \dot{y}_I \\ \dot{z}_I \end{bmatrix} = \begin{bmatrix} \cos \theta \cos \psi & -\cos \phi \sin \psi & \sin \phi \sin \psi \\ \sin \phi \sin \theta \cos \psi & \cos \phi \sin \theta \cos \psi & \cos \phi \sin \theta \sin \psi \\ -\sin \theta & \sin \phi \cos \theta & \cos \phi \cos \theta \end{bmatrix} \begin{bmatrix} u_B \\ v_B \\ w_B \end{bmatrix} + \begin{bmatrix} v_{wx}^I \\ v_{wy}^I \\ v_{wz}^I \end{bmatrix}$$

Expanding and assuming $v_B = \phi = \psi = 0$ and with no wind, $\dot{y}_I \equiv 0$ and

$$\dot{x}_I = u_B \cos \theta + w_B \sin \theta \quad (A-10)$$

$$\dot{z}_I = -u_B \sin \theta + w_B \cos \theta$$

In order to study the effects of acceleration on the conversion corridor, constant accelerations are considered inputs in the flight path axis system. These were transformed to the body axis system in which the aerodynamic lift, drag and moment coefficients are available.

Assuming the rate of change of wind velocity to be negligible,

$$\dot{\underline{v}}_B = H_V^B \dot{\underline{v}}_V = H_I^B H_V^I \dot{\underline{v}}_V \quad (A-11)$$

Again, $\phi = \psi = \xi = \dot{v}_V = 0$, so for our problem the above may be reduced to

$$\dot{u}_B = \dot{u}_V \cos (\theta - \gamma) - \dot{w}_V \sin (\theta - \gamma) \quad (A-12)$$

$$\dot{w}_B = \dot{u}_V \sin (\theta - \gamma) + \dot{w}_V \cos (\theta - \gamma)$$

However, if the winds are also assumed to be zero,

$$\alpha \equiv \theta - \gamma$$

$$\dot{u}_B = \dot{u}_v \cos \alpha - \dot{w}_v \sin \alpha$$

$$\dot{w}_B = \dot{u}_v \sin \alpha + \dot{w}_v \cos \alpha \quad (A-13)$$

In HARRIER, \dot{u}_v and \dot{w}_v are referred to as ACPC(1) and ACPC(3), respectively, which represent the inputs APAR and APER.

MOMENT EQUATIONS

In general for a rigid body, $\underline{M}_I a + \underline{M}_I e = \frac{d}{dt} (I_I \underline{\omega}_I)$ in an inertial coordinate system, where

$\underline{M}_I a \triangleq$ total aerodynamic moment

$\underline{M}_I e \triangleq$ total moment due to engine and RCS forces

$I_I \triangleq$ aircraft inertia tensor

$\underline{\omega}_I \triangleq$ aircraft rotational velocity vector

In quasi-equilibrium flight $\underline{\omega}_I \equiv 0$, so the equations reduce to

$$\underline{M}_I a + \underline{M}_I e = 0$$

The sum of the moments must be zero irrespective of the coordinate system.

Both the aerodynamic and the engine moments are given in body axes.

$$\underline{M}_B a + \underline{M}_B e = 0 \quad (A-14)$$

$$\underline{M}_B a \triangleq \begin{bmatrix} L_a \\ M_a \\ N_a \end{bmatrix}$$

aerodynamic moments

$$\underline{M}_B e \triangleq \begin{bmatrix} L_e \\ M_e \\ N_e \end{bmatrix}$$

engine moments

Assuming the moment reference center is located along the x_B axis, the aerodynamic moments may be defined as,

$$L_a = \bar{q} Sb C_l$$

$$M_a = \bar{q} Sc C_m + x_{mr} \bar{q} Sc_L \cos \alpha + x_{mr} \bar{q} Sc_D \sin \alpha$$

$$N_a = \bar{q} Sb C_n + x_{mr} \bar{q} Sc_Y \cos \alpha$$

The components used in computing C_m and C_L are discussed in Chapter 2. C_l , C_Y and C_n are not discussed in this paper.

Again referring to Figure 2,

$$L_e = (T_{\phi_S} - T_{\phi_P}) x_\phi$$

$$M_e = T_{\theta_F} x_{\theta_F} - T_{\theta_A} x_{\theta_A} + T_{jF} x_{jF} - T_{jA} x_{jA}$$

$$+ (T_{\phi_P} + T_{\phi_S}) x_{\phi\theta}$$

$$N_e = T_\psi x_\psi$$

The modelling of the RCS and engine thrusts is described in Chapter 2.

Substituting the above into equation (A-14) and expanding,

Rolling Moment $0 = \bar{q} Sb C_l + (T_{\phi_P} - T_{\phi_S}) x_\phi$

Pitching Moment $0 = \bar{q} Sc C_m + T_{\theta_F} x_{\theta_F} - T_{\theta_A} x_{\theta_A} + T_{jF} x_{jF} - T_{jA} x_{jA} + (T_{\phi_P} + T_{\phi_S}) x_{\phi\theta} + x_{mr} \bar{q} Sc_L \cos \alpha + x_{mr} \bar{q} Sc_D \sin \alpha$ (A-15)

Yawing Moment $0 = \bar{q} Sb C_N + T_\psi x_\psi + x_{mr} \bar{q} Sc_Y \cos \beta$

As previously mentioned, only the longitudinal plane is considered in this paper and the equation for pitching moment is the only one

implemented in HARRIER. In addition it is assumed that the roll and yaw RCS jets are not being used. Therefore,

$$\begin{aligned} \text{Pitching Moment } 0 = \bar{q} S_c C_m + T_{\theta_F} x_{\theta_F} - T_{\theta_A} x_{\theta_A} + T_{jF} x_{jF} \\ - T_{jA} x_{jA} + x_{mr} \bar{q} S_C L \cos \alpha + x_{mr} \bar{q} S_C D \sin \alpha \end{aligned} \quad (A-16)$$

This forms the basis for FO(7) in HARRIER.

LIFT-LOSS CURVES

As mentioned in Chapter 2, some discrepancy was found in the data in Reference 5 when the data from the aforementioned carpet plots for C_L were compared to another figure in the same Reference (reproduced here as Figure 33) which shows the lift-loss as a function of V_j/V_∞ . The lift-loss presented by the carpet plot data in Figures 3 through 6 can be compared to that in Figure 33 in the following way. Assuming the lift-loss is invariant with α and using $\alpha = 8^\circ$ as reference,

$$\Delta C_{L_{\text{wing-body}}} = C_{L_{\text{wing-body}}} - C_{L_{0_{\text{wing-body}}}}$$

where

$$C_{L_{\text{wing-body}}} = C_{L_{\text{wing-body}}} \text{ at given } \theta_j \text{ and } V_j/V_\infty$$

(from Figures 3 through 6)

$$C_{L_{0_{\text{wing-body}}}} = C_{L_{\text{wing-body}}} \text{ at } \theta_j = 0 \text{ or } V_j/V_\infty = 0$$

$$\Delta L = \Delta C_{L_{\text{wing-body}}} \bar{q} S \quad \text{where } \bar{q} = (1/2) \rho V_\infty^2$$

Nondimensionalizing by gross thrust, T;

$$\frac{\Delta L}{T} = \frac{\Delta C_L \bar{q}S}{T}$$

From Reference 6, $T = (1/2)\rho V_j^2 S_j = (V_j/V_\infty)^2 \bar{q}S_j$

Therefore $\frac{\Delta L}{T} = \frac{\Delta C_L \bar{q}S}{(V_j/V_\infty)^2 \bar{q}S_j} = \frac{\Delta C_L S}{(V_j/V_\infty)^2 S_j}$

Using the above formula, the lift-loss presented by Figures 3 to 6 was computed and superimposed on Figure 33. These data obviously do not agree. Lift-loss obtained from the carpet plots is substantially greater than the lift-loss graph shows. In addition, the lift-loss graph shows a lift-loss at $\theta_j = 0$ which disagrees with the observations on pages 12 and 13. Furthermore, as

V_j/V_∞ goes to zero, the lift-loss curves first increase and then decrease in a range where no substantiating data could be found. The reason for this might be that the lift-loss should go to zero as V_j (hence V_j/V_∞) goes to zero. This would be reasonable except for the fact that at this point both ΔL and T tend towards zero so the ordinate of this figure, $\Delta L/T$, is actually an ill-defined point. The reason for these discrepancies could not be determined.

The wing-body aerodynamics for flaps-up flight were taken from Reference 5 and are presented in Figures 34 through 36. These data were obtained with $\theta_j = 0$ and it is assumed that there is no wing/jet interaction at this point.

APPENDIX B
METHOD OF SOLUTION

In earlier work in this field Marinucci (Ref. 10) used the Bellman quasi-linearization method (Ref. 11) for a similar problem. This method is an extension of the well known Newton-Raphson algorithm. Given a non-linear function,

$$y = f(x)$$

the basic Newton-Raphson method is an iterative process where given an initial guess for y , y_{old} , the value of y at some point x_{new} may be estimated by,

$$y_{new} \approx y_{old} + \left. \frac{df(x)}{dx} \right|_{x=x_{old}} \cdot (x_{new} - x_{old})$$

Bellman's quasi-linearization applies this to a system of equations, for

$$\begin{aligned} y &= f(x) \\ y_{new} &\approx y_{old} + \left. \frac{\partial f(x)}{\partial x} \right|_{x=x_{old}} (x_{new} - x_{old}) \end{aligned}$$

The Jacobian for the set of equations used in this problem and typical values are at the end of this Appendix. If, as in our case, $y \Delta 0$ and the value for x which satisfies this is desired, then

$$0 \approx y_{old} + J (x_{new} - x_{old}) \quad \text{where} \quad J \Delta \left. \frac{\partial f(x)}{\partial x} \right|$$

$$x_{new} \approx x_{old} - J^{-1} y_{old}$$

This x_{new} will be an approximation for the true answer. An obvious condition for using Bellmans' method is that J be non-singular. Refs. 10 and 11 describe conditions for convergence of this method, the most

important condition being the convexity of the functions $f(x)$. While convexity of the functions is a sufficient criterion for convergence it is not strictly necessary. For less dominant terms in any particular equation, if $f_k(x_j)$ is not convex, convergence may still normally be obtained by setting that respective term in the Jacobian to zero.

In summary, the iterative Bellman quasi-linearization is used as follows:

- 1.) guess a reasonable solution \underline{x}_{old}
- 2.) compute the Jacobian $\underline{J} \Big|_{\underline{x}=\underline{x}_{old}}$
- 3.) solve for $\underline{x}_{new} = \underline{x}_{old} - \underline{J}^{-1} \underline{y}_{old}$
- 4.) test convergence
 - a.) if convergence passes - STOP
 - b.) if convergence fails,
make $\underline{x}_{old} = \underline{x}_{new}$ and go to step 2.

Since the aerodynamic and control system functions of the HARRIER are highly non-linear most of the functions are input to the computer program as table look-ups. The computer SUBROUTINE which computes the values of the functions also computes the partial derivatives for substitution into the Jacobian.

With the equations as defined in Chapter 2, the Jacobian is shown on the last pages of this Appendix. The derivation of all elements in the Jacobian is straightforward except for the partial derivatives with respect to T/W since the aerodynamic data are given as functions of V_j/V_∞ , and

the table look-up routine therefore gives the partial derivative with respect to V_j/V_∞ ; the relation between V_j/V_∞ and T/W must be known.

$$T = (V_j/V_\infty)^2 \bar{q} S_j \text{ (as defined in Ref. 6).}$$

The derivative with respect to thrust can then be expressed in terms of the derivative with respect to V_j/V_∞ . Given the partial of some function f_i with respect to thrust,

$$\frac{\partial f_i}{\partial \frac{T}{W}} = \frac{\frac{\partial f_i}{\partial \frac{V_j}{V_\infty}}}{\frac{1}{W} \frac{V_j}{V_\infty}^2 \bar{q} S_j}$$

$$= \frac{\frac{\partial f_i}{\partial \frac{V_j}{V_\infty}}}{\frac{\bar{q} S_j}{W} \frac{V_j}{V_\infty}^2}$$

However, in most cases the table look-up computes $\frac{\partial f_i}{\partial \frac{V_j}{V_\infty}}$, therefore

$$\frac{\partial f_i}{\partial \frac{T}{W}} = \frac{\frac{\partial f_i}{\partial \frac{V_j}{V_\infty}}}{\frac{\bar{q} S_j}{W} \frac{V_j}{V_\infty}^2} \cdot \frac{\frac{V_j}{V_\infty}}{\frac{V_j}{V_\infty}^2}$$

$$= \frac{\frac{\partial f_i}{\partial \frac{V_j}{V_\infty}}}{\frac{\bar{q} S_j}{W} \frac{V_j}{V_\infty}} \cdot \frac{1}{2} \left(\frac{V_j}{V_\infty}\right)^{-1}$$

$$\frac{\partial f_i}{\partial \frac{T}{W}} = \frac{W}{\bar{q} S_j} \cdot \frac{1}{2 \left(\frac{V_j}{V_\infty}\right)} \frac{\frac{\partial f_i}{\partial \frac{V_j}{V_\infty}}}{\frac{V_j}{V_\infty}}$$

The next three pages show the elements $A(i,j)$ of the Jacobian in symbolic form.

$$\begin{aligned}
A(1,1) &= \sin \alpha \\
A(1,2) &= -\cos \alpha \\
A(1,3) &= \cos \theta_j \\
A(1,4) &= (D/W) \sin \alpha + (L/W) \cos \alpha + (\dot{u}_{V_c}/g) \sin \alpha + (\dot{w}_{V_c}/g) \cos \alpha - \cos \theta \\
A(1,5) &= 0 \\
A(1,6) &= 0 \\
A(1,7) &= 0 \\
A(2,1) &= -\cos \alpha \\
A(2,2) &= -\sin \alpha \\
A(2,3) &= \sin \theta_j - \frac{\partial T_{\theta_A}}{\partial T} - \frac{\partial T_{\theta_F}}{\partial T} \\
A(2,4) &= - (D/W) \cos \alpha + (L/W) \sin \alpha - (\dot{u}_{V_c}/g) \cos \alpha + (\dot{w}_{V_c}/g) \sin \alpha - \sin \theta \\
A(2,5) &= 0 \\
A(2,6) &= 0 \\
A(2,7) &= - \left(\frac{\partial T_{\theta_F}}{\partial \delta_H} + \frac{\partial T_{\theta_A}}{\partial \delta_H} \right) \frac{1}{W} \\
A(3,1) &= 1 \\
A(3,2) &= 0 \\
A(3,3) &= -S \left(\frac{\frac{\partial C_{L_{WB}}}{\partial V_j}}{\frac{\partial V_j}{\partial V_\infty}} + \frac{\frac{\partial C_{L_{\delta H}}}{\partial V_j}}{\frac{\partial V_j}{\partial V_\infty}} \Delta \delta_H \right) / (2 S_j \frac{V_j}{V_\infty}) - \bar{q} S \frac{\partial C_{L_{inlet}}}{\partial T} \\
A(3,4) &= -\bar{q} S \left(\frac{\partial C_{L_{WB}}}{\partial \alpha} + \frac{\partial C_{L_{inlet}}}{\partial \alpha} \right) / W \\
A(3,5) &= 0 \\
A(3,6) &= 0 \\
A(3,7) &= -\bar{q} S C_{L_{\delta H}} / W
\end{aligned}$$

$$\begin{aligned}
A(4,1) &= 0 \\
A(4,2) &= 1 \\
A(4,3) &= -S \frac{\partial C_{D_{WB}}}{\partial V_{\infty}} / (2 S_j \frac{V_j}{V_{\infty}}) - \frac{\partial D_{ram}}{\partial T} \\
A(4,4) &= \bar{q} S \frac{\partial C_{D_{WB}}}{\partial \alpha} / W \\
A(4,5) &= 0 \\
A(4,6) &= 0 \\
A(4,7) &= 0 \\
A(5,1) &= 0 \\
A(5,2) &= 0 \\
A(5,3) &= 0 \\
A(5,4) &= u_B \sin \theta - w_B \cos \theta \\
A(5,5) &= -\cos \theta \\
A(5,6) &= -\sin \theta \\
A(5,7) &= 0 \\
A(6,1) &= 0 \\
A(6,2) &= 0 \\
A(6,3) &= 0 \\
A(6,4) &= u_B \cos \theta + w_B \sin \theta \\
A(6,5) &= \sin \theta \\
A(6,6) &= -\cos \theta \\
A(6,7) &= 0
\end{aligned}$$

$$A(7,1) = \frac{Wx_{mr}}{I_{yy}} \cos \alpha$$

$$A(7,2) = \frac{Wx_{mr}}{I_{yy}} \sin \alpha$$

$$A(7,3) = \frac{W}{I_{yy}} \left[x_{\theta_F} \frac{\partial T_{\theta_F}}{\partial T} - x_{\theta_A} \frac{\partial T_{\theta_A}}{\partial T} + \frac{\bar{Sc}}{2S_j \frac{V_j}{V_{\infty}}} \left(\frac{\partial C_{m_{WB}}}{\partial \frac{V_j}{V_{\infty}}} + \frac{\partial C_{m_{\delta H}}}{\partial \frac{V_j}{V_{\infty}}} \Delta \delta_H \right) \right]$$

$$+ \bar{q} \bar{Sc} \frac{\partial C_{m_{inlet}}}{\partial T} + x_{jF} \sin \theta_j \frac{\partial T_{jF}}{\partial T} + x_{jA} \sin \theta_j \frac{\partial T_{jA}}{\partial T} \right]$$

$$A(7,4) = \frac{1}{I_{yy}} \left[\bar{q} \bar{Sc} \left(\frac{\partial C_{m_{\delta H}}}{\partial \alpha} \Delta \delta_H + \frac{\partial C_{m_{inlet}}}{\partial \alpha} \right) + x_{mr} L \sin \alpha + x_{mr} D \cos \alpha \right]$$

$$A(7,5) = 0$$

$$A(7,6) = 0$$

$$A(7,7) = \frac{1}{I_{yy}} \left[\bar{q} \bar{Sc} C_{m_{\delta H}} + x_{\theta_F} \frac{\partial T_{\theta_F}}{\partial \delta_H} + x_{\theta_A} \frac{\partial T_{\theta_A}}{\partial \delta_H} \right]$$